

1-1-2010

## Vortices in the near field of optical dipole radiation

Xin Li

Follow this and additional works at: <https://scholarsjunction.msstate.edu/td>

---

### Recommended Citation

Li, Xin, "Vortices in the near field of optical dipole radiation" (2010). *Theses and Dissertations*. 4973.  
<https://scholarsjunction.msstate.edu/td/4973>

This Dissertation - Open Access is brought to you for free and open access by the Theses and Dissertations at Scholars Junction. It has been accepted for inclusion in Theses and Dissertations by an authorized administrator of Scholars Junction. For more information, please contact [scholcomm@msstate.libanswers.com](mailto:scholcomm@msstate.libanswers.com).

VORTICES IN THE NEAR FIELD OF OPTICAL DIPOLE RADIATION

By

Xin Li

A Dissertation  
Submitted to the Faculty of  
Mississippi State University  
in Partial Fulfillment of the Requirements  
for the Degree of Doctor of Philosophy  
in Engineering Physics  
in the Department of Physics and Astronomy

Mississippi State, Mississippi

December 2010

Copyright by

Xin Li

December 2010

VORTICES IN THE NEAR FIELD OF OPTICAL DIPOLE RADIATION

By

Xin Li

Approved:

---

Henk F. Arnoldus  
Associate Professor of Physics and  
Astronomy  
(Director of Dissertation)

---

Erdem Topsakal  
Associate Professor of Electrical and  
Computer Engineering  
(Committee Member)

---

Donna M. Pierce  
Assistant Professor of Physics and  
Astronomy  
(Committee Member)

---

Chuji Wang  
Assistant Professor of Physics and  
Astronomy  
(Committee Member)

---

Wenchao Ma  
Professor of Physics and  
Astronomy  
(Committee Member)

---

David L. Monts  
Professor of Physics and  
Astronomy  
(Graduate Coordinator)

---

Sarah A. Rajala  
Dean of the James Worth Bagley College  
of Engineering

Name: Xin Li

Date of Degree: December 10, 2010

Institution: Mississippi State University

Major Field: Engineering Physics

Major Professor: Dr. Henk F. Arnoldus

Title of Study: VORTICES IN THE NEAR FIELD OF OPTICAL DIPOLE RADIATION

Pages in Study: 149

Candidate for Degree of Doctor of Philosophy

An oscillating electric dipole emits radiation, and the flow of energy is represented by the field lines of the Poynting vector. In the most general state of oscillation the dipole moment vector traces out an ellipse. We have evaluated analytically and numerically the field lines of the Poynting vector for the emitted light, and it appears that each field line lies on a cone, which has its axis perpendicular to the plane of the ellipse. The field lines exhibit a vortex structure near the location of the dipole, and they approach a straight line in the far field. The spatial extent of the optical vortex is well below the wavelength of the emitted radiation. It is shown that the asymptotic limit of a field line is displaced as compared to a ray which would come directly out of the source. This near-field vortex pattern will also lead to a shift of the intensity distribution of the radiation in the far field.

The emission of radiation by a linearly oscillating electric dipole is drastically altered when the dipole is close to a mirror. The energy is not emitted along optical rays, as for a free dipole, but as a set of four optical vortices. At a larger distance from the dipole singularities and isolated vortices appear. It is shown that most of these interference

vortices are due to the vanishing of the magnetic field at their centers. In the plane of the mirror there is a singular circle with a diameter which is proportional to the distance between the dipole and the mirror. Inside this circle, all energy flows to a singularity on the mirror surface.

We have also demonstrated a peculiar property of energy transport of optical dipole radiation in a negative index of refraction material (NIM). When the particle is embedded in a NIM and the dipole moment is rotating, the direction of rotation of the field lines of energy flow is reversed as compared to the rotation of the field lines for emission in a dielectric.

## DEDICATION

*To my parents and my grandparents.*

## ACKNOWLEDGEMENTS

I would like to express my deepest gratitude to my advisor, Dr. Henk F. Arnoldus, for all his help, encouragement, exceptional guidance, and inspirations throughout my PhD study. This work would not have been possible without his effort and support. I would also like to express my thanks to my advisor Dr. Erdem Topsakal and to Dr. John T. Foley for their numerous discussions, suggestions and support of this work.

I would like to sincerely thank Dr. Donna Pierce, Dr. Chuji Wang and Dr. Wenchao Ma for their valuable time and for serving on my committee.

I would also like to thank my former colleagues Ms. Jie Shu and Mr. Ruiyuan Mu in the MSU theoretical optics research group for their friendship, assistance and cooperation during this work.

Finally, I would like to thank my family, my father Zegong Li, my mother Huiying Guo and my grandma Xiangqian Kong for their endless love and support. I am incredibly lucky to have them in my life.



## TABLE OF CONTENTS

	Page
DEDICATION .....	ii
ACKNOWLEDGEMENTS .....	iii
LIST OF FIGURES .....	vi
<b>CHAPTER</b>	
I. INTRODUCTION .....	1
1.1 Background.....	1
1.2 Overview.....	2
II. NANOSCALE STRUCTURE OF THE ENERGY FLOW LINES FOR DIPOLE RADIATION IN FREE SPACE.....	10
2.1 The Poynting Vector for Electric Dipole Radiation .....	11
2.2 Magnetic Dipole.....	16
2.3 Elliptical Dipole Moment .....	18
2.4 Field Lines of the Poynting Vector.....	21
2.4.1 Solution for the Field Lines .....	23
2.5 Displacement in the Far Field.....	30
2.5.1 Asymptotic Limit of the Field Lines.....	31
2.5.2 Displacement Vector.....	34
III. SUBWAVELENGTH RESOLUTION IN THE FAR FIELD INTENSITY PROFILE OF OPTICAL DIPOLE RADIATION.....	43
3.1 Intensity in the Image Plane.....	43
3.1.1 Angular Distribution of the Emitted Power.....	45
3.1.2 Intensity Distribution of the Radiation on a Plane .....	46
3.2 Extremum in the Far Field Intensity Profile of a Circular Dipole .....	51
3.2.1 Shift of the Peak in the Far Field for a Circular Dipole .....	57
3.3 Far Field Intensity Pattern for an Elliptical Dipole.....	61
3.4 Intensity in the Near Field.....	66

3.5	Macroscopic Far-Field Observation of the Near-Field Dipole Vortex .....	68
3.5.1	The Difference Profile .....	68
3.5.2	Experimental Setup and Results .....	72
IV.	ELECTRIC DIPOLE RADIATION NEAR A MIRROR .....	78
4.1	Emission of Radiation.....	82
4.2	Field Lines in the $yz$ -Plane.....	88
4.3	Field Lines in the Plane of the Mirror.....	99
V.	DIPOLE RADIATION IN A DIELECTRIC AND A NEGATIVE INDEX OF REFRACTION MATERIAL.....	107
5.1	Introduction to Metamaterials.....	108
5.2	Negative Index of Refraction Materials.....	110
5.3	Green's Function and the Index of Refraction.....	117
5.4	Electric Dipole Radiation.....	118
5.5	The Poynting Vector for a Dielectric and a NIM .....	120
5.6	Conclusions.....	122
VI.	CONCLUSIONS AND FUTURE WORK .....	123
6.1	Conclusions .....	123
6.2	Future Work .....	124
	REFERENCES .....	128
	APPENDIX	
A.	CALCULATION OF THE POYNTING VECTOR FOR A DIPOLE LOCATED AT A DISTANCE H ABOVE A MIRROR.....	135
B.	NUMERICAL ASPECTS OF THE COMPUTATION OF FIELD LINES .....	139
C.	THE POYNTING VECTOR CLOSE TO A DIPOLE ABOVE A MIRROR.....	146
D.	BIOGRAPHICAL SKETCH .....	148
E.	PUBLICATIONS OF XIN LI.....	150

## LIST OF FIGURES

1.1	Atom, molecule or nano-particle in a laser beam .....	3
1.2	The emission of light by a source of radiation.....	4
1.3	Ray diagram for the image formation of a point source near a mirror (left) and a sketch of a possible energy flow pattern (right).....	6
2.1	The most general state of oscillation of an electric dipole moment $\mathbf{d}(t)$ .....	20
2.2	A typical field line of the Poynting vector for the radiation emitted by an electric dipole with $\beta = 1$ , located at the origin of coordinates.....	26
2.3	Three field lines of the Poynting vector for $\beta = 1$ and $\phi_0 = \pi/2$ .....	27
2.4	Field lines of the Poynting for $\beta = 1$ and $\theta_0 = \pi/4$ and $3\pi/4$ .....	28
2.5	Field line for $\beta = 0.1$ .....	29
2.6	Field line for $\beta = 0.001$ .....	30
2.7	A field line approaches asymptotically a line $\ell$ at a large distance .....	32
2.8	Dependence of the displacement on $\theta_0$ .....	35
2.9	A field line in the $xy$ -plane for an elliptical dipole with $\beta = 0.5$ .....	36
2.10	Three field lines in the $xy$ -plane ( $\theta_0 = \pi/2$ ) for a circular dipole ( $\beta = 1$ ) .....	37
2.11	The observation plane for an observer located in the direction $\hat{\mathbf{r}}_0$ with respect to the source .....	39
2.12	Field lines for $\theta_0 = \pi/2$ and $\phi_0 = \pi/2$ .....	41

3.1	Several field lines in the $xy$ -plane of the Poynting vector for the case of a counterclockwise rotating circular dipole in the $xy$ -plane .....	48
3.2	The image plane .....	49
3.3	The intensity distribution in an image plane perpendicular to the $y$ -axis .....	52
3.4	Curve $\alpha$ and its approximation .....	58
3.5	The far-field intensity distribution for a rotating dipole .....	59
3.6	The shift $\bar{\mu}_p$ curve and the displacement $\bar{\mu}_d$ curve .....	60
3.7	The location of the maxima as a function of $ \beta $ .....	64
3.8	The shift $\bar{\mu}_p$ for $\beta \geq 0$ .....	65
3.9	The intensity distribution for an elliptical dipole moment with $\beta = 0.4$ .....	67
3.10	The near-field intensity distribution for a dipole with $\beta = 1$ .....	69
3.11	The difference profile $\Delta I$ .....	72
3.12	The extrema on the $\bar{\mu}$ -axis are located at $\bar{\mu}_e$ and $-\bar{\mu}_e$ .....	74
3.13	Experimental setup .....	75
3.14	Experimental data .....	76
4.1	Field lines of the Poynting vector for a linear dipole .....	79
4.2	A dipole is located on the $z$ -axis, a distance $H$ above a mirror .....	80
4.3	The plane through the dipole which is perpendicular to $\mathbf{\epsilon}'$ .....	86
4.4	Four-vortex structure .....	87
4.5	The field lines of the Poynting vector for a dipole oscillating above mirror .....	89
4.6	The function $v(h)$ .....	92

4.7	Energy flow lines for a dipole oscillating above mirror when $h = 4.5$ .....	93
4.8	Field lines in the $yz$ -plane .....	94
4.9	Enlargement of the vortex $c$ of Fig. 4.8 .....	96
4.10	The field line pattern for a dipole oscillating perpendicular to the plane of the mirror at a distance $h = 2\pi$ .....	97
4.11	Field lines for a dipole oscillating parallel to the surface at a distance $h = 2\pi$ ....	98
4.12	The solutions of $\text{Re } B_x = 0$ and $\text{Im } B_x = 0$ .....	100
4.13	A field point in the $xy$ -plane is represented by the position vector $\mathbf{q}$ .....	103
4.14	The field lines in the plane of the mirror (for $\tan \gamma > 0$ ) .....	105
5.1	A plane wave with wave vector $\mathbf{k}$ is incident upon an interface .....	111
5.2	The same plane wave incident upon a NIM.....	112
5.3	Light from a point source is incident upon a layer of dielectric material (left) and a ray diagram for a slab of NIM (right).....	113
5.4	Two field lines of the Poynting vector for the radiation emitted by a rotating dipole moment embedded in a dielectric.....	115
5.5	Energy flow field lines for emission of radiation by a particle embedded in a NIM.....	116
6.1	Gold nano-particle embedded in tissue and exposed to external microwaves ....	125

# CHAPTER I

## INTRODUCTION

### 1.1 Background

The near field of a localized source or the diffracted probe light by a nanoscale object can have a very intricate structure in close vicinity of the source or scatterer, including singularities and optical vortices. The first prediction of an optical vortex on a sub-wavelength scale was made by Braunbek and Laukien [1]. They considered a half-infinite thin conducting sheet (the Sommerfeld half-plane), illuminated by a monochromatic plane wave under normal incidence. They found numerically that an optical vortex in the field lines of the energy flow should appear at the illuminated side of the half-plane, somewhere near the edge. At the center of this vortex is a phase singularity. A singular point of a radiation field is usually defined as a point where the amplitude of the electric field vanishes, leaving the phase of the optical field undefined [2]. At such a point, the Poynting vector also vanishes. When a field line of the Poynting vector approaches a singular point, then the field line can either end at that point or bend around it. Another possibility is that there are closed-loop field lines around the singular point, representing a circulation of energy around the singularity.

Vortices around singular points have been predicted in the diffracted field of a plane wave by a sub-wavelength slit in a screen [3,4], in interference patterns between three

plane waves [5] and in the focal plane of a focusing lens [6-9]. By far the most studied optical vortices are the vortices in the field of a Laguerre-Gaussian laser beam [10-13]. The dimension of an optical vortex is of the order of the wavelength of the light, or less. When a vortex appears in a diffraction pattern around an edge, like for the half-plane, the distance between the singular point of the vortex and the screen is of the order of an optical wavelength. Optical vortices, loops and knots can be generated in the laboratory by means of interference of light beams [14], and the existence of vortices in the near field can be experimentally verified with interference techniques [15-18]. Such singularities in the radiation field are a result of diffraction and reflection by a device or due to interference.

## 1.2 Overview

The most elementary type of electromagnetic radiation is electric dipole radiation. On one hand, when a source of radiation is small compared to the wavelength of the emitted light, the source is in first approximation an electric dipole, and, on the other hand, the radiation emitted by atoms and molecules is usually electric dipole radiation. As shown in Fig1.1, suppose there is a particle in a laser beam. If the laser beam hits the particle, it will induce a dipole moment. For instance, when an atom is placed in the laser beam, it will absorb a photon and jump to an excited electronic state. In a subsequent spontaneous decay, a fluorescent photon will be emitted in the form of dipole radiation. In the decay to the lower state, the change in magnetic quantum number is  $\Delta m = -1, 0$  or

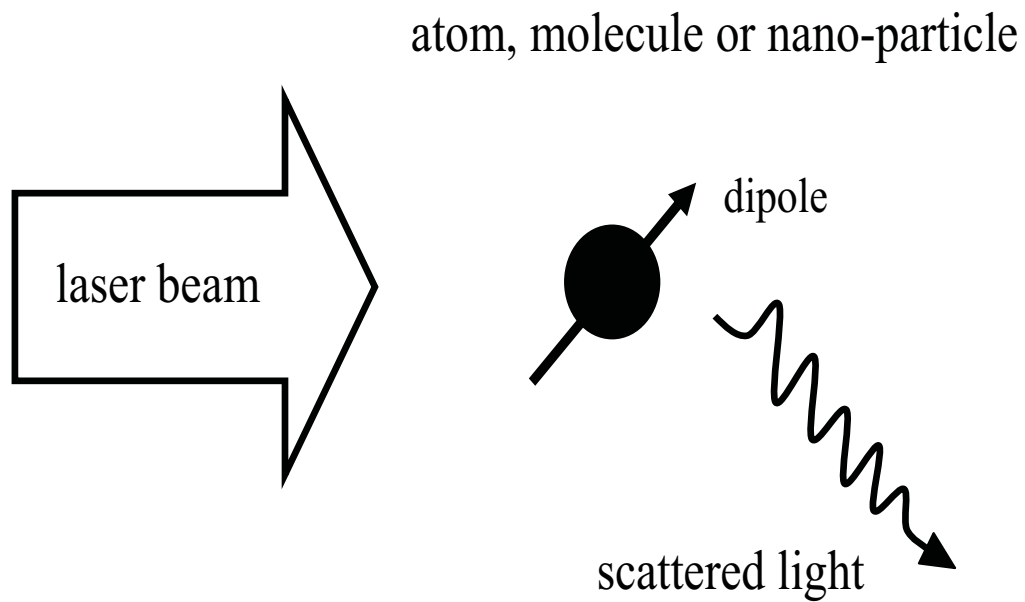


Figure 1.1 Atom, molecule or nano-particle in a laser beam.

1, according to the dipole selection rules. The electric and magnetic fields of an electric dipole are well-known [19], and the emitted power per unit solid angle can be obtained easily, giving the familiar lobe structure for a linearly-oscillating dipole moment. For a single dipole, located at the origin of coordinates, the light appears to be emanating from the location of the dipole, when viewed from the far field. The wave fronts propagate as spherical outgoing waves centered around the dipole and the corresponding optical rays (the orthogonal trajectories of the wave fronts) are therefore straight lines which appear to come from the location of the source. This situation is illustrated in Fig. 1.2.

In the geometrical optics limit of light propagation certain terms in Maxwell's equations are neglected under the assumption that the wavelength of the light is small



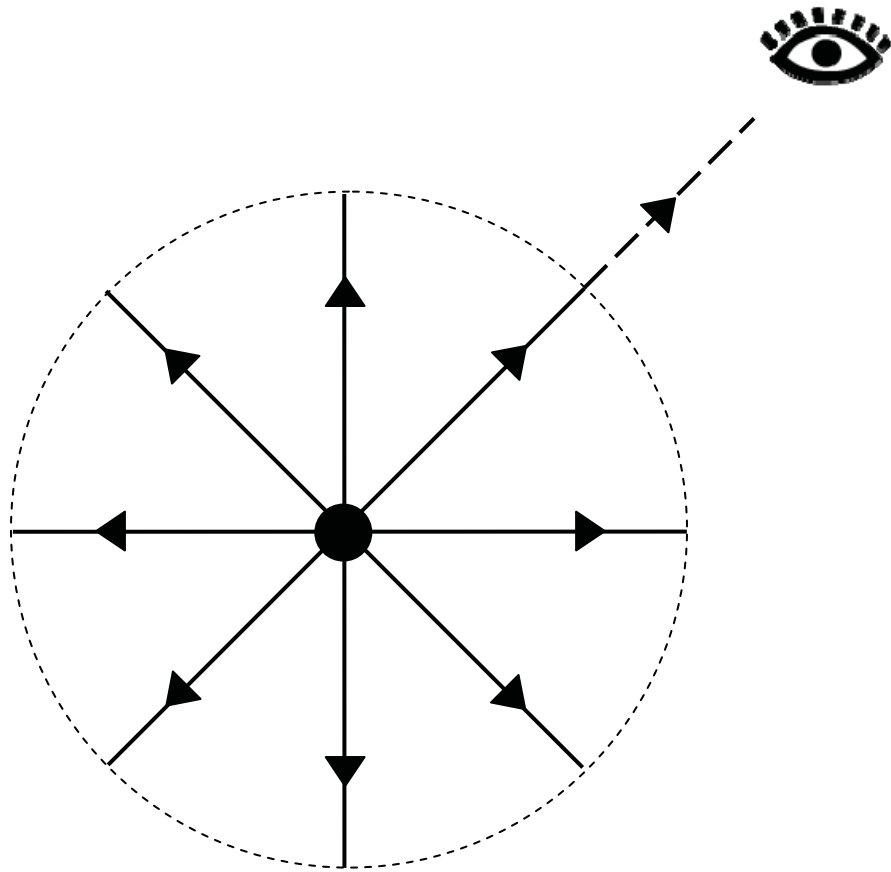


Figure 1.2 The emission of light by a source of radiation.

When observed from a large distance, the light appears to travel along straight lines (rays), which appear to come from the location of the source (the black dot). These lines, with their orientation indicated by the arrow heads, are the field lines of the Poynting vector of the electromagnetic radiation field. The corresponding wave fronts are expanding spheres, and this is shown schematically by the dashed circle. The eye in the figure depicts the position of an observer, far away from the source.

compared to other relevant distances. It can then be shown [20] that the light rays in a homogeneous medium are straight lines, irrespective of the source of the radiation, and that the light rays coincide with the field lines of the Poynting vector. In this limit, the

field lines of the Poynting vector are straight lines at any distance from the source, and in particular in the near field. However, when the structure of dipole radiation is resolved on the scale of a wavelength, the field lines of the Poynting vector are in general curves [21], and they may exhibit a vortex structure near the location of the dipole. In the far field, the field lines are asymptotically straight, but we shall show that when the direction of the emission of radiation is detected with an accuracy of a wavelength or less, the field lines appear to be displaced as compared to the optical rays. With contemporary near-field optical microscopy techniques, the precise details of a radiation pattern have become amenable to experimental observation [22-26], and such measurements with nanoscopic precision may have an impact on novel imaging devices in microbiology and medical applications.

When a small source of radiation is located near an interface, the emitted light that propagates towards the surface partially reflects and partially refracts at the boundary. We shall consider the case where the medium is a perfect mirror, so that all light reflects. The angle of reflection of an optical ray is equal to the angle of incidence, and by considering the path of two rays, as in Fig. 1.3, it appears that a virtual image is formed below the mirror, such that the distance between the object and the mirror is equal to the distance between the image and the mirror. Part of the emitted light travels directly from the source to an observer, and the result is that both the source and the image can be seen. Ray diagrams as in Fig. 1.3 are justified in the geometrical optics limit of light propagation [20] in which variations in the optical field on the scale of a wavelength are

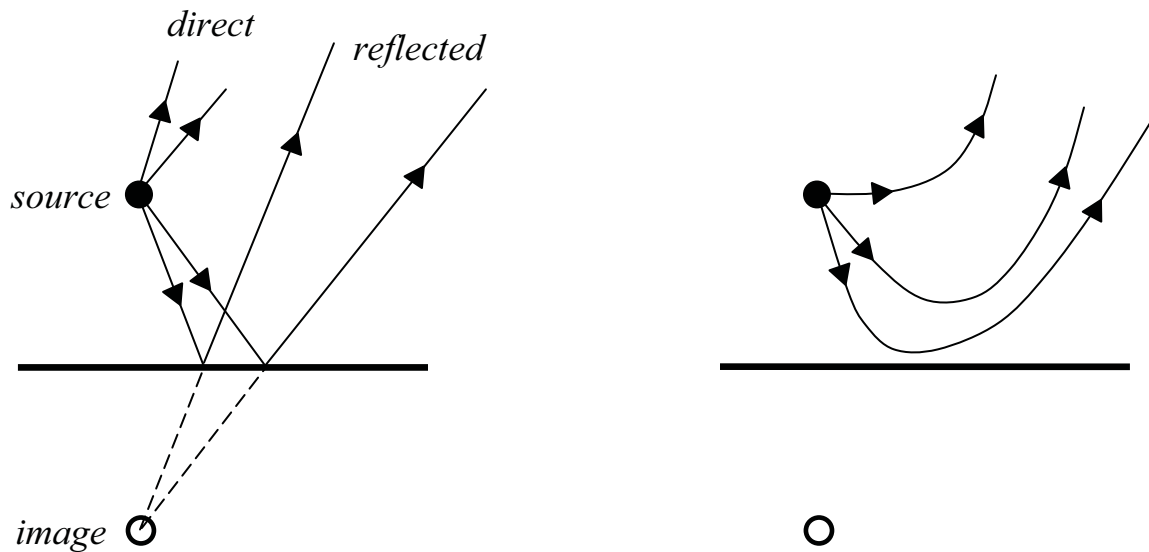


Figure 1.3 Ray diagram for the image formation of a point source near a mirror (left) and a sketch of a possible energy flow pattern (right).

In the geometrical limit of light propagation, the mirror image of an incoherent point source can be constructed by considering the reflection of the optical rays, as shown on the left. For the exact solution of Maxwell's equations the flow of energy is determined by the field lines of the Poynting vector. In contrast to the optical rays, these field lines are smooth curves, as illustrated in the sketch on the right.

neglected. It is furthermore assumed that the source is incoherent, so that any interference between optical rays washes out. In the geometrical optics limit the rays are the orthogonal trajectories of the wave fronts, and for propagation in vacuum it can then be shown that the rays are straight lines. The direction of energy flow in any radiation field is determined by the direction of the electromagnetic Poynting vector, and in the geometrical optics limit the field lines of the Poynting vector coincide with the optical

rays. Therefore, in the geometrical optics limit electromagnetic energy flows along straight lines, which are the optical rays.

When the source of radiation is an atom, a molecule or a nano-particle, driven by a laser beam, the radiation can no longer be considered incoherent, and there will be interference between the different paths of energy propagation. When the source near a mirror is viewed from the far field (many wavelengths away), an interference pattern will be observed, and the source and its image can no longer be distinguished. The ray diagram of Fig. 1.3 is still valid, although its interpretation is then derived from an angular spectrum representation of the source field and the reflected field. In this approach the radiated electric and magnetic fields are represented by superpositions of traveling and evanescent plane waves [27-38]. In the far field, only the plane waves survive, and it can be shown by asymptotic expansion of the angular spectrum with the method of stationary phase that the interference pattern in the far field is consistent with the ray diagram of Fig. 1.3. For a coherent source, however, the rays in Fig. 1.3 are not the paths of energy propagation anymore, but rather visualizations of the wave vectors of the traveling waves in an angular spectrum representation.

In near-field optics and nano-photonics variations in the optical field on the scale of a wavelength are of interest and objects may be located at a sub-wavelength distance from an interface. Then the geometrical optics limit breaks down, whether the source is coherent or not. When measurements are performed in the near-field, then an interpretation of the the ray diagram of Fig. 1.3 also loses its significance in terms of the

angular spectrum, since the near field is dominated by the evanescent waves. In any case, when sub-wavelength phenomena are of interest, the exact solution of Maxwell's equations has to be adopted. The paths of energy flow are the field lines of the Poynting vector, and these field lines are usually curves rather than straight lines. Field lines of any vector field can not cross, whereas the optical rays in Fig. 1.3 do cross. So when considering the flow of energy out of a source near a mirror, we expect a smooth flow pattern as in the sketch in Fig. 1.3. Near the interface, the Poynting vector is tangential to the boundary, as follows from the boundary conditions of Maxwell's equations, and therefore the field lines reflect smoothly at the mirror. This in contrast to the reflection in the ray picture in Fig. 1.3 where the rays make a sharp turn at the interface.

For the construction of the image with a ray diagram, as in Fig. 1.3, the details of the source are irrelevant, whereas for the flow line picture in Fig. 1.3 the details of the flow pattern will depend on the precise structure of the source. We shall consider the emission of radiation by a harmonically oscillating linear dipole near a mirror. It will turn out that the flow line picture is generally far more complicated than suggested in Fig. 1.3, and we shall also show that the process of emission of radiation is drastically altered due to the presence of the mirror.

Understanding the energy emission pattern of a small source and the energy flow distribution in simple systems may have an impact on near field imaging with nanoscale resolution, for instance of biomolecules. Particularly interesting are our results concerning the influence of an interface. Due to reflection of the emitted radiation by the

interface, interference patterns appear, as one could expect. However, we shall also show that the interface changes the emission mechanism of the radiation, which is a counterintuitive result.

The results presented in this thesis have been published in a series of ten publications, which are listed in Appendix E. A full text pdf version of each paper can be found at the Theoretical Optics website, <http://hfa1.physics.msstate.edu/> .

CHAPTER II  
NANOSCALE STRUCTURE OF THE ENERGY FLOW LINES FOR DIPOLE  
RADIATION IN FREE SPACE

An oscillating electric dipole emits radiation, and the flow of energy in the electromagnetic field is represented by the field lines of the Poynting vector. In the most general state of oscillation the dipole moment vector traces out an ellipse. In this chapter, we have evaluated analytically and numerically the field lines of the Poynting vector for the emitted light, and it appears that each field line lies on a cone, which has its axis perpendicular to the plane of the ellipse. The field lines exhibit a vortex structure near the location of the dipole, and they approach a straight line in the far field. The spatial extent of the optical vortex is well below the wavelength of the emitted radiation, and hence is of nanoscale dimension for optical radiation. It is shown that due to the spiraling of the field lines near the source, the asymptotic limit of a field line is displaced as compared to a ray which would come directly out of the source. The magnitude of the displacement of the image in the far field is of the same order of magnitude as the spatial extent of the vortex structure near the source.

## 2.1 The Poynting Vector for Electric Dipole Radiation

When the current density in a localized source of radiation oscillates harmonically with angular frequency  $\omega$ , it has an electric dipole moment given by

$$\mathbf{d}(t) = \text{Re}(\mathbf{d} e^{-i\omega t}) , \quad (2.1)$$

where the complex amplitude  $\mathbf{d}$  is a complex-valued vector, which is determined by the current distribution of the source. Throughout this thesis, a non-italic bold face letter indicates a vector. It will be assumed that higher order multipole moments of the current density contribute negligibly to the radiation field, when compared to the electric dipole moment contribution. The radiated electric field will also have a harmonic time dependence, and can therefore be written as

$$\mathbf{E}(\mathbf{r}, t) = \text{Re}[\mathbf{E}(\mathbf{r}) e^{-i\omega t}] , \quad (2.2)$$

with  $\mathbf{E}(\mathbf{r})$  the complex amplitude, and the radiated magnetic field  $\mathbf{B}(\mathbf{r}, t)$  can be represented similarly. The complex amplitudes of the electric and magnetic fields of an electric dipole at the origin of coordinates can be represented most compactly as

$$\mathbf{E}(\mathbf{r}) = \frac{1}{4\pi\epsilon_0} [k_0^2 \mathbf{d} + (\mathbf{d} \cdot \nabla) \nabla] g(\mathbf{r}) , \quad (2.3)$$

$$\mathbf{B}(\mathbf{r}) = \frac{i\omega\mu_0}{4\pi} \mathbf{d} \times \nabla g(\mathbf{r}) , \quad (2.4)$$

in terms of the wave number  $k_0 = \omega/c$ , and



$$g(\mathbf{r}) = \frac{e^{ik_0 r}}{r} , \quad (2.5)$$

is the free-space Green's function for the scalar Helmholtz equation. Here,  $r = |\mathbf{r}|$  is the distance between the field point  $\mathbf{r}$  and the location of the source. Working out the derivatives gives explicitly

$$\mathbf{E}(\mathbf{r}) = \frac{k_0^3}{4\pi\epsilon_0 q} \{ \mathbf{d} - (\mathbf{d} \cdot \hat{\mathbf{r}})\hat{\mathbf{r}} + [\mathbf{d} - 3(\mathbf{d} \cdot \hat{\mathbf{r}})\hat{\mathbf{r}}] \frac{i}{q} (1 + \frac{i}{q}) \} e^{iq} , \quad (2.6)$$

$$\mathbf{B}(\mathbf{r}) = -\frac{k_0^3}{4\pi\epsilon_0 c q} \mathbf{d} \times \hat{\mathbf{r}} \left( 1 + \frac{i}{q} \right) e^{iq} , \quad (2.7)$$

where we have set

$$q = k_0 r , \quad (2.8)$$

for the dimensionless distance between the dipole and the field point  $\mathbf{r}$ . Vector  $\hat{\mathbf{r}}$  is the unit vector in the  $\mathbf{r}$  direction, e.g.,  $\hat{\mathbf{r}} = \mathbf{r}/r$ .

The Poynting vector at position  $\mathbf{r}$  and at time  $t$  for an electromagnetic field is in general given by

$$\mathbf{S}(\mathbf{r}, t) = \frac{1}{\mu_0} \mathbf{E}(\mathbf{r}, t) \times \mathbf{B}(\mathbf{r}, t) . \quad (2.9)$$

For a time-harmonic field we can substitute the right-hand side of Eq. (2.2) for  $\mathbf{E}(\mathbf{r}, t)$ , and a similar expression for  $\mathbf{B}(\mathbf{r}, t)$ . This yields

$$\mathbf{S}(\mathbf{r}) = \frac{1}{2\mu_0} \text{Re}[\mathbf{E}(\mathbf{r}) \times \mathbf{B}(\mathbf{r})^*] , \quad (2.10)$$

which now only involves the complex amplitudes of the electric and magnetic fields, rather than the fields themselves. Here, terms that oscillate at twice the optical frequency  $\omega$  have been dropped since they average to zero on a time scale of an optical cycle. Equation (2.10) shows that for any time-harmonic field the (time-averaged) Poynting vector is independent of time  $t$ . The significance of the Poynting vector is as follows. Consider a small fictitious surface area  $dA$  at point  $\mathbf{r}$  in space, and let  $\hat{\mathbf{n}}$  be the unit normal vector on  $dA$ . Then  $\mathbf{S} \cdot \hat{\mathbf{n}}dA$  equals the energy transported through  $dA$  per second, which is the power transported through  $dA$ . We therefore see that the direction of  $\mathbf{S}(\mathbf{r})$  at the field point  $\mathbf{r}$  indicates the direction of energy flow. The Poynting vector  $\mathbf{S}(\mathbf{r})$  determines a vector field around the dipole, and the field lines of this vector field represent the flow pattern of the radiated energy.

When we substitute the right-hand sides of Eqs. (2.6) and (2.7) for the complex amplitudes of the electric and magnetic fields, respectively, we obtain for an electric dipole at the origin of coordinates

$$\mathbf{S}(\mathbf{r}) = \frac{ck_0^4}{32\pi^2 \epsilon_0 r^2} \{ [\mathbf{d} \cdot \mathbf{d}^* - (\hat{\mathbf{r}} \cdot \mathbf{d})(\hat{\mathbf{r}} \cdot \mathbf{d}^*)] \hat{\mathbf{r}} - \frac{2}{q} \left( 1 + \frac{1}{q^2} \right) \text{Im}[(\hat{\mathbf{r}} \cdot \mathbf{d}) \mathbf{d}^*] \} . \quad (2.11)$$

To see the meaning of the various contributions, let us consider a surface area  $dA$  which is part of a sphere with radius  $r$  around the origin. Then we have  $\hat{\mathbf{n}} = \hat{\mathbf{r}}$  for the unit normal on  $dA$ , and the magnitude of  $dA$  equals  $r^2 d\Omega$ , with  $d\Omega$  the solid angle subtended by  $dA$ . In spherical coordinates this is  $d\Omega = \sin \theta d\theta d\phi$ . The emitted power into the solid angle  $d\Omega$  is then

$$\frac{dP}{d\Omega} = r^2 \hat{\mathbf{r}} \cdot \mathbf{S}(\mathbf{r}) , \quad (2.12)$$

and with Eq. (2.11) this becomes

$$\frac{dP}{d\Omega} = \frac{ck_0^4}{32\pi^2 \epsilon_0} [\mathbf{d} \cdot \mathbf{d}^* - (\hat{\mathbf{r}} \cdot \mathbf{d})(\hat{\mathbf{r}} \cdot \mathbf{d}^*)] . \quad (2.13)$$

The term proportional to  $\text{Im}[(\hat{\mathbf{r}} \cdot \mathbf{d})\mathbf{d}^*]$  in Eq. (2.11) gives no contribution to the radial power flow, since the dot product of this term with  $\hat{\mathbf{r}}$  vanishes. We see from expression (2.13) that the power flow into the solid angle  $d\Omega$  is independent of the distance  $r$  between the dipole and the surface element  $dA$ . The total power  $P_0$ , emitted by the dipole, can then be obtained as

$$P_0 = \oint d\Omega \frac{dP}{d\Omega} , \quad (2.14)$$

where the integral runs over the unit sphere. The dependence on the spherical coordinates  $(\theta, \phi)$  in  $dP/d\Omega$  only enters through  $\hat{\mathbf{r}}$ , and the integral in Eq. (2.14) can be evaluated easily. We find

$$P_0 = \frac{ck_0^4}{12\pi\epsilon_0} \mathbf{d} \cdot \mathbf{d}^* . \quad (2.15)$$

In order to make the notation more transparent, we set

$$\mathbf{d} = d_0 \boldsymbol{\varepsilon} , \quad d_0 > 0 , \quad \boldsymbol{\varepsilon} \cdot \boldsymbol{\varepsilon}^* = 1 , \quad (2.16)$$

for the complex amplitude of the dipole moment and we introduce the function

$$\zeta(\theta, \phi) = 1 - (\hat{\mathbf{r}} \cdot \boldsymbol{\varepsilon})(\hat{\mathbf{r}} \cdot \boldsymbol{\varepsilon}^*) \quad . \quad (2.17)$$

This yields the expression

$$\mathbf{S}(\mathbf{r}) = \frac{3P_0}{8\pi r^2} \left\{ \zeta(\theta, \phi) \hat{\mathbf{r}} - \frac{2}{q} \left( 1 + \frac{1}{q^2} \right) \text{Im}[(\hat{\mathbf{r}} \cdot \boldsymbol{\varepsilon}) \boldsymbol{\varepsilon}^*] \right\} \quad , \quad (2.18)$$

for the Poynting vector. The total power becomes

$$P_0 = \frac{ck_0^4}{12\pi\varepsilon_0} d_0^2 \quad , \quad (2.19)$$

and the power per unit solid angle takes the form

$$\frac{dP}{d\Omega} = \frac{3}{8\pi} P_0 \zeta(\theta, \phi) \quad . \quad (2.20)$$

The function  $\zeta(\theta, \phi)$ , which appears as the first term in the expression for the Poynting vector, is therefore proportional to the power per unit solid angle for the observation direction  $(\theta, \phi)$ . The second term on the right-hand side of Eq. (2.18), which is proportional to  $\text{Im}[(\hat{\mathbf{r}} \cdot \boldsymbol{\varepsilon}) \boldsymbol{\varepsilon}^*]$ , has no radial component. If only the first term were present, the Poynting vector would be proportional to  $\hat{\mathbf{r}}$ , and the field lines would run in the radial direction, as in Fig. 1.2. The second term is responsible for a possible curving of the field lines, and we shall see below that this term leads to the appearance of an optical vortex near the location of the dipole.

When the vector  $\boldsymbol{\varepsilon}$  in Eq. (2.16) is real, as for instance in a  $\Delta m = 0$  transition in an atom, the dipole moment given by Eq. (2.1) becomes  $\mathbf{d}(t) = d_0 \boldsymbol{\varepsilon} \cos(\omega t)$ . This

corresponds to a linear dipole moment, oscillating back and forth along the direction of  $\boldsymbol{\varepsilon}$ , and the Poynting vector becomes

$$\mathbf{S}(\mathbf{r}) = \frac{3P_0}{8\pi r^2} \hat{\mathbf{r}} \sin^2 \alpha \quad , \quad (2.21)$$

where  $\alpha$  is the angle between vector  $\boldsymbol{\varepsilon}$  and the observation direction  $\hat{\mathbf{r}}$ . The Poynting vector is in the radial direction for all field points  $\mathbf{r}$ , and therefore the field lines of  $\mathbf{S}(\mathbf{r})$  are straight lines which run radially outward from the location of the dipole, as in Fig. 1.2. The power per unit solid angle is proportional to  $\sin^2 \alpha$ , and this gives the common lobe pattern for dipole radiation.

At a large distance from the dipole, the Poynting vector is approximately

$$\mathbf{S}(\mathbf{r}) \approx \frac{3P_0}{8\pi r^2} \zeta(\theta, \phi) \hat{\mathbf{r}} \quad , \quad (2.22)$$

which is in the radial direction. Therefore, in the far field the field lines approach a straight line, and they have the appearance of running from the location of the dipole directly to the far field. A more careful consideration (below) will show that this only holds when spatial variations on the scale of a wavelength in the far field are neglected.

## 2.2 Magnetic Dipole

Although electric dipole radiation is the most common atomic source of light, magnetic dipole radiation is also of interest. For instance, when an atomic transition is

electric-dipole-forbidden, the atom may emit magnetic dipole radiation. For a time-harmonic source, the time dependent magnetic dipole moment can be written as

$$\mathbf{p}(t) = \text{Re}(\mathbf{p} e^{-i\omega t}) , \quad (2.23)$$

in analogy to Eq. (2.1) for the electric dipole moment. The complex amplitudes for the electric and magnetic fields now become

$$\mathbf{E}(\mathbf{r}) = -\frac{i\omega\mu_0}{4\pi} \mathbf{p} \times \nabla g(\mathbf{r}) , \quad (2.24)$$

$$\mathbf{B}(\mathbf{r}) = \frac{\mu_0}{4\pi} [k_0^2 \mathbf{p} + (\mathbf{p} \cdot \nabla) \nabla] g(\mathbf{r}) , \quad (2.25)$$

and this yields explicitly

$$\mathbf{E}(\mathbf{r}) = \frac{k_0^3}{4\pi\epsilon_0 c q} \mathbf{p} \times \hat{\mathbf{r}} \left( 1 + \frac{i}{q} \right) e^{iq} , \quad (2.26)$$

$$\mathbf{B}(\mathbf{r}) = \frac{\mu_0 k_0^3}{4\pi q} \left\{ \mathbf{p} - (\mathbf{p} \cdot \hat{\mathbf{r}}) \hat{\mathbf{r}} + [\mathbf{p} - 3(\mathbf{p} \cdot \hat{\mathbf{r}}) \hat{\mathbf{r}}] \frac{i}{q} \left( 1 + \frac{i}{q} \right) \right\} e^{iq} . \quad (2.27)$$

Then we set

$$\mathbf{p} = p_0 \boldsymbol{\varepsilon} , \quad p_0 > 0 , \quad \boldsymbol{\varepsilon} \cdot \boldsymbol{\varepsilon}^* = 1 , \quad (2.28)$$

as in Eq. (2.16) for the electric dipole. Computation of the corresponding Poynting vector then gives again expression (2.18), with the total power now given by

$$P_0 = \frac{k_0^4}{12\pi\epsilon_0 c} p_0^2 . \quad (2.29)$$

Therefore, apart from the different expressions for  $P_0$ , the Poynting vector for a magnetic dipole in free space is the same as the Poynting vector for an electric dipole with the same  $\boldsymbol{\varepsilon}$ , and consequently the field line patterns are the same for both types of dipoles.

### 2.3 Elliptical Dipole Moment

When an atom in an excited electronic state decays to a lower state in a  $\Delta m = \mp 1$  transition, the vector  $\boldsymbol{\varepsilon}$  in Eq. (16) is the spherical unit vector

$$\mathbf{e}_{\pm 1} = -\frac{1}{\sqrt{2}}(\pm \mathbf{e}_x + i \mathbf{e}_y) . \quad (2.30)$$

The dipole moment  $\mathbf{d}(t)$  then traces out a circle in the  $xy$ -plane, and the rotation is positive (counterclockwise when viewed from the positive  $z$ -axis) for  $\boldsymbol{\varepsilon} = \mathbf{e}_1$  and negative for  $\boldsymbol{\varepsilon} = \mathbf{e}_{-1}$ . In general, however, the complex amplitude  $\mathbf{d}$  of the dipole moment can be any complex-valued vector. It can then be shown [39,40] that the most general state of rotation of  $\mathbf{d}(t)$  is an ellipse. We can then take the plane of this ellipse as the  $xy$ -plane, and parametrize vector  $\boldsymbol{\varepsilon}$  as

$$\boldsymbol{\varepsilon} = -\frac{1}{\sqrt{\beta^2 + 1}}(\beta \mathbf{e}_x + i \mathbf{e}_y) , \quad (2.31)$$

with  $\beta$  real. With Eq. (2.1) this yields

$$\mathbf{d}(t) = -\frac{d_0}{\sqrt{\beta^2 + 1}}[\beta \mathbf{e}_x \cos(\omega t) + \mathbf{e}_y \sin(\omega t)] , \quad (2.32)$$

and this ellipse is shown in Fig. 2.1. For  $|\beta| < 1$ , as in the figure, the major axis is along the  $y$ -axis and the minor axis is along the  $x$ -axis. For  $|\beta| > 1$  the major axis is along the  $x$ -axis and the minor axis is along the  $y$ -axis. For  $\beta > 0$  ( $\beta < 0$ ) the rotation is positive (negative) and for  $\beta = \pm 1$ , vector  $\boldsymbol{\varepsilon}$  becomes  $\mathbf{e}_{\pm 1}$ , and the ellipse reduces to a circle. Furthermore, for  $\beta = 0$  and  $\beta \rightarrow \infty$  we recover the case of a linear dipole, oscillating along the  $y$ -axis and  $x$ -axis, respectively. As shown in Fig. 2.1, as time progresses, vector  $\mathbf{d}(t)$  traces out an ellipse, and we take the plane of the ellipse as the  $xy$ -plane. The ellipse is parametrized with  $\beta$ , as in Eq. (2.32), and the figure shows the dependence on  $\beta$  of the semi-major and semi-minor axes. For  $\beta = 0$ , the oscillation becomes linear along the  $y$ -axis, and for  $\beta = 1$  the ellipse reduces to a circle. For  $\beta > 1$  the major axis is along the  $x$ -axis, and for  $\beta \rightarrow \infty$  the oscillation becomes linear along the  $x$ -axis. For  $\beta$  positive, as in the figure, the rotation is counterclockwise and for  $\beta$  negative the rotation becomes clockwise.

With  $\boldsymbol{\varepsilon}$  given by Eq. (2.31), the Poynting vector from Eq. (2.18) becomes

$$\mathbf{S}(\mathbf{r}) = \frac{3P_0}{8\pi r^2} \left\{ \zeta(\theta, \phi) \hat{\mathbf{r}} + \frac{2}{q} \left( 1 + \frac{1}{q^2} \right) \frac{\beta}{\beta^2 + 1} \sin \theta \mathbf{e}_\phi \right\}, \quad (2.33)$$

and for the function  $\zeta(\theta, \phi)$  from Eq. (2.17) we find

$$\zeta(\theta, \phi) = 1 - \frac{1}{2} \sin^2 \theta \left[ 1 + \frac{\beta^2 - 1}{\beta^2 + 1} \cos(2\phi) \right]. \quad (2.34)$$

The term proportional to  $\hat{\mathbf{r}}$  in Eq. (2.33) is the same as the right-hand side of Eq. (2.22),



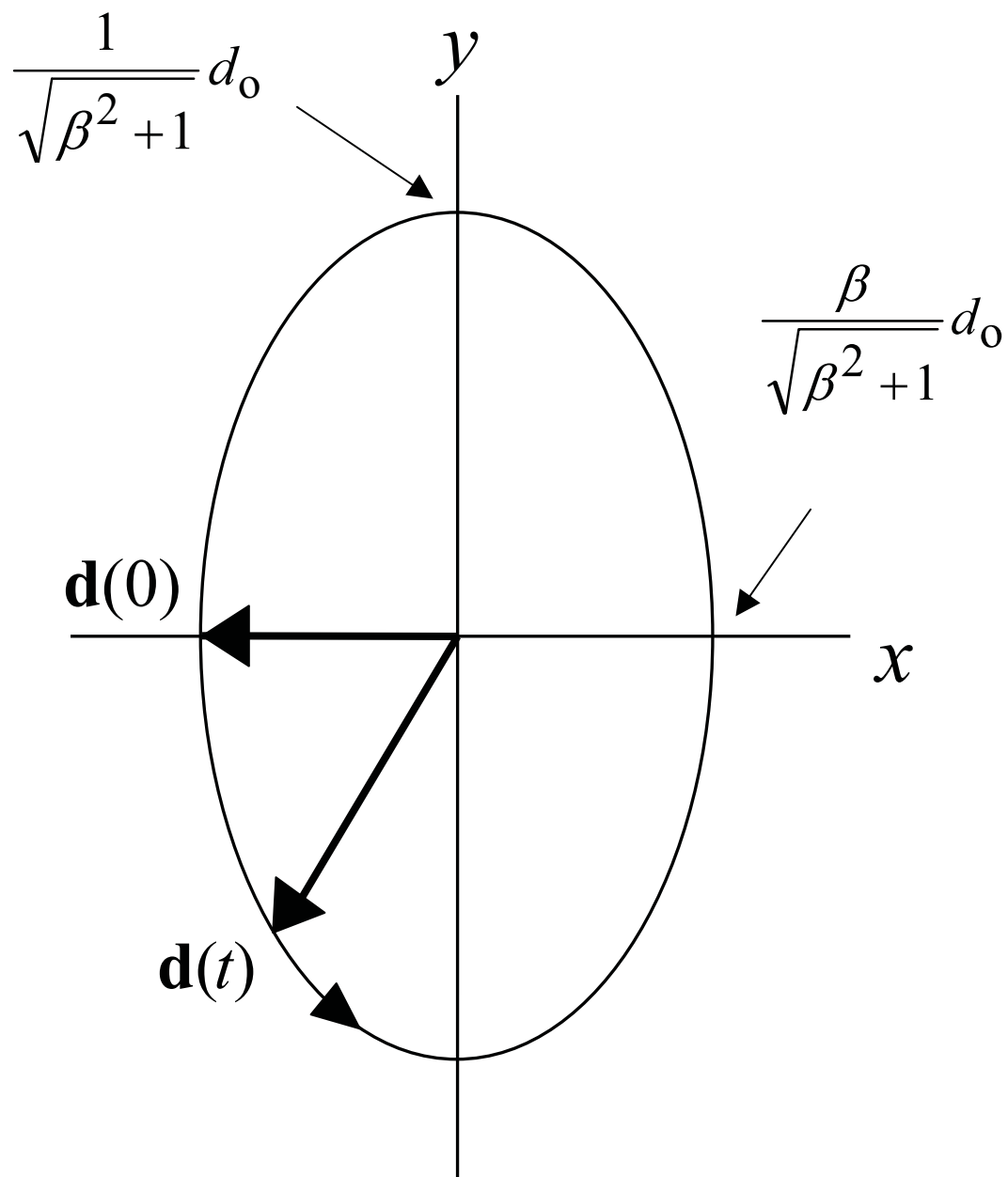


Figure 2.1 The most general state of oscillation of an electric dipole moment  $\mathbf{d}(t)$ .

so this term corresponds to the far-field solution. The term proportional to  $\mathbf{e}_\phi$  is dominant in the near field, since it is proportional to  $r^{-5}$ , and it will give rise to a rotation of the field lines around the  $z$ -axis. For  $\beta = 0$  and  $\beta \rightarrow \infty$  this term vanishes, and the field lines are in the radial direction at any distance from the dipole, as in Fig. 1.2.

## 2.4 Field Lines of the Poynting Vector

Expression (2.33) for  $\mathbf{S}(\mathbf{r})$  defines a vector field in space, and a field line of  $\mathbf{S}(\mathbf{r})$  is a curve for which at any point along the curve the vector  $\mathbf{S}(\mathbf{r})$  is on its tangent line. Let  $\mathbf{r}(u)$  be a parametrization of a field line, with  $u$  a dummy variable. Since a field line is only determined by the direction of  $\mathbf{S}(\mathbf{r})$ , and not its magnitude, the field lines are solutions of

$$\frac{d\mathbf{r}}{du} = f(\mathbf{r})\mathbf{S}(\mathbf{r}) \quad , \quad (2.35)$$

with  $f(\mathbf{r})$  an arbitrary positive function of  $\mathbf{r}$ . In spherical coordinates  $(q, \theta, \phi)$ , with  $q = k_0 r$ , Eq. (2.35) becomes

$$\frac{dq}{du} = k_0 f(\mathbf{r}) \hat{\mathbf{r}} \cdot \mathbf{S}(\mathbf{r}) \quad , \quad (2.36)$$

$$q \frac{d\theta}{du} = k_0 f(\mathbf{r}) \mathbf{e}_\theta \cdot \mathbf{S}(\mathbf{r}) \quad , \quad (2.37)$$

$$q \sin \theta \frac{d\phi}{du} = k_0 f(\mathbf{r}) \mathbf{e}_\phi \cdot \mathbf{S}(\mathbf{r}) \quad , \quad (2.38)$$

which is a set of equations for  $q$ ,  $\theta$  and  $\phi$  as functions of  $u$ . To simplify the equations

we take

$$f(\mathbf{r}) = \frac{8\pi r^2}{3P_0 k_0} , \quad (2.39)$$

and with Eq. (2.33) for  $\mathbf{S}(\mathbf{r})$  we then obtain

$$\frac{dq}{du} = \zeta(\theta, \phi) , \quad (2.40)$$

$$\frac{d\theta}{du} = 0 , \quad (2.41)$$

$$\frac{d\phi}{du} = \frac{2}{q^2} \left( 1 + \frac{1}{q^2} \right) \frac{\beta}{\beta^2 + 1} . \quad (2.42)$$

The solution of Eq. (2.41) is  $\theta = \theta_0$ , with  $\theta_0$  a constant. Therefore, any field line lies on a cone  $\theta = \theta_0$ . Then in Eq. (2.40) we can replace  $\zeta(\theta, \phi)$  by  $\zeta(\theta_0, \phi)$ , and when combined with Eq. (2.42) this yields

$$\frac{d\phi}{dq} = \frac{2}{q^2} \left( 1 + \frac{1}{q^2} \right) \frac{1}{\zeta(\theta_0, \phi)} \frac{\beta}{\beta^2 + 1} , \quad (2.43)$$

which is an ordinary first-order nonlinear differential equation for  $\phi(q)$ . We shall solve this equation in the next section.

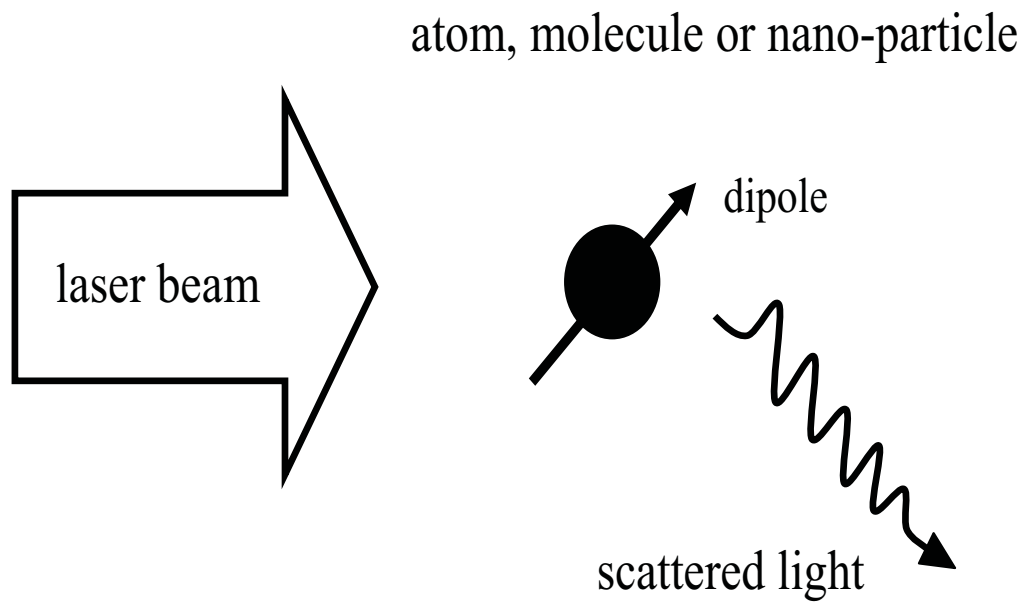


Figure 1.1 Atom, molecule or nano-particle in a laser beam.

1, according to the dipole selection rules. The electric and magnetic fields of an electric dipole are well-known [19], and the emitted power per unit solid angle can be obtained easily, giving the familiar lobe structure for a linearly-oscillating dipole moment. For a single dipole, located at the origin of coordinates, the light appears to be emanating from the location of the dipole, when viewed from the far field. The wave fronts propagate as spherical outgoing waves centered around the dipole and the corresponding optical rays (the orthogonal trajectories of the wave fronts) are therefore straight lines which appear to come from the location of the source. This situation is illustrated in Fig. 1.2.

In the geometrical optics limit of light propagation certain terms in Maxwell's equations are neglected under the assumption that the wavelength of the light is small

the range

$$-\infty < \phi < \phi_0 \quad , \quad \beta > 0 \quad , \quad (2.47)$$

$$\phi_0 < \phi < \infty \quad , \quad \beta < 0 \quad , \quad (2.48)$$

as follows from the arguments above.

Equation (2.46) can be solved explicitly, provided we consider  $\phi$  as the independent variable rather than  $q$ . When we introduce the function

$$A(\phi) = \frac{3}{8} \left( \beta - \frac{1}{\beta} \right) \sin^2 \theta_0 [\sin(2\phi) - \sin(2\phi_0)] - \frac{3}{2} \left( \beta + \frac{1}{\beta} \right) \left( 1 - \frac{1}{2} \sin^2 \theta_0 \right) (\phi - \phi_0) \quad , \quad (2.49)$$

then Eq. (2.46) becomes

$$A(\phi) = \frac{1}{q} \left( 3 + \frac{1}{q^2} \right) \quad , \quad (2.50)$$

which is a cubic equation in  $1/q$ . The solution for  $q(\phi)$  is

$$q(\phi) = \frac{1}{\left[ \sqrt{1 + \frac{1}{4} A(\phi)^2} + \frac{1}{2} A(\phi) \right]^{\frac{1}{3}} - \left[ \sqrt{1 + \frac{1}{4} A(\phi)^2} - \frac{1}{2} A(\phi) \right]^{\frac{1}{3}}} \quad . \quad (2.51)$$

The dimensionless Cartesian coordinates of a point on a field line are therefore parametrized by

$$\bar{x} = q(\phi) \sin \theta_0 \cos \phi \quad , \quad (2.52)$$

$$\bar{y} = q(\phi) \sin \theta_0 \sin \phi \quad , \quad (2.53)$$

$$\bar{z} = q(\phi) \cos \theta_0 \quad , \quad (2.54)$$

with  $\bar{x} = k_0 x$ ,  $\bar{y} = k_0 y$  and  $\bar{z} = k_0 z$ , and the parameter  $\phi$  is chosen as in Eq. (2.47) or (2.48), depending on the sign of  $\beta$ .

For the numerical evaluation of points on a field line we use *Mathematica*, and the graphs are made in *SigmaPlot*. Figure 2.2 shows a field line for a circular dipole, rotating in the positive direction ( $\beta = 1$ ), and the observation angles are  $\theta_0 = \pi/4$  and  $\phi_0 = \pi/2$ . The field line lies on a cone, and it has a vortex structure near the site of the dipole. The spatial extent of the vortex is a fraction of a wavelength, as can be seen from the figure. Figure 2.3 shows several field lines for the same values of  $\phi_0$  and  $\beta$  as in Fig. 2.2, but here each field line has a different value of  $\theta_0$ . The emerging field line pattern consists of cones around the  $z$ -axis, and on each cone we have a line swirling around. A similar picture holds for the region  $z < 0$ , but it would not be clear if these lines were drawn in the same figure.

Each field line lies on a cone with its axis as the  $z$ -axis, and the field lines turn around the  $z$ -axis with a positive orientation. Asymptotically, the field lines run into the direction of the positive  $y$ -axis for the example in Fig. 2.3, since we have  $\phi_0 = \pi/2$ . For the dimensionless coordinates we have  $\bar{x} = k_0 x$ , etc., so a dimensionless distance of  $2\pi$  corresponds to one optical wavelength. We then see from the figure that the spatial extent of this optical vortex is a fraction of a wavelength. For optical radiation, with a wavelength of several hundred nanometers, the vortex manifests itself on a scale of less than 100 nm. With contemporary high-precision nanoscale experimental techniques, such a vortex should be accessible to detection.

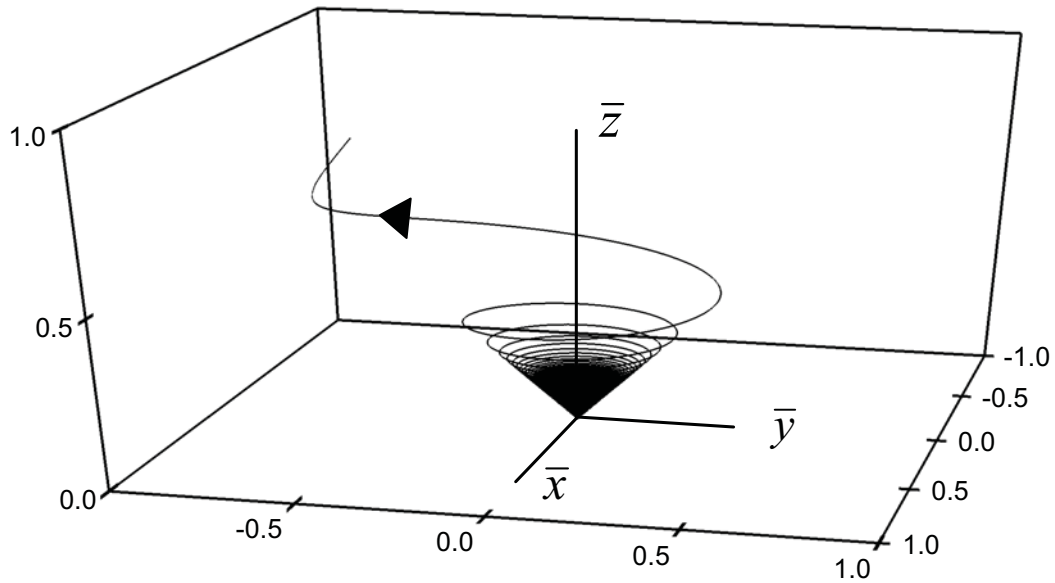


Figure 2.2 A typical field line of the Poynting vector for the radiation emitted by an electric dipole with  $\beta = 1$ , located at the origin of coordinates.

The field line lies on a cone (of  $45^\circ$  with the  $z$ -axis for this example). Near the source, the field line rotates numerous times around the  $z$ -axis, and this gives the vortex structure in the near-field emission pattern. We use dimensionless variables  $\bar{x} = k_0 x$ , etc., so that a distance of  $2\pi$  corresponds to one optical wavelength. We then see from the figure that the spatial extent of the vortex is a fraction of a wavelength.

Figure 2.4 shows several field lines for  $\beta = 1$ . For the field lines in the region  $z > 0$  we have chosen  $\theta_0 = \pi/4$ , and each field line has a different value of  $\phi_0$ . This figure illustrates how various field lines on a cone run off in different directions for different values of  $\phi_0$ . For the field lines below the  $xy$ -plane, we have used the same values of  $\phi_0$  as for the region  $z > 0$ , but  $\theta_0$  is equal to  $3\pi/4$ . The orientation of the field lines with

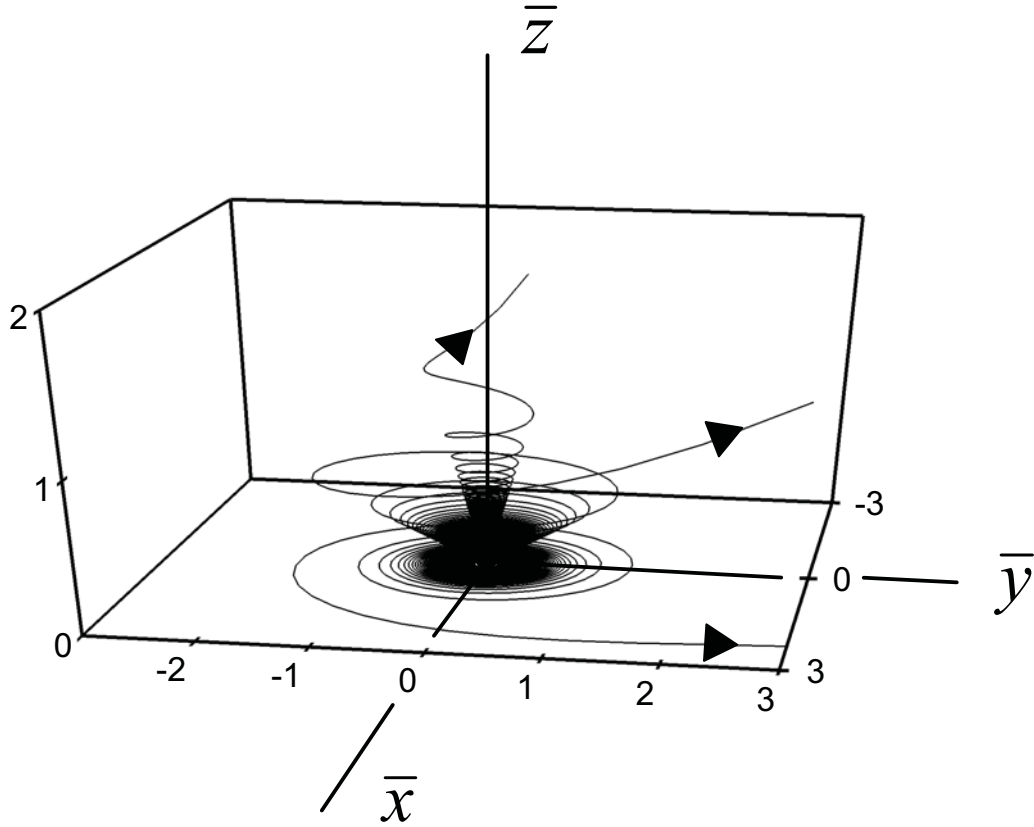


Figure 2.3 Three field lines of the Poynting vector for  $\beta = 1$  and  $\phi_0 = \pi/2$ .

Shown are field lines for three different values of  $\theta_0$ . Shown in the figure are  $\theta_0 = \pi/8$ ,  $3\pi/8$  and  $\pi/2$ . Each field line lies on the corresponding cone, and leaves into the positive  $y$ -direction.

respect to the  $z$ -axis is the same in  $z > 0$  and in  $z < 0$ . The dependence of the vortex structure on the value of  $\beta$  is illustrated in Figs. 2.5 and 2.6. Figure 2.2 shows the vortex for  $\beta = 1$ , with  $\theta_0 = \pi/4$  and  $\phi_0 = \pi/2$  as the observation angles. Figures 2.5 and 2.6 show field lines for  $\beta = 0.1$  and  $\beta = 0.001$ , respectively, with the values of  $\theta_0$  and  $\phi_0$  the same as in Fig. 2.2. When the value of  $\beta$  decreases, as in Figs. 2.5 and 2.6, we find that the structure of the vortex remains similar, but its spatial extent diminishes.



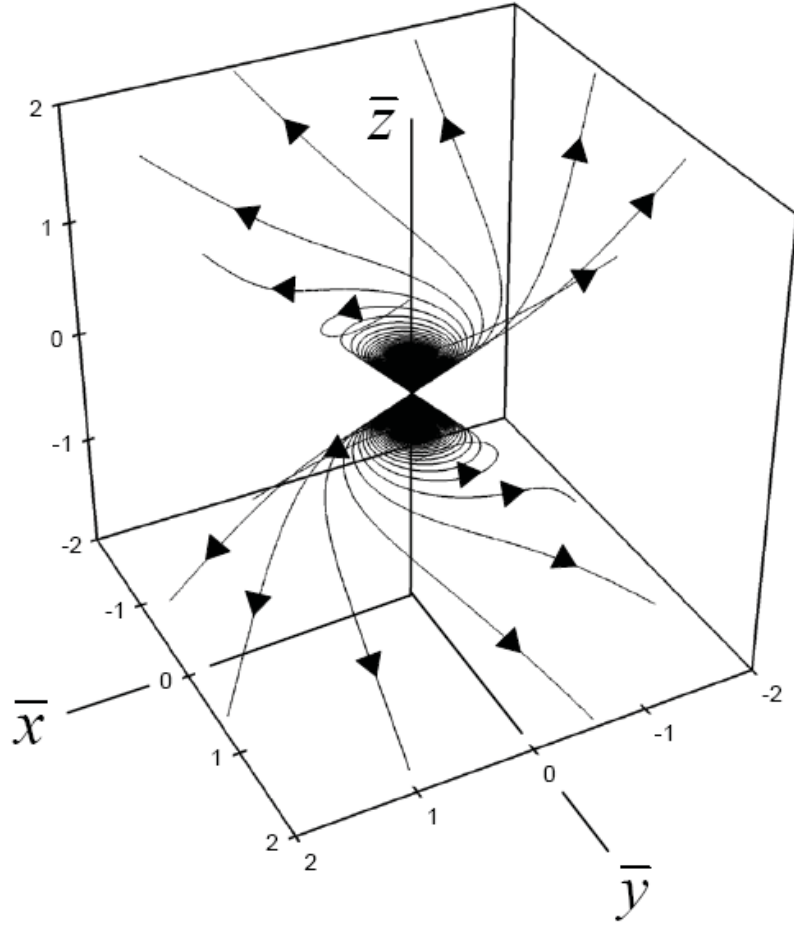


Figure 2.4 Field lines of the Poynting for  $\beta = 1$  and  $\theta_0 = \pi/4$  and  $3\pi/4$ .

The figure shows field lines for a variety of values of  $\phi_0$  with  $\beta$  fixed. The orientation of the field lines in both  $z > 0$  and  $z < 0$  is the same as the direction of rotation of the dipole moment (positive).

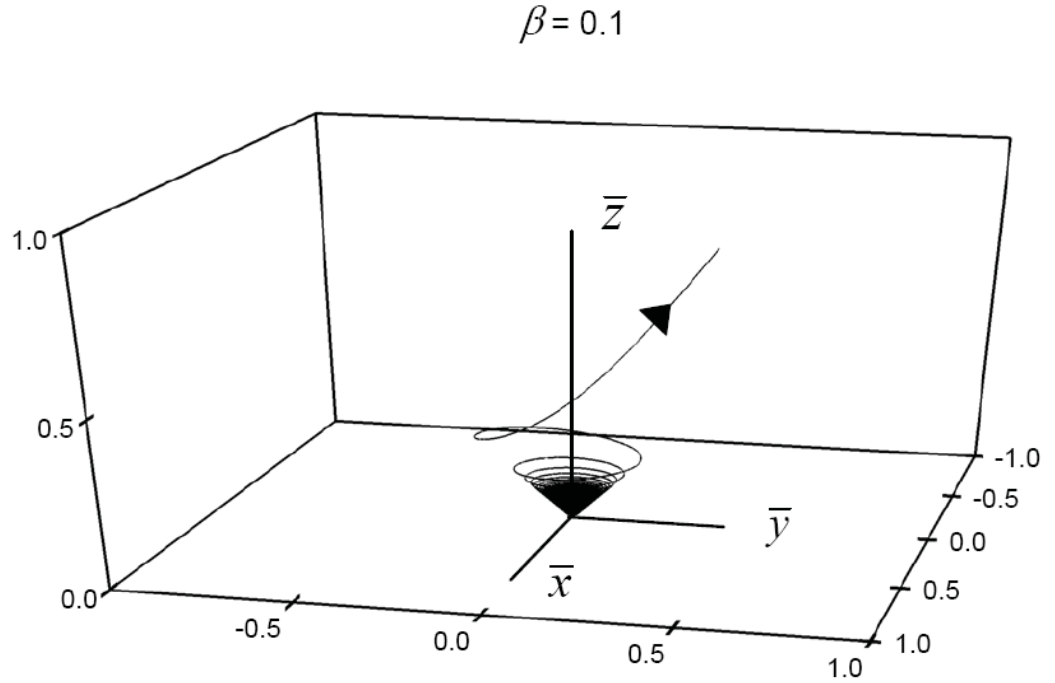


Figure 2.5 Field line for  $\beta = 0.1$ .

The observation direction is  $(\theta_o, \phi_o) = (\pi/4, \pi/2)$ . For this figure, the value of  $\beta$  is equal to 0.1, and the observation angles are the same as for the field line in Fig. 2.2. Comparison of Figs. 2.2 and 2.5 shows that when  $\beta$  decreases, the spatial extent of the vortex decreases.

For  $\beta \rightarrow 0$  the field lines of the Poynting vector should become straight lines, running from the site of the dipole to the far field, since in the limit  $\beta \rightarrow 0$  the oscillation of the dipole becomes linear along the  $y$ -axis. Figures 2.5 and 2.6 show that this transition occurs through a decreasing size of the optical vortex.

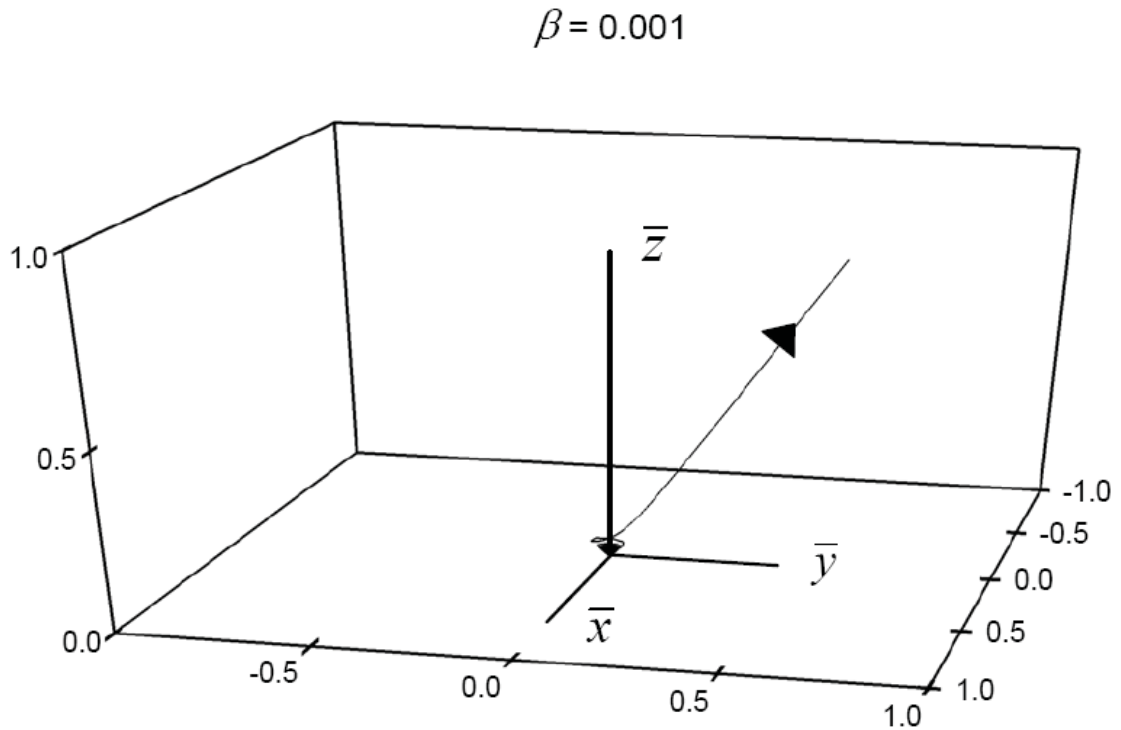


Figure 2.6 Field line for  $\beta = 0.001$ .

For  $\beta \rightarrow 0$  the dipole approaches a linear dipole, oscillating along the  $y$ -axis, for which the field lines are straight, and run radially outward. It appears that this limit is reached in such a way that the spatial extent of the vortex reduces, until it reaches a point for  $\beta \rightarrow 0$ , as can be seen from this figure.

## 2.5 Displacement in the Far Field

Every field line of the Poynting vector approaches a straight line in the far field, which is reminiscent of the optical rays picture for the emission of radiation. Due to the rotation of the field lines near the location of the source, however, these straight lines do not appear to come exactly from the site of the dipole, as depicted in Fig. 2.7.

### 2.5.1 Asymptotic Limit of the Field Lines

In order to obtain the asymptotic limit of the field lines, we consider Eq. (2.43) for  $d\phi/dq$ . For  $q$  large, we can expand  $\phi(q)$  in an asymptotic series as

$$\phi(q) = \phi_0 + \frac{\alpha_1}{q} + \frac{\alpha_2}{q^2} + \dots \quad (2.55)$$

For the function  $\zeta(\theta_0, \phi)$  on the right-hand side of Eq. (2.43) we obtain  $\zeta(\theta_0, \phi) = \zeta(\theta_0, \phi_0) + O(1/q)$ , and the expansion of Eq. (2.43) becomes

$$\frac{d\phi}{dq} = \frac{1}{q^2} Y(\theta_0, \phi_0; \beta) + O\left(\frac{1}{q^3}\right), \quad (2.56)$$

where we have introduced the abbreviation

$$Y(\theta_0, \phi_0; \beta) = \frac{1}{\zeta(\theta_0, \phi_0)} \frac{2\beta}{\beta^2 + 1}. \quad (2.57)$$

Integration of Eq. (2.56) then yields the first two terms of the asymptotic series

$$\phi(q) = \phi_0 - \frac{1}{q} Y(\theta_0, \phi_0; \beta) + \dots \quad (2.58)$$

The dimensionless Cartesian coordinates for a point on a field line are given by Eqs. (2.52)-(2.54), in which  $q$  is considered a function of  $\phi$ . We now view  $\phi$  to be a function of  $q$ , and we expand  $\cos \phi$  and  $\sin \phi$  in Eqs. (2.52) and (2.53) for  $q$  large by means of Eq. (2.58). This gives

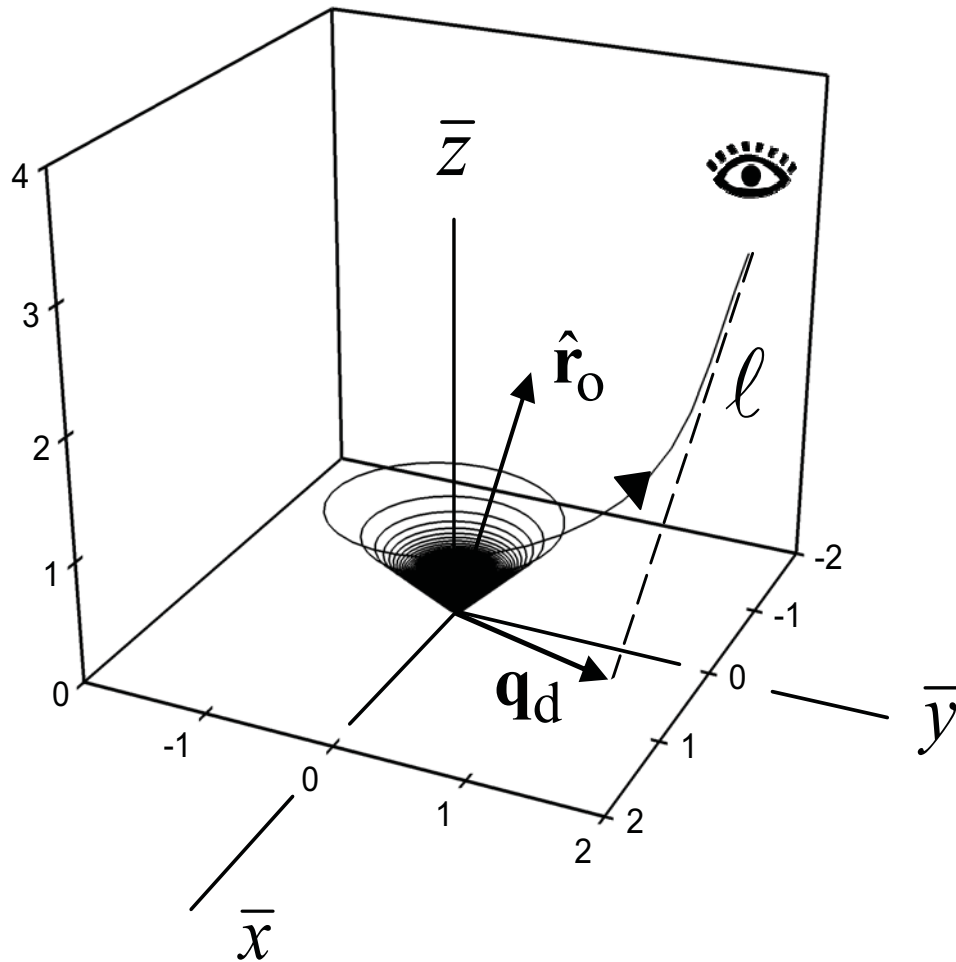


Figure 2.7 A field line approaches asymptotically a line  $\ell$  at a large distance.

When the radiation is detected by an observer in the far field, the field line appears to come from a point in the  $xy$ -plane with position vector  $\mathbf{q}_d$ . Therefore, the source of the radiation appears to be displaced over vector  $\mathbf{q}_d$ . The figure illustrates this displacement for a circular dipole with  $\beta = 1$ , and observation direction  $(\theta_o, \phi_o) = (\pi/4, 0.95\pi)$ .

$$\cos\phi(q) = \cos\phi_0 + \frac{1}{q}Y(\theta_0, \phi_0; \beta)\sin\phi_0 + \dots , \quad (2.59)$$

$$\sin\phi(q) = \sin\phi_0 - \frac{1}{q}Y(\theta_0, \phi_0; \beta)\cos\phi_0 + \dots . \quad (2.60)$$

In Eqs. (2.52) and (2.53) the factors  $\cos\phi$  and  $\sin\phi$  are multiplied by  $q$ , and therefore the second terms on the right-hand sides of Eqs. (2.59) and (2.60) become a constant, independent of  $q$ . The higher-order terms vanish for  $q \rightarrow \infty$ , and therefore the asymptotic limit for the dimensionless Cartesian coordinates becomes

$$\bar{x} = \sin\theta_0[\lambda\cos\phi_0 + Y(\theta_0, \phi_0; \beta)\sin\phi_0] , \quad (2.61)$$

$$\bar{y} = \sin\theta_0[\lambda\sin\phi_0 - Y(\theta_0, \phi_0; \beta)\cos\phi_0] , \quad (2.62)$$

$$\bar{z} = \lambda\cos\theta_0 , \quad (2.63)$$

where we have replaced  $q$  by  $\lambda$ , since this free parameter does not have the significance of the dimensionless distance to the origin anymore in the asymptotic limit. When we let  $-\infty < \lambda < \infty$ , Eqs. (2.61)-(2.63) represent a straight line  $\ell$ , which is the asymptote of the corresponding field line of the Poynting vector. When we set

$$\mathbf{q}_d = Y(\theta_0, \phi_0; \beta)\sin\theta_0(\mathbf{e}_x\sin\phi_0 - \mathbf{e}_y\cos\phi_0) , \quad (2.64)$$

for given  $(\theta_0, \phi_0)$ , then the equation for the line  $\ell$  can be written as

$$\ell: \mathbf{q} = \lambda\hat{\mathbf{r}}_0 + \mathbf{q}_d , \quad (2.65)$$

with  $\mathbf{q} = k_0\mathbf{r}$  the dimensionless position vector for a point on the line  $\ell$ , and  $\hat{\mathbf{r}}_0$  the radial unit vector into the direction of observation  $(\theta_0, \phi_0)$ . The intersection between the

line  $\ell$  and the  $xy$ -plane follows by setting  $\lambda = 0$ , and therefore we see that vector  $\mathbf{q}_d$  is the virtual displacement of the source in the  $xy$ -plane, when viewed from the far field. This result is illustrated in Fig. 2.7. It also follows from Eq. (2.64) that  $\mathbf{q}_d \cdot \hat{\mathbf{r}}_o = 0$ , and therefore the displacement  $\mathbf{q}_d$  is perpendicular to the direction of observation  $\hat{\mathbf{r}}_o$ .

An interesting aspect of the virtual displacement  $\mathbf{q}_d$  of the source in the  $xy$ -plane is that it depends on the observation angles  $\theta_o$  and  $\phi_o$ . Figure 2.8 shows two field lines for which the displacement for both is along the positive  $y$ -axis, and we see from the figure that the magnitude of the displacement is different for both observation directions. For observation along the  $xy$ -plane, the line  $\ell$  is in the  $xy$ -plane, and its intersection point with the  $xy$ -plane should be considered as the limit  $\theta_o \rightarrow \pi/2$  in the general expression (2.64) for  $\mathbf{q}_d$ . Since the line  $\ell$  runs into the direction of  $\hat{\mathbf{r}}_o$ , and since  $\mathbf{q}_d \cdot \hat{\mathbf{r}}_o = 0$ , the displacement vector in the  $xy$ -plane is perpendicular to the asymptote  $\ell$  of the field line. An example of this situation is shown in Fig. 2.9. Figure 2.10 shows several field lines in the  $xy$ -plane, and their corresponding displacement vectors.

### 2.5.2 Displacement Vector

When a field line is observed in the far field, it appears to come from the point with position vector  $\mathbf{q}_d$  in the  $xy$ -plane, as shown in Fig. 2.7. From a different point of view, the observation plane of an observer in the far field, located at angular position  $(\theta_o, \phi_o)$ , is a plane perpendicular to  $\hat{\mathbf{r}}_o$ , at a large distance from the source. When a field line would run straight from the source to the observer, it would intersect the observation

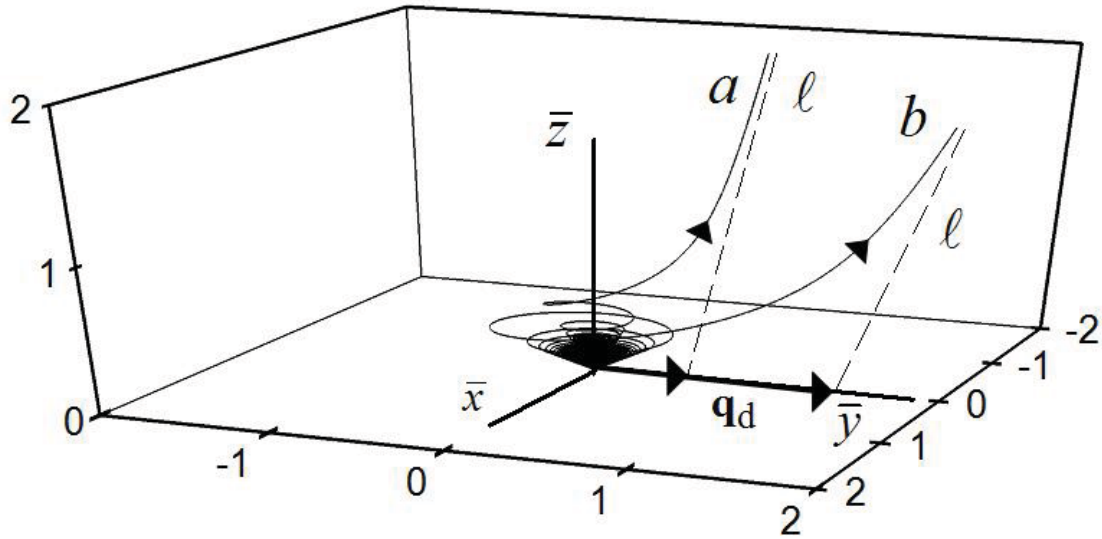


Figure 2.8 Dependence of the displacement on  $\theta_0$ .

Far away from the source the field lines approach straight lines, indicated by  $\ell$ . The figure shows field lines for  $\beta=1$ ,  $\phi_0 = \pi$ , and curves  $a$  and  $b$  correspond to observation angles  $\theta_0 = \pi/6$  and  $\theta_0 = \pi/3$ , respectively. When viewed from the far field, a curved field line is indistinguishable from the asymptotic line  $\ell$ , and this gives rise to an apparent displacement of the source. The image point in the  $xy$ -plane is the intersection between  $\ell$  and the  $xy$ -plane, and the location of this point is represented by the displacement vector  $\mathbf{q}_d$ . Clearly, the displacement depends on the direction of observation.

plane at the local origin of coordinates  $O'$ , as shown in Fig. 2.11, but due to the rotation of the field lines near the source the field line intersects this plane at a different point. At a large distance, this point is the same as the intersection of the plane with the line  $\ell$ . The displacement vector  $\mathbf{q}_d$  from Eq. (2.64) can be written as

$$\mathbf{q}_d = -\mathbf{e}_{\phi_0} Y(\theta_0, \phi_0; \beta) \sin \theta_0, \quad (2.66)$$

with  $\mathbf{e}_{\phi_0}$  the local unit vector  $\mathbf{e}_\phi$  in a spherical coordinate system, and evaluated at the



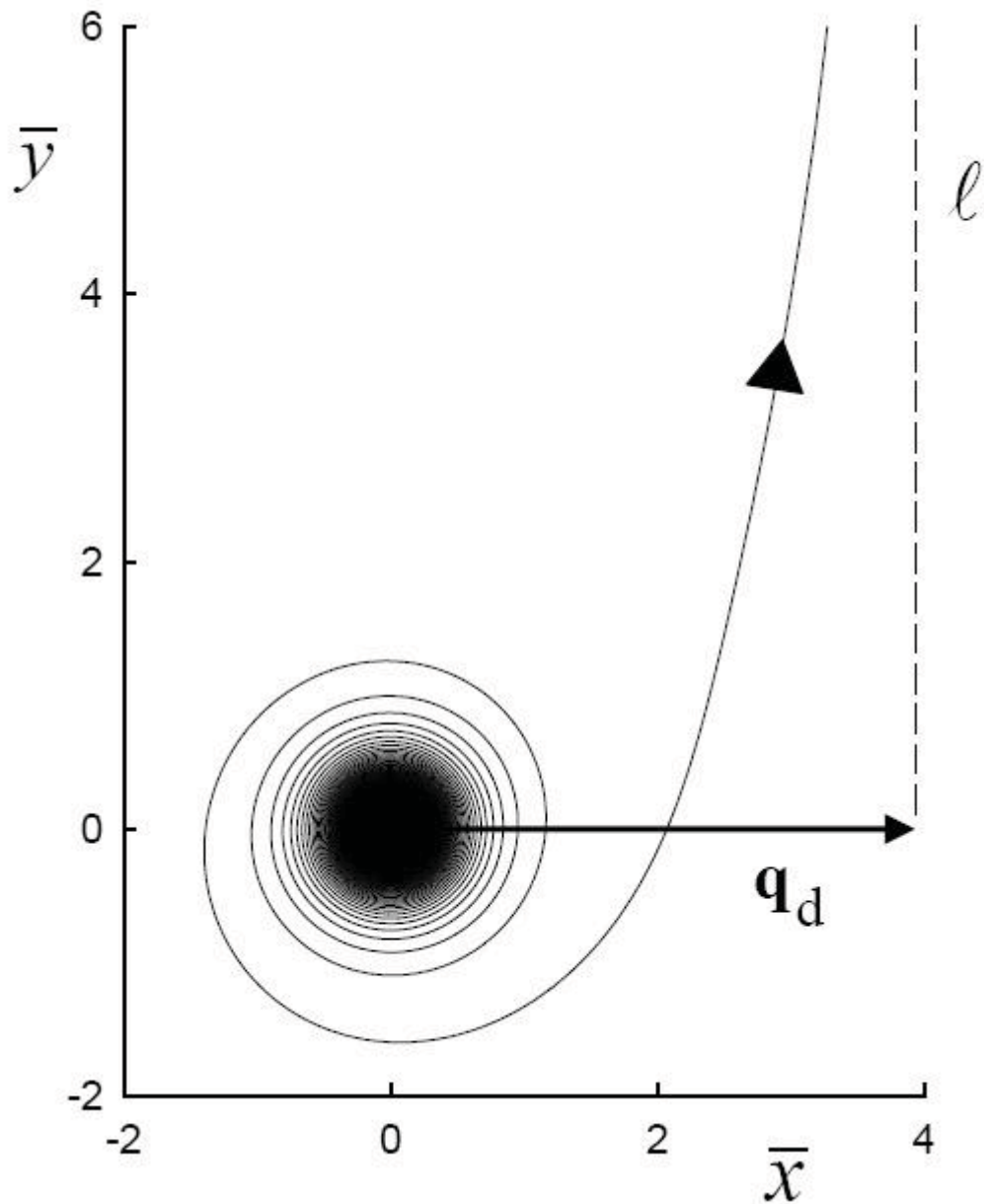


Figure 2.9 A field line in the  $xy$ -plane for an elliptical dipole with  $\beta = 0.5$ .

The parameter  $\phi_0$  is taken as  $\pi/2$ , so the field line runs parallel to the positive  $y$ -axis in the far field. The displacement vector of the image of the dipole in the  $xy$ -plane is along the positive  $x$ -axis and has a magnitude of  $q_d = 4$ .

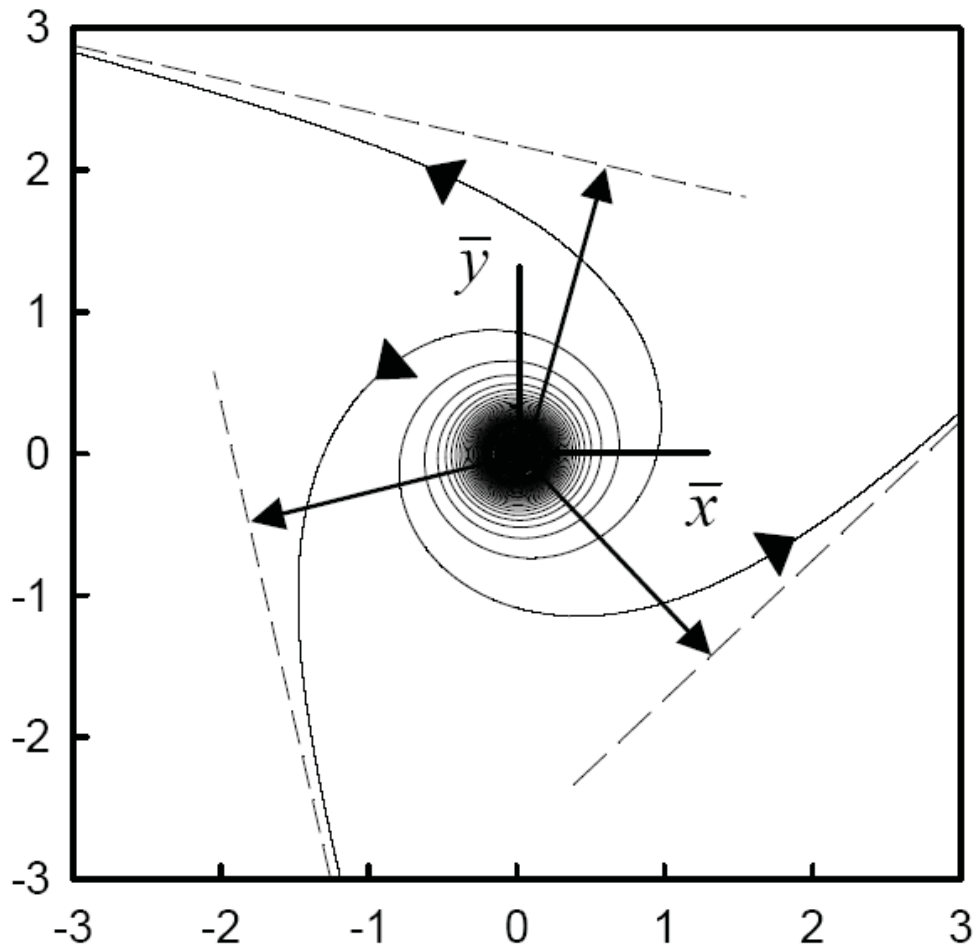


Figure 2.10 Three field lines in the  $xy$ -plane ( $\theta_0 = \pi/2$ ) for a circular dipole ( $\beta = 1$ ).

The field lines approach asymptotically the dashed lines, corresponding to various values of the observation angle  $\phi_0$ . The arrows indicate the displacement vectors of the image of the dipole in the  $xy$ -plane, and they are perpendicular to the dashed lines.

observation angle  $\phi_0$ . From Eqs. (2.65) and (2.66) it then follows that the displacement of this intersection point with respect to the local origin of coordinates is also given by  $\mathbf{q}_d$ , since vector  $\mathbf{q}_d$  is a vector in the observation plane. Therefore, the apparent

displacement of the field line in the far field is the same as the virtual displacement of the source in the  $xy$ -plane.

The displacement in the far field depends on the observation direction  $(\theta_o, \phi_o)$ , and on the parameter  $\beta$  of the ellipse. For  $\beta > 0$ , the displacement is in the  $-\mathbf{e}_{\phi_o}$  direction, as in Fig. 2.12, and for  $\beta < 0$  the displacement is in the  $\mathbf{e}_{\phi_o}$  direction. The magnitude of the displacement is

$$q_d = \frac{2|\beta| \sin \theta_o}{\beta^2 + 1 \zeta(\theta_o, \phi_o)} \quad , \quad (2.67)$$

with  $\zeta(\theta_o, \phi_o)$  given by Eq. (2.34). For  $\theta_o = 0$  or  $\theta_o = \pi$  we have  $\zeta(\theta_o, \phi_o) = 1$  and  $q_d = 0$ . When a field line is observed along the  $z$ -axis, the displacement is zero. We see from Fig. 2.3 that in the  $z$ -direction a field line swirls around the  $z$ -axis and stays close to the  $z$ -axis, which results in a vanishing displacement in the far field. For a given  $\beta$  and  $\phi_o$  we find from Eqs. (2.67) and (2.34) that  $q_d$  is maximum for  $\theta_o = \pi/2$ , so for an observation direction in the  $xy$ -plane. When considering the dependence on  $\phi_o$ , we find from Eq. (2.34) that  $q_d$  is maximum for  $\cos(2\phi_o) = 1$  when  $|\beta| > 1$ , and for  $\cos(2\phi_o) = -1$  when  $|\beta| < 1$ . This corresponds to  $\phi_o = 0$  or  $\pi$  and  $\phi_o = \pm \pi/2$ , respectively. From Fig. 2.1 we then see that both cases correspond to an observation direction along the major axis of the ellipse. When viewed in this direction, the magnitude of the displacement is given by

$$q_d = \begin{cases} 2|\beta| & , \quad |\beta| > 1 \\ \frac{2}{|\beta|} & , \quad |\beta| < 1 \end{cases} \quad , \quad (2.68)$$

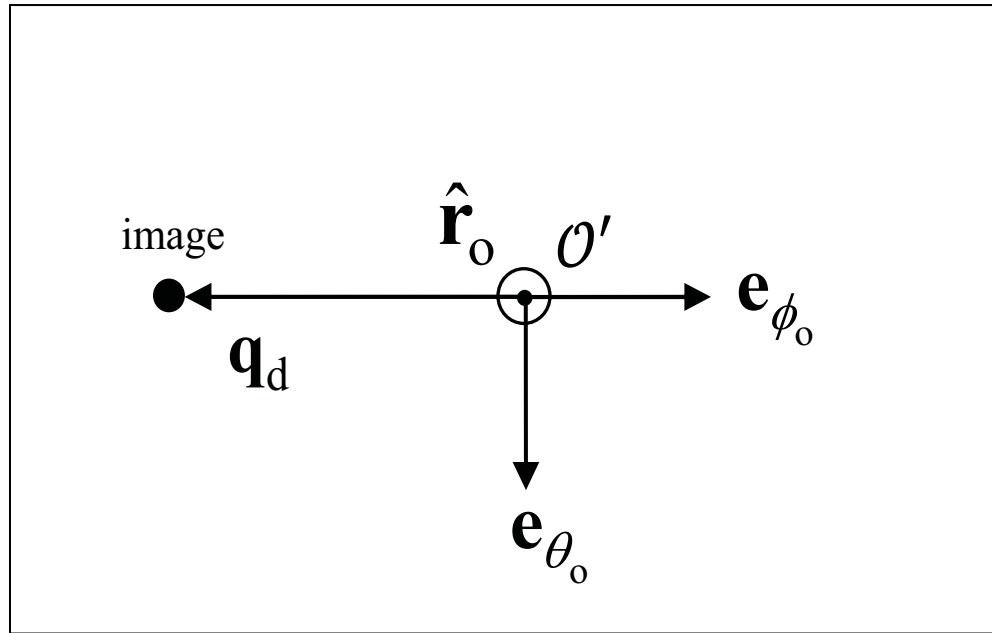


Figure 2.11 The observation plane for an observer located in the direction  $\hat{r}_o$  with respect to the source.

The plane is perpendicular to  $\hat{r}_o$  and far away from the source. If a field line would be a straight line (ray) from the source to the far field, it would intersect the observation plane at the origin  $O'$ . Due to the rotation of the field line near the source, the intersection point, which is the location of the image, is displaced over vector  $q_d$  in the observation plane. For a positive  $\beta$  the rotation near the source is in the positive direction with respect to the  $z$ -axis, and this leads to a displacement in the  $-\mathbf{e}_{\phi_o}$  direction, as shown.

which is the maximum value of  $q_d$ , given  $\beta$ . For a circular dipole we have  $|\beta|=1$ , and the maximum dimensionless displacement is  $q_d=2$ , corresponding to a distance  $r_d = \lambda/\pi$ , with  $\lambda$  the wavelength of the radiation. When the eccentricity of the ellipse increases, the value of  $q_d$  along the major axis increases. Figure 2.12 shows field lines

for observation along the major axis for  $\beta=1$  and  $\beta=0.5$ . For  $|\beta|\neq 1$ , the displacement can be very large, and we see from the figure that the approach to the asymptote  $\ell$  becomes very slow.

For  $\beta \rightarrow \infty$  ( $\beta \rightarrow 0$ ), the oscillation of the dipole becomes linear along the  $x$ -axis ( $y$ -axis), and from Eq. (2.68) it follows that in this limit the maximum displacement grows without bounds. This is due to the fact that along the major axis we have  $\zeta(\theta_0, \phi_0) \rightarrow 0$  for both  $\beta \rightarrow \infty$  and  $\beta \rightarrow 0$ , resulting in a division by a small number in Eq. (2.67). On the other hand, it follows from Eq. (2.20) that  $\zeta(\theta, \phi)$  is proportional to the radiated power per unit solid angle in the direction  $(\theta, \phi)$ . We conclude that in the limit of a linear dipole the displacement is maximum for the direction into which the emitted power vanishes.

In its most general state of oscillation, an electric dipole moment of a source of radiation traces out an ellipse in a plane, taken to be the  $xy$ -plane. The field lines of the Poynting vector of the emitted electromagnetic field represent the direction of energy flow, and we have obtained an analytical solution for these field lines. It was found that for a given observation direction  $(\theta_0, \phi_0)$  in the far field, the corresponding field line lies entirely on the cone specified by the polar angle  $\theta_0$ . Near the location of the dipole the field lines have a vortex structure, in which each field line swirls around the  $z$ -axis numerous times. In the far field, each field line approaches asymptotically a straight line, resembling an optical ray. The parameter equation of this line is given by Eq. (2.65)

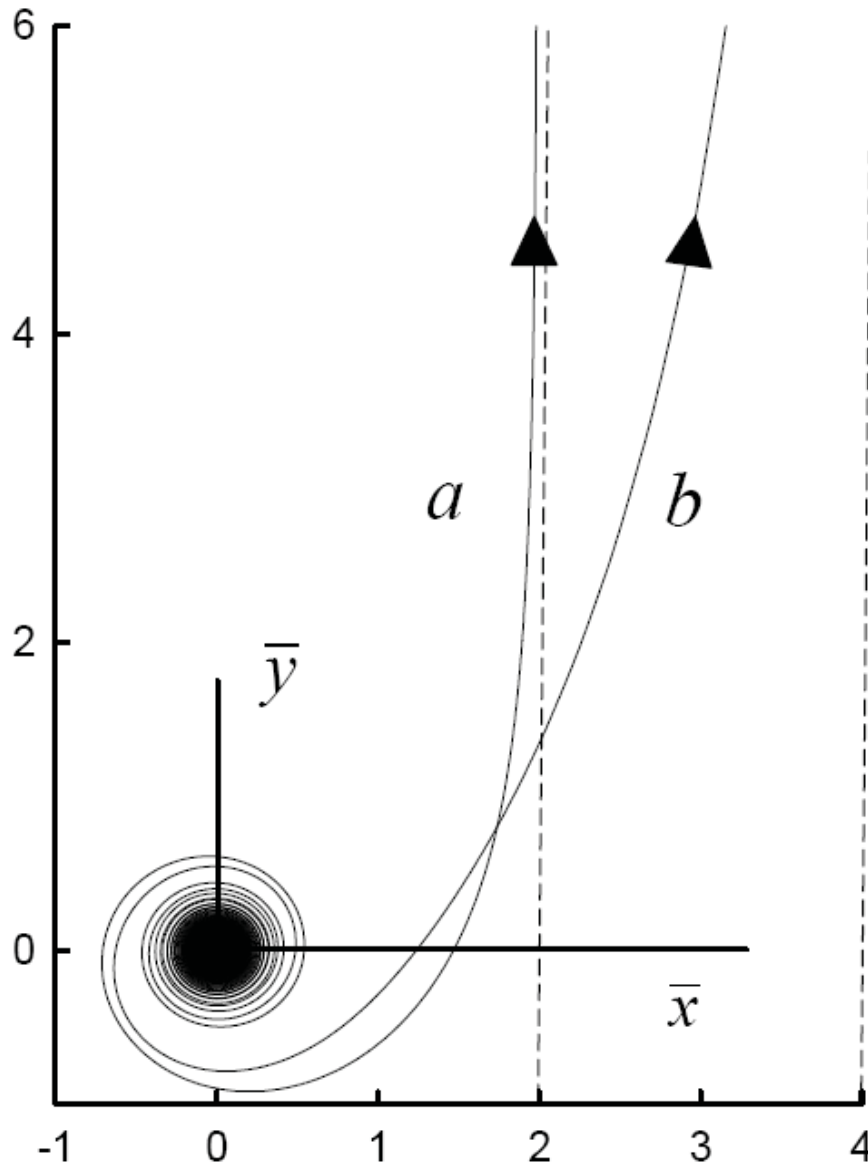


Figure 2.12 Field lines for  $\theta_0 = \pi/2$  and  $\phi_0 = \pi/2$ .

Curves  $a$  and  $b$  correspond to  $\beta=1$  and  $\beta=0.5$ , respectively, and the dashed lines are the asymptotes. The displacement vectors are along the  $x$ -axis, and their magnitudes are  $q_d = 2$  and  $q_d = 4$ , respectively.

for a given observation direction  $(\theta_0, \phi_0)$ . This line does not go through the origin of coordinates, where the dipole is located, and therefore it appears that the position of the dipole in the  $xy$ -plane is shifted. This apparent displacement of the source is represented by the position vector  $\mathbf{q}_d$ , given by Eq. (2.64). The magnitude of vector  $\mathbf{q}_d$  is of the same order as the spatial extent of the vortex near the source, which is of sub-wavelength dimension. However, when the radiation is observed along the major axis of the ellipse, the magnitude of the displacement increases with increasing eccentricity of the ellipse. When a field line is viewed from a location in the far field, the image point is displaced by the same vector  $\mathbf{q}_d$ , with respect to the origin of coordinates in the observation plane. In this fashion, the nanoscale structure of the radiation pattern near the source is reflected in a measurable, although small, effect in the far field.

CHAPTER III  
SUBWAVELENGTH RESOLUTION IN THE FAR FIELD INTENSITY  
PROFILE OF OPTICAL DIPOLE RADIATION

Figure 2.7 shows a field line of the Poynting vector for the radiation emitted by a dipole, with a dipole moment which rotates counterclockwise in the  $xy$ -plane. The scale in the figure is such that one wavelength corresponds to  $2\pi$ . Near the dipole, the field line swirls around the  $z$ -axis, and in the far field it approaches the straight line  $\ell$ . Therefore, it appears as if the radiation comes from a point in the  $xy$ -plane (the plane of dipole rotation) which does not coincide with the location of the source. The spatial extent of the vortex in Fig. 2.7 is less than or about a wavelength, depending on the direction of observation and the state of oscillation of the dipole. The vortex structure of the field line of  $\mathbf{S}(\mathbf{r})$  near the source has an effect in the far field, and it can be anticipated that the displacement shown for a single field line in Fig. 2.7 should lead to an observable shift of the intensity distribution of the radiation at a large distance.

### 3.1 Intensity in the Image Plane

In Eq. (2.18), vector  $\boldsymbol{\varepsilon}$  represents the state of oscillation of the dipole. When  $\boldsymbol{\varepsilon}$  is real, we have  $\mathbf{d}(t) = d_0 \boldsymbol{\varepsilon} \cos(\omega t)$ , and therefore the dipole moment oscillates back and



forth along vector  $\boldsymbol{\varepsilon}$  (linear dipole). For a linear dipole, the Poynting vector is given by Eq. (2.21), which indicates that at any field point  $\mathbf{r}$  the Poynting vector is in the  $\hat{\mathbf{r}}$  direction, and consequently the field lines of the vector field  $\mathbf{S}(\mathbf{r})$  are straight lines in the radial direction. For an observation direction along the dipole axis, e.g.,  $\hat{\mathbf{r}} = \pm\boldsymbol{\varepsilon}$ , we have  $\mathbf{S}(\mathbf{r}) = 0$ , which expresses the fact that no energy is emitted along the dipole axis. This makes the dipole axis a singular line of the field line pattern.

When we have  $\boldsymbol{\varepsilon} = -(\mathbf{e}_x + i\mathbf{e}_y)/\sqrt{2}$ , the dipole moment vector  $\mathbf{d}(t)$  has a constant magnitude and rotates with angular frequency  $\omega$  in the  $xy$ -plane, and in the counterclockwise direction when viewed down the positive  $z$ -axis. Such electric dipole radiation is emitted by an atom in a  $\Delta m = -1$  electronic transition. The rotation of the dipole moment gives a swirling of the field lines of  $\mathbf{S}(\mathbf{r})$  around the  $z$ -axis in the neighborhood of the dipole, as illustrated in Fig. 2.7. In Eq. (2.18), this rotation comes from the term with  $\text{Im}[(\hat{\mathbf{r}} \cdot \boldsymbol{\varepsilon)\boldsymbol{\varepsilon}^*]$ . Since the term is proportional to  $1/q$ , it vanishes in the far field, and only the contribution proportional to  $\hat{\mathbf{r}}$  in  $\mathbf{S}(\mathbf{r})$  survives. Therefore, it may seem that since in the far field we have  $\mathbf{S}(\mathbf{r}) \propto \hat{\mathbf{r}}$ , the field lines of  $\mathbf{S}(\mathbf{r})$  should run in the radial direction. However, near the dipole a field line spirals around the  $z$ -axis, so when such a field line approaches a straight line in the far field, it is offset as compared to a field line which would emanate from the site of the dipole. This gives a displacement of the field lines in the far field, and hence a possible shift in the intensity distribution in the far field.

### 3.1.1 Angular Distribution of the Emitted Power

The power flowing through a surface element  $dA$ , located at point  $\mathbf{r}$ , into the direction of the unit normal  $\hat{\mathbf{n}}$  on  $dA$ , is equal to  $dP = \mathbf{S}(\mathbf{r}) \cdot \hat{\mathbf{n}} dA$ . We now consider  $dA$  as part of a sphere with radius  $r_0$ , and with the origin of coordinates as its center. Then the unit normal  $\hat{\mathbf{n}}$  is equal to  $\hat{\mathbf{r}}$  at any point, and we have  $dA = r_0^2 d\Omega$ , with  $d\Omega$  the solid angle corresponding to the surface element  $dA$ . The emitted power per unit solid angle is given by Eq. (2.13):

$$\frac{dP}{d\Omega} = \frac{3P_0}{8\pi} [1 - (\hat{\mathbf{r}} \cdot \boldsymbol{\varepsilon})(\hat{\mathbf{r}} \cdot \boldsymbol{\varepsilon}^*)] . \quad (3.1)$$

Vector  $\hat{\mathbf{r}}$  has the significance of the observation direction, and in terms of angles  $\theta$  and  $\phi$  of a spherical coordinate system this vector is

$$\hat{\mathbf{r}} = (\mathbf{e}_x \cos \phi + \mathbf{e}_y \sin \phi) \sin \theta + \mathbf{e}_z \cos \theta . \quad (3.2)$$

Therefore,  $dP/d\Omega$  in Eq. (3.1) gives the radiation pattern as a function of  $\theta$  and  $\phi$ , given a particular value of vector  $\boldsymbol{\varepsilon}$ . When integrated over a  $4\pi$  solid angle, the total emitted power is  $P_0$ .

The right-hand side of Eq. (3.1) is independent of the radius  $r_0$  of the sphere, and this may suggest that power simply flows radially outward, as for the case of a linear dipole, and as in the geometrical optics limit of light propagation. We see from Fig. 2.7 that the field lines of the Poynting vector wind around the  $z$ -axis near the dipole, and the power flows out of the dipole along such field lines. The outward power flow  $dP/d\Omega$  for a

given observation direction  $(\theta, \phi)$  shows no sign of this rotation of the field lines in the near field for any  $r_0$ . The term with  $\text{Im}[(\hat{\mathbf{r}} \cdot \boldsymbol{\varepsilon})\boldsymbol{\varepsilon}^*]$  in Eq. (2.18) is responsible for the rotation of the field lines. With Eq. (2.12) we see that the contribution of this term becomes proportional to  $\text{Im}[(\hat{\mathbf{r}} \cdot \boldsymbol{\varepsilon})(\hat{\mathbf{r}} \cdot \boldsymbol{\varepsilon}^*)]$ , and this is zero.

### 3.1.2 Intensity Distribution of the Radiation on a Plane

The angular distribution of the emitted power does not reveal the possible circulation of the field lines in the near field, no matter the radius  $r_0$  of the sphere. Figure 3.1 shows several field lines of the Poynting vector for a dipole rotating in the  $xy$ -plane, and we clearly notice an asymmetry in the field line distribution, for instance along the line  $\bar{y} = 4$  (in dimensionless units, as in Fig. 2.7), which is due to the spiraling behavior of the field lines. In order to possibly observe the rotation of the field lines, we consider the intensity distribution of the radiation over an image plane, rather than over a sphere. We take the image plane as a tangent plane of a sphere with radius  $r_0$ , and the intersection point will be represented by vector  $\mathbf{r}_0$ . Therefore, the position of the plane is determined by angles  $(\theta_0, \phi_0)$ , and by its perpendicular distance  $r_0$  to the origin. The unit vectors  $\mathbf{e}_{\theta_0}$  and  $\mathbf{e}_{\phi_0}$  lie in the image plane, as shown in Fig. 3.2, and they define a rectangular coordinate system  $(\lambda, \mu)$  in which the coordinate axes are along the unit vectors. A point  $\mathbf{r}$  in the image plane can then be represented as

$$\mathbf{r} = \mathbf{r}_0 + \lambda \mathbf{e}_{\theta_0} + \mu \mathbf{e}_{\phi_0} . \quad (3.3)$$

The unit normal vector on the image plane is  $\hat{\mathbf{r}}_0$  for every point in the plane. The intensity  $I$  (power per unit area) at point  $\mathbf{r}$  in the plane depends on the location of the plane, specified by  $\mathbf{r}_0$ , and on the coordinates  $(\lambda, \mu)$  of the point with respect to the origin of the plane at  $\mathbf{r}_0$ . The intensity distribution over the plane is therefore

$$I(\mathbf{r}_0; \lambda, \mu) = \mathbf{S}(\mathbf{r}) \cdot \hat{\mathbf{r}}_0 \quad , \quad (3.4)$$

with  $\mathbf{S}(\mathbf{r})$  given by Eq. (2.18). We introduce dimensionless coordinates  $\bar{\lambda} = k_0 \lambda$ ,  $\bar{\mu} = k_0 \mu$  in the image plane. Since  $k_0$  is the wave number, a dimensionless distance of  $2\pi$  represents one wavelength. Similarly,  $q_0 = k_0 r_0$  is the dimensionless distance between the dipole and the image plane, and for point  $\mathbf{r}$  in the plane we have

$$q = \sqrt{q_0^2 + \bar{\lambda}^2 + \bar{\mu}^2} \quad , \quad (3.5)$$

as the dimensionless distance between this point and the position of the dipole. From Eq. (3.3) we obtain

$$\hat{\mathbf{r}} = \frac{1}{q} (q_0 \hat{\mathbf{r}}_0 + \bar{\lambda} \mathbf{e}_{\theta_0} + \bar{\mu} \mathbf{e}_{\phi_0}) \quad , \quad (3.6)$$

and therefore we have  $\hat{\mathbf{r}} \cdot \hat{\mathbf{r}}_0 = q_0 / q$ . The intensity distribution then becomes

$$I(\mathbf{r}_0; \lambda, \mu) = I_0 \left( \frac{q_0}{q} \right)^3 \left\{ 1 - (\hat{\mathbf{r}} \cdot \boldsymbol{\varepsilon})(\hat{\mathbf{r}} \cdot \boldsymbol{\varepsilon}^*) - \frac{2}{q_0} \left( 1 + \frac{1}{q^2} \right) \text{Im}[(\hat{\mathbf{r}} \cdot \boldsymbol{\varepsilon})(\hat{\mathbf{r}}_0 \cdot \boldsymbol{\varepsilon}^*)] \right\} \quad , \quad (3.7)$$

with

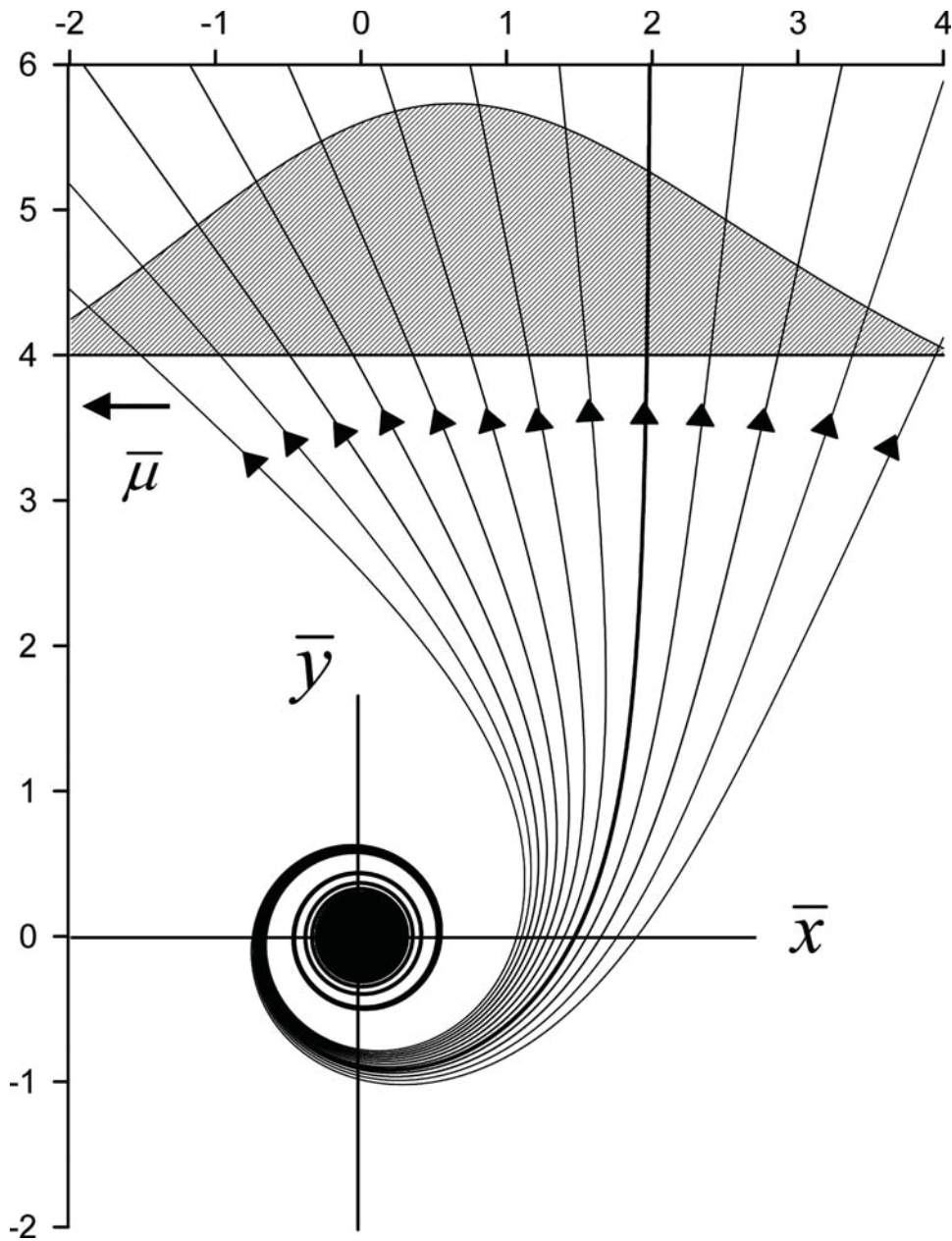


Figure 3.1 Several field lines in the  $xy$ -plane of the Poynting vector for the case of a counterclockwise rotating circular dipole in the  $xy$ -plane.

A bundle of field lines, like in the figure, determines the intensity distribution on an image plane (the line  $\bar{y} = 4$  in the figure). The bold field line is approximately perpendicular to the image plane, and runs asymptotically into the observation direction  $(\theta_0, \phi_0)$ , which is  $(\pi/2, \pi/2)$  in this illustration.

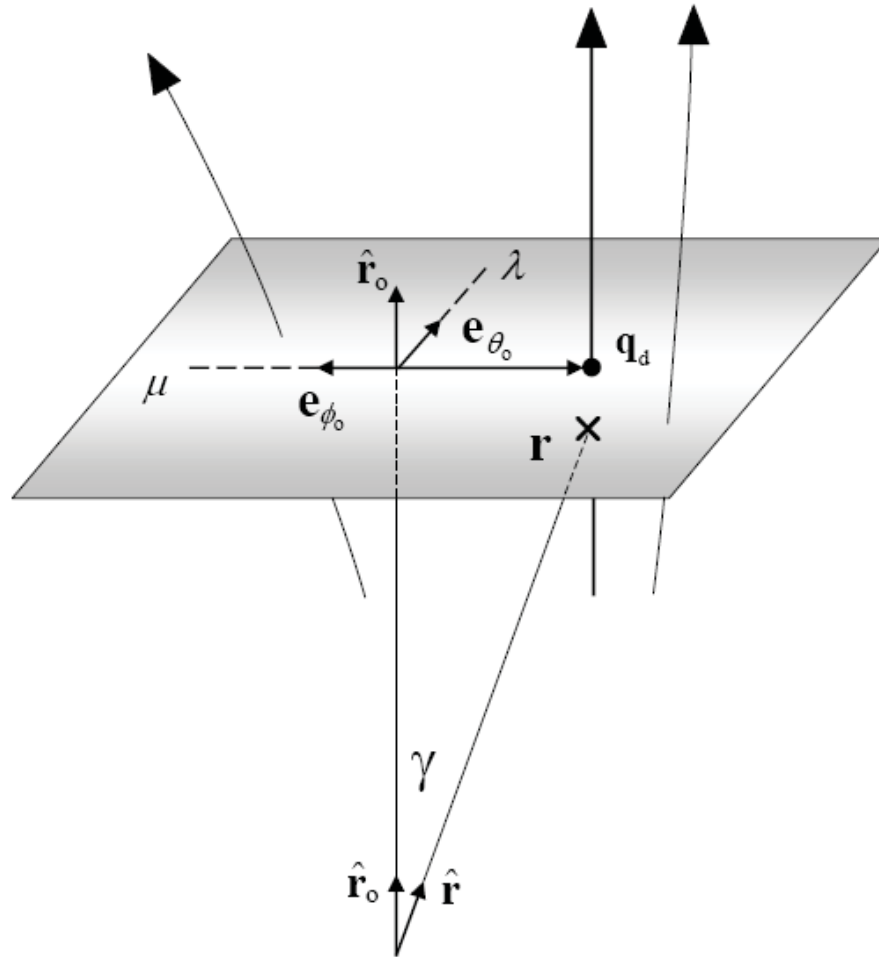


Figure 3.2 The image plane.

The image plane is spanned by the unit vectors  $\mathbf{e}_{\theta_0}$  and  $\mathbf{e}_{\phi_0}$ , and  $\lambda$  and  $\mu$  are the corresponding Cartesian coordinates in the plane. Field lines of the Poynting vector that cross this plane determine the intensity profile, formed on the plane. The bold field line runs asymptotically in the  $\hat{\mathbf{r}}_0$  direction, and crosses the plane at the location given by the displacement vector  $\mathbf{q}_d$  with respect to the origin of the plane. This is the same  $\mathbf{q}_d$  as in Fig. 3.1. Angle  $\gamma$  is the angle between the observation direction  $(\theta_0, \phi_0)$ , represented by  $\hat{\mathbf{r}}_0$ , and the angular location of the field point  $\mathbf{r}$  in the observation plane, as seen from the site of the source.

$$I_o = \frac{3P_o}{8\pi r_o^2} . \quad (3.8)$$

In Eq. (3.7),  $\hat{\mathbf{r}}$  is given by Eq. (3.6) and  $\hat{\mathbf{r}}_o$  follows from Eq. (3.2) with  $(\theta, \phi)$  replaced by  $(\theta_o, \phi_o)$ .

The contribution  $1 - (\hat{\mathbf{r}} \cdot \boldsymbol{\varepsilon})(\hat{\mathbf{r}} \cdot \boldsymbol{\varepsilon}^*)$  in Eq. (3.7) is essentially  $dP/d\Omega$ , as can be seen from Eq. (3.1), and this part corresponds to the energy flow in the radial direction. The term in braces containing  $\text{Im}[(\hat{\mathbf{r}} \cdot \boldsymbol{\varepsilon})(\hat{\mathbf{r}}_o \cdot \boldsymbol{\varepsilon}^*)]$  arises due to the rotation of the field lines. The overall factor  $(q_o/q)^3$  has two contributions: A factor  $(q_o/q)^2$  comes from  $\mathbf{S}(\mathbf{r})$ , Eq. (2.18), being proportional to  $1/r^2$ , and a factor  $q_o/q$  results from  $\hat{\mathbf{r}} \cdot \hat{\mathbf{r}}_o = q_o/q$ , e.g., from projecting the radial outflow onto a plane rather than a sphere. In other words, the factor  $q_o/q$  accounts for the fact that the field lines are not perpendicular to the observation plane, as can be seen in Fig. 3.1.

An intensity distribution  $I_o(q_o/q)^3$  in the image plane would be a single peak at the origin, and rotational symmetric around the normal vector  $\hat{\mathbf{r}}_o$ . If we set  $q_o/q = \cos \gamma$ , then  $\gamma$  (see Fig. 3.2) is the angle between vector  $\mathbf{r}$  and vector  $\mathbf{r}_o$ , as seen from the location of the dipole. The angular half-width at half-maximum of the image on the plane, as viewed from the site of the dipole, then follows from  $(q_o/q)^3 = 1/2$ , and this is  $\gamma = 37^\circ$ . This peak will be altered due to the angular dependence of the emitted power in the radial direction and due to possible rotations of the field lines.

As an example, let us consider a linear dipole along the  $y$ -axis, so  $\boldsymbol{\varepsilon} = \mathbf{e}_y$ . Since  $\boldsymbol{\varepsilon}$  is real, the field lines of the Poynting vector are in the radial direction, without any curving.

We take the image plane perpendicular to the  $y$ -axis, and therefore  $\boldsymbol{\varepsilon}$  coincides with the observation direction  $\hat{\mathbf{r}}_0$ . Equation (3.7) can then be simplified to

$$I(\mathbf{r}_0; \lambda, \mu) = I_0 \cos^3 \gamma \sin^2 \gamma, \quad (3.9)$$

where  $\gamma$  is the angular location of a point on the image plane, as illustrated in Fig. 3.2. The intensity in the observation direction ( $\gamma = 0$ ) is zero, and therefore the intensity has a minimum at the origin of the image plane. The intensity is rotationally symmetric around  $\hat{\mathbf{r}}_0$ , and consequently the maximum of the distribution has the shape of a ring. Figure 3.3 shows the intensity distribution for this case. The angular width of the ring is given by  $\cos \gamma = \sqrt{3/5}$ , which gives  $\gamma = 39^\circ$ , and the radius of the ring in the image plane is  $q_0 \sqrt{2/3}$ .

### 3.2 Extremum in the Far Field Intensity Profile of a Circular Dipole

Features of the intensity distribution like the ring in Fig. 3.3 are of macroscopic nature in the sense that they scale with the distance  $q_0$  between the dipole and the image plane. The structure of the intensity profile is a result of the angular distribution of the emitted power,  $dP/d\Omega$ . On the other hand, the swirling of the field lines, as in Fig. 3.1, can only affect the intensity on a nanoscale, since the spatial dimension of the vortex is of the order of a wavelength of the radiation. We shall next consider the effect of the rotation of the field lines on the intensity distribution in detail.

For an arbitrary complex-valued vector  $\boldsymbol{\varepsilon}$ , the dipole moment  $\mathbf{d}(t)$  in Eq. (2.1) traces out an ellipse in a plane as stated in chapter 2. We take this plane as the  $xy$ -plane and



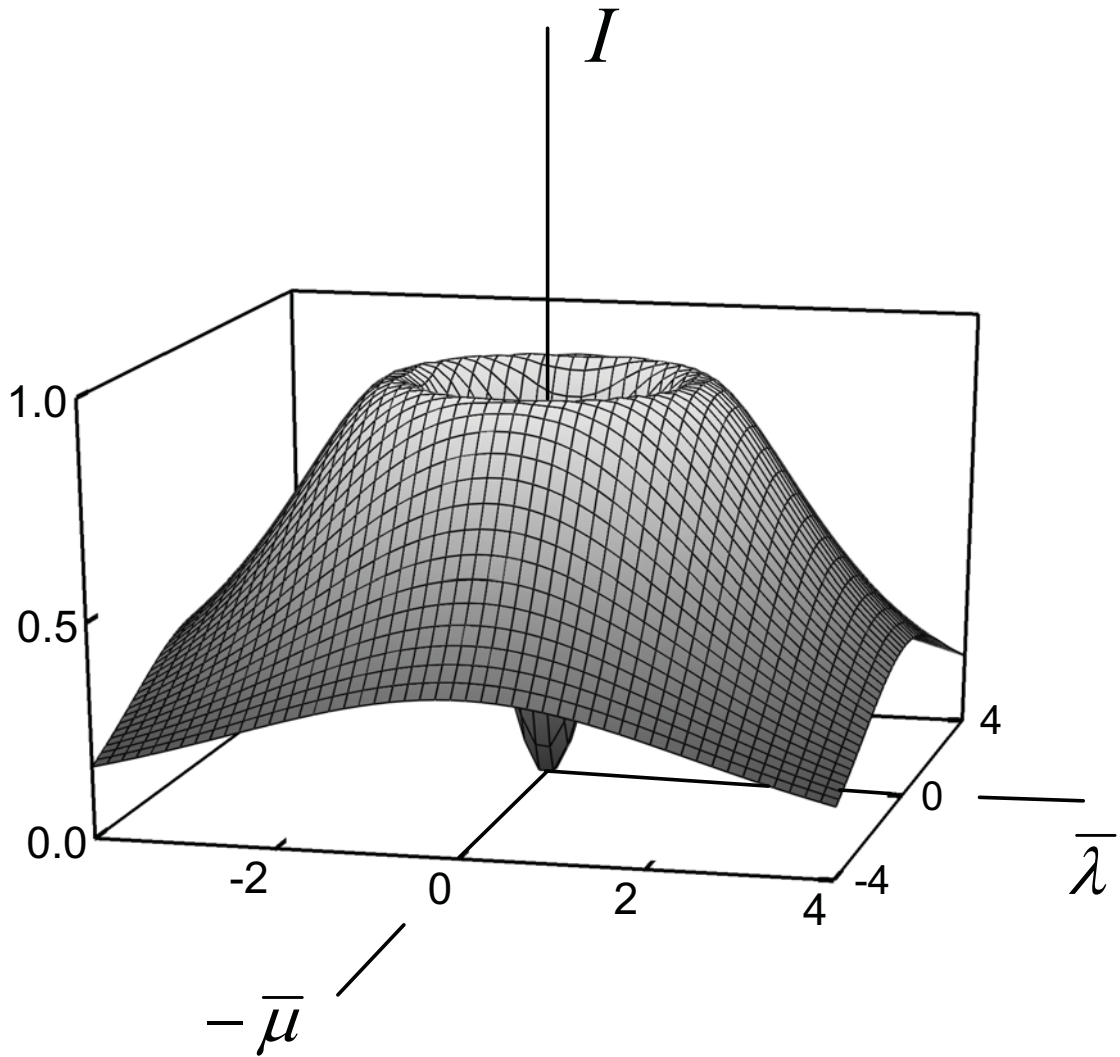


Figure 3.3 The intensity distribution in an image plane perpendicular to the  $y$ -axis.

In this figure, the dipole moment oscillates linearly along the  $y$ -axis. The dimensionless distance between the plane and the dipole is  $q_0 = 2$ , and the dimensionless radius of the ring is 1.63.

parametrize vector  $\boldsymbol{\varepsilon}$  as Eq. (2.31), represented by parameter  $\beta$ . For  $\beta > 0$  ( $\beta < 0$ ) the dipole moment rotates in the counterclockwise (clockwise) direction, when viewed down the  $z$ -axis, and for  $\beta = \pm 1$  the ellipse reduces to a circle. For  $\beta = 0$  the oscillation becomes linear along the  $y$ -axis. The unit vector  $\hat{\mathbf{r}}$  into the direction of a point on the image plane involves the unit vectors that span the plane, according to Eq. (3.6).

Explicitly we have

$$\mathbf{e}_{\theta_0} = (\mathbf{e}_x \cos \phi_0 + \mathbf{e}_y \sin \phi_0) \cos \theta_0 - \mathbf{e}_z \sin \theta_0, \quad (3.10)$$

$$\mathbf{e}_{\phi_0} = -\mathbf{e}_x \sin \phi_0 + \mathbf{e}_y \cos \phi_0, \quad (3.11)$$

and the intensity becomes

$$I(\mathbf{r}_0; \lambda, \mu) = I_0 \left( \frac{q_0}{q} \right)^3 \left[ 1 - (\hat{\mathbf{r}} \cdot \boldsymbol{\varepsilon})(\hat{\mathbf{r}} \cdot \boldsymbol{\varepsilon}^*) - \frac{1}{q_0 q} \left( 1 + \frac{1}{q^2} \right) \frac{2\beta}{\beta^2 + 1} \bar{\mu} \sin \theta_0 \right]. \quad (3.12)$$

The last term in square brackets comes from the rotation of the field lines. We notice that this term is proportional the coordinate  $\bar{\mu}$  in the image plane, and this indicates that the peak in the intensity distribution will be shifted along the  $\bar{\mu}$ -axis. We also see that for  $\beta > 0$ , as in Fig. 3.1, the shift is in the negative  $\bar{\mu}$  direction, and for  $\beta < 0$  the shift is in the positive direction. For a linear dipole ( $\beta = 0$ ), the shift vanishes, and for an observation direction  $\hat{\mathbf{r}}_0$  perpendicular to the plane of rotation of the dipole ( $\theta_0 = 0$  or  $\pi$ ), the shift is zero for any  $\beta$ . The displacement term has an overall factor of  $1/(q_0 q)$ , which is  $O(1/q_0^2)$  in the far field ( $q_0 \rightarrow \infty$ ), and it may seem that at a large distance from the source, the shift of the peak should disappear. We shall see in the next section that this is not the case.

The first part in square brackets in Eq. (3.12) for  $I(\mathbf{r}_0; \lambda, \mu)$  comes from  $dP/d\Omega$ , and for an elliptic dipole we find explicitly:

$$(\hat{\mathbf{r}} \cdot \boldsymbol{\varepsilon})(\hat{\mathbf{r}} \cdot \boldsymbol{\varepsilon}^*) = \frac{1}{q^2} \frac{1}{\beta^2 + 1} [\beta^2 (\bar{\rho} \cos \phi_0 - \bar{\mu} \sin \phi_0)^2 + (\bar{\rho} \sin \phi_0 + \bar{\mu} \cos \phi_0)^2] . \quad (3.13)$$

Here we have introduced the abbreviation

$$\bar{\rho} = q_0 \sin \theta_0 + \bar{\lambda} \cos \theta_0 . \quad (3.14)$$

When the dipole moment rotates in a circle, we have  $\beta = \pm 1$ , and the expression for the intensity distribution on a plane simplifies considerably. From Eqs. (3.12) and (3.13) we obtain

$$I(\mathbf{r}_0; \lambda, \mu) = I_0 \left( \frac{q_0}{q} \right)^3 \left[ 1 - \frac{1}{2q^2} (\bar{\rho}^2 + \bar{\mu}^2) - \frac{\beta}{q_0 q} \left( 1 + \frac{1}{q^2} \right) \bar{\mu} \sin \theta_0 \right] . \quad (3.15)$$

The dependence on the observation direction  $\phi_0$  has disappeared, as could be expected for a circular dipole. The last term in square brackets comes from the curving of the field lines near the dipole, as in Fig. 3.1, and this term is proportional to  $\bar{\mu}$ . The displacement  $\mathbf{q}_d$  of the field lines in the far field is in the  $\bar{\mu}$  direction, and we expect a corresponding shift of the intensity distribution in the image plane. When considering the  $\bar{\mu}$  dependence of  $I(\mathbf{r}_0; \lambda, \mu)$  for fixed  $\bar{\lambda}$ , the dependence on  $\bar{\mu}$  enters through the parameter  $q$ , Eq. (3.5), and explicitly as  $\bar{\mu}^2$  and  $\bar{\mu}$  in Eq. (3.15). Without the rotation of

the field lines,  $\bar{\mu}$  only enters as  $\bar{\mu}^2$  and since this is symmetric in  $\bar{\mu}$  the profile would be symmetric in the  $\bar{\mu}$  direction around  $\bar{\mu} = 0$  in the image plane. In particular, the point  $\bar{\mu} = 0$  would be either a local maximum or minimum, and hence any shift of this local extremum would be a reflection of the circulation of the field lines in the optical near field.

In order to find the extrema of the intensity distribution, we first consider the dependence of  $I(\mathbf{r}_0; \lambda, \mu)$  on  $\bar{\mu}$ , for a given  $\bar{\lambda}$ . Setting  $\partial I / \partial \bar{\mu} = 0$  yields

$$\bar{\mu} \left[ 4 - \frac{5}{2q^2} (\bar{\mu}^2 + \bar{\rho}^2) \right] = -\beta \frac{\sin \theta_0}{q_0 q} (q_0^2 + \bar{\lambda}^2 - 3\bar{\mu}^2) , \quad (3.16)$$

and here we have also assumed detection in the far field, for which  $q_0 \gg 1$ . For detection along the  $z$ -axis ( $\theta_0 = 0$  or  $\pi$ ) we have  $\sin \theta_0 = 0$ , and a solution is  $\bar{\mu} = 0$ . In order to find the general solution, we recall that an extremum in the far field should scale with  $q_0$ , so that angle  $\gamma$  in Fig. 3.2 remains constant. When we divide Eq. (3.16) by  $q_0$ , then the left-hand side becomes constant for  $q_0$  large, and the right-hand side vanishes as  $O(1/q_0)$ . It can be shown by inspection that the factor in square brackets on the left-hand side is positive, and therefore we find from Eq. (3.16) that  $\bar{\mu}/q_0 = 0$  for any given  $\bar{\lambda}$ . Since there is only one solution, the extremum is a maximum in the  $\bar{\mu}$  direction. Similarly,  $\partial I / \partial \bar{\lambda} = 0$  yields

$$-3\bar{\lambda} + \frac{5\bar{\lambda}}{2q^2} (\bar{\mu}^2 + \bar{\rho}^2) - \bar{\rho} \cos \theta_0 = -\beta \frac{4\bar{\lambda}\bar{\mu}}{q_0 q} \sin \theta_0 , \quad (3.17)$$

for  $q_0 \gg 1$ . For detection along the  $z$ -axis ( $\theta_0 = 0$  or  $\pi$ ) we have  $\bar{\rho} = \bar{\lambda} \cos \theta_0$ , and we see that  $\bar{\lambda} = 0$  is a solution of Eq. (3.17). Also for detection in the  $xy$ -plane, for which  $\theta_0 = \pi/2$ , we find that  $\bar{\lambda} = 0$  is a solution. When we divide Eq. (3.17) by  $q_0$ , then the right-hand side goes to zero, and the remaining equation can be solved for  $\bar{\lambda}/q_0$  for any given  $\bar{\mu}/q_0$  and  $\theta_0$ . The equation has one solution, and therefore the extremum in the  $\bar{\lambda}$  direction is a maximum.

It follows from the previous paragraph that the intensity distribution has a single peak in the  $\bar{\lambda}\bar{\mu}$ -plane. When we indicate the coordinates of the location of the peak by  $(\bar{\lambda}_p, \bar{\mu}_p)$ , then we have  $\bar{\mu}_p/q_0 = 0$ . With  $\bar{\mu}_p/q_0 = 0$ , Eq. (3.17) becomes an equation for  $\bar{\lambda}_p/q_0$ , after division by  $q_0$ . When we set  $\alpha = \bar{\lambda}_p/q_0$ , Eq. (3.17) yields

$$\frac{5}{2}\alpha(\sin \theta_0 + \alpha \cos \theta_0)^2 = (1 + \alpha^2)[\sin \theta_0 \cos \theta_0 + \alpha(3 + \cos^2 \theta_0)] , \quad (3.18)$$

which is a cubic equation for  $\alpha$ , given the observation angle  $\theta_0$ . The solution of this equation is shown in Fig. 3.4. We see that  $\alpha$  is relatively small for all  $\theta_0$ , so that a reasonable approximation is obtained by setting  $\alpha^3 \approx 0$ ,  $\alpha^2 \approx 0$ . This yields

$$\alpha \approx \frac{\sin(2\theta_0)}{7\sin^2\theta_0 - 8} , \quad (3.19)$$

which is shown as the dashed curve in the figure. The shift of the maximum in the  $\bar{\lambda}$  direction is negative (positive) for  $0 < \theta_0 < \pi/2$  ( $\pi/2 < \theta_0 < \pi$ ).

### 3.2.1 Shift of the Peak in the Far Field for a Circular Dipole

The peak in the intensity distribution is located at  $\bar{\lambda}_p = \alpha q_0$  along the  $\bar{\lambda}$ -axis in the image plane, where  $\alpha$  follows from Fig 3.4, given angle  $\theta_0$ . The location of the peak is a consequence of the angle dependence of  $dP/d\Omega$ , and is independent of the rotation of the field lines near the origin of coordinates. The position scales with the distance  $q_0$  between the image plane and the dipole, such that the viewing angle  $\gamma$  is independent of  $q_0$ . In the  $\bar{\mu}$  direction, the maximum appears at  $\bar{\mu}_p/q_0 = 0$ , and this leaves the possibility that  $\bar{\mu}_p$  is finite, rather than zero. When we set  $\bar{\mu}_p/q_0 = 0$  and  $\bar{\lambda}_p/q_0 = \alpha$  in Eq. (3.16), we obtain an equation for  $\bar{\mu}_p$ . The solution is

$$\bar{\mu}_p = -\beta(1+\alpha^2)^{3/2} \frac{2\sin\theta_0}{8(1+\alpha^2)-5(\sin\theta_0+\alpha\cos\theta_0)^2}, \quad (3.20)$$

which is independent of  $q_0$ , and represents the shift of the maximum in the far field. For a given  $\theta_0$ ,  $\alpha$  follows from Eq. (3.18), and hence the shift of the peak along the  $\bar{\mu}$ -axis is a function of the observation angle  $\theta_0$  only (apart from the overall  $\beta = \pm 1$ ). Figure 3.5 shows the far-field intensity distribution for  $\theta_0 = \pi/2$  with  $\beta = 1$ . The maximum along the  $\bar{\mu}$ -axis is located at  $\bar{\mu}_p = -2/3$ .

The shift of the peak,  $\bar{\mu}_p$ , is zero for  $\theta_0 = 0, \pi$  and maximum for  $\theta_0 = \pi/2$ , and the maximum shift at  $\theta_0 = \pi/2$  is  $|\bar{\mu}_p| = 2/3$ . Figure 3.6 shows the behavior of the shift as a function of  $\theta_0$  for  $\beta = 1$ . The shift is due to the rotation in the field lines of the Poynting vector, and we see from Fig. 3.1 that the shift is expected to be negative for a dipole moment which rotates counterclockwise in the  $xy$ -plane. The right-hand side of

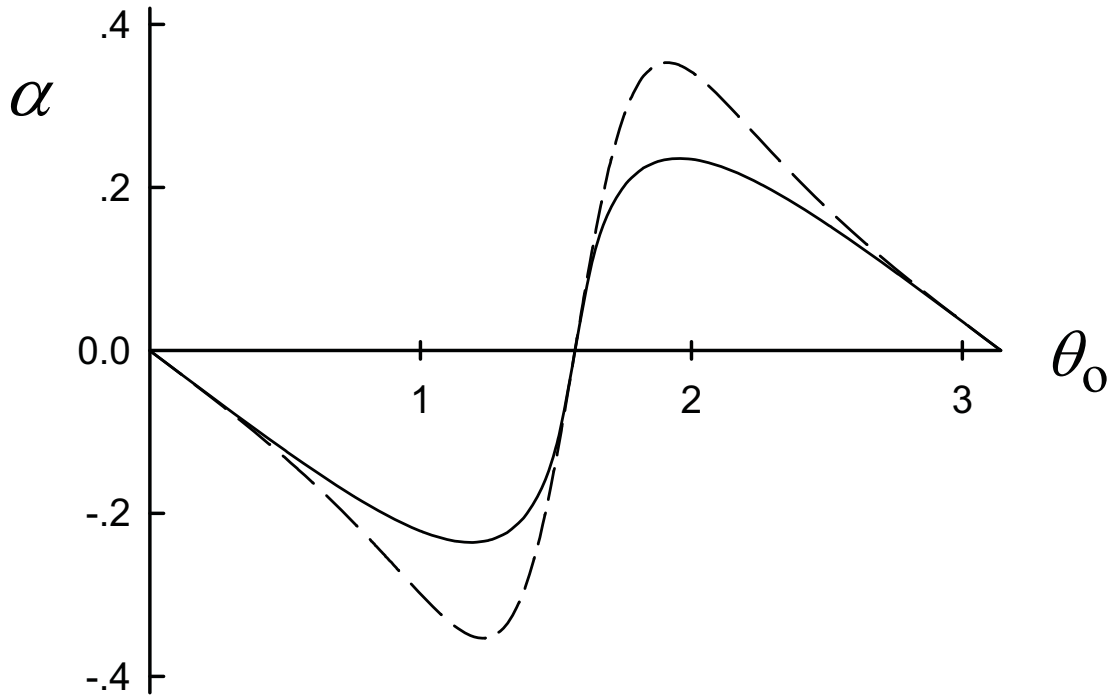


Figure 3.4 Curve  $\alpha$  and its approximation.

The solid curve shows  $\alpha$ , the solution of Eq. (3.18), as a function of  $\theta_0$ , and the dashed curve is the approximation given by Eq. (3.19).

Eq. (3.20) changes sign with  $\beta$ , and therefore for a clockwise rotating dipole moment the shift is positive. When the dipole radiation is emitted by an atom in a laser beam, the rotation direction of the dipole moment can be reversed by changing the helicity of the driving laser from left-circular to right-circular polarized, or vice versa, for instance by inserting a half-wave plate. The peak in the intensity would then shift over  $4/3$  in dimensionless units, and this corresponds to a distance of  $2\lambda/(3\pi)$ , with  $\lambda$  the wavelength of the radiation. Although this shift is of nanoscale size, it should be

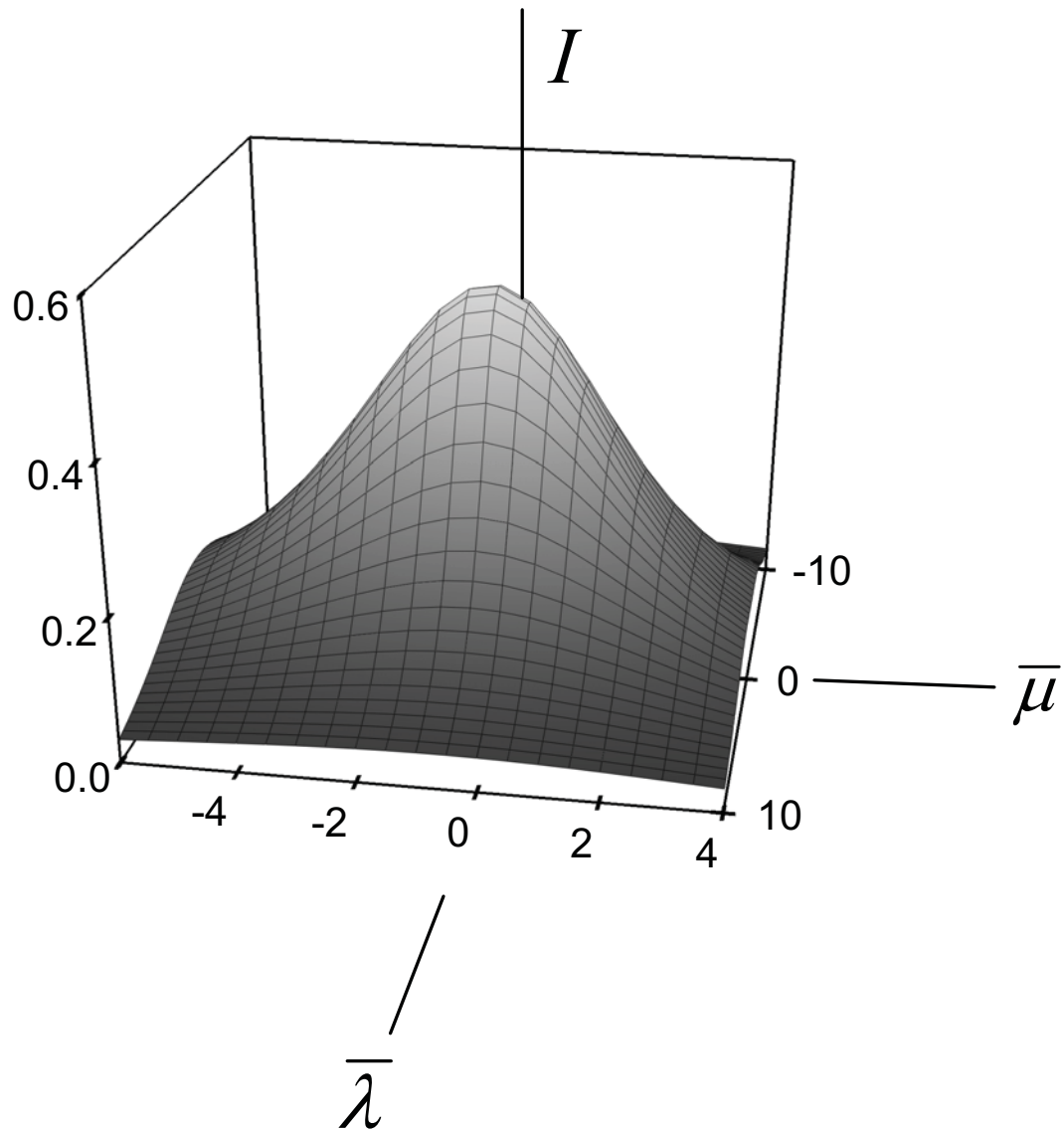


Figure 3.5 The far-field intensity distribution for a rotating dipole.

The graph shows the far-field intensity distribution for a rotating dipole with  $\beta=1$  for observation along the  $xy$ -plane. The maximum is located on the  $\bar{\mu}$ -axis at  $\bar{\mu}_p = -2/3$ .



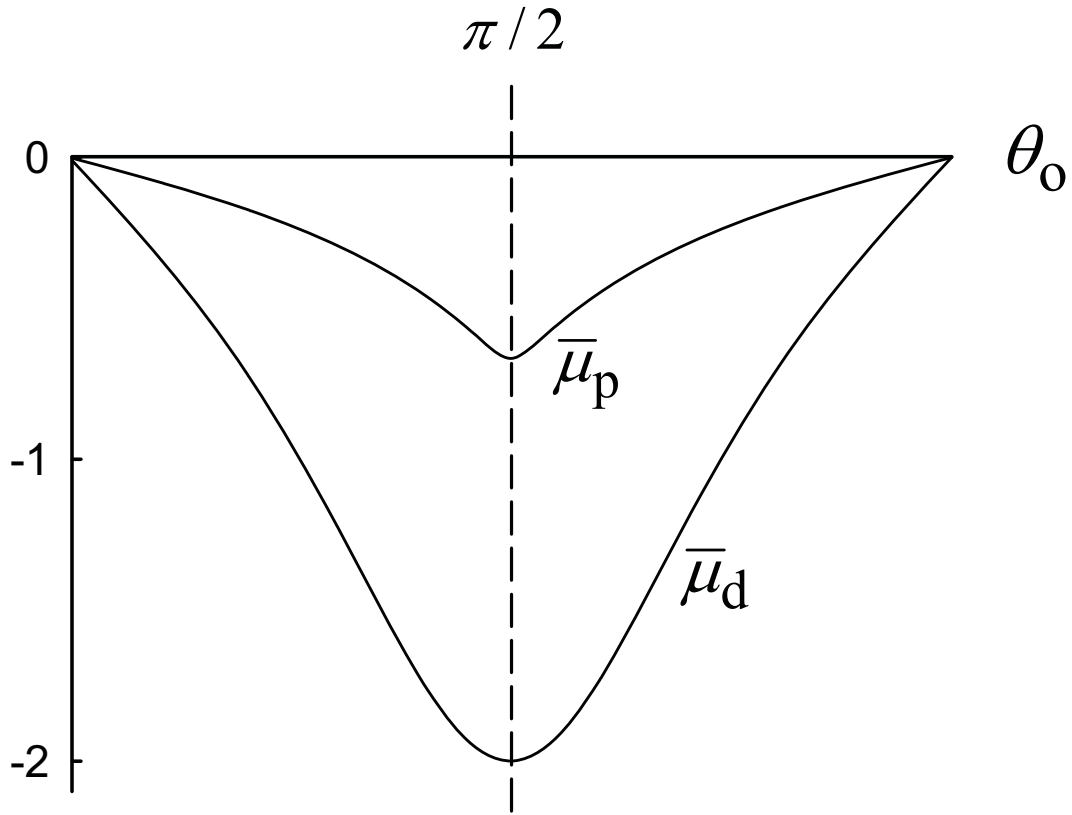


Figure 3.6 The shift  $\bar{\mu}_p$  curve and the displacement  $\bar{\mu}_d$  curve.

The figure shows the shift  $\bar{\mu}_p$  of the peak in the intensity distribution and the displacement  $\bar{\mu}_d$  of the central field line as a function of the observation angle  $\theta_0$ , both for a circular dipole with  $\beta=1$ . For  $\beta=-1$  both functions change sign.

observable in experiment. In this fashion, the swirling of the field lines of the Poynting vector in the near field could be observed by a measurement in the far field.

All field lines of the Poynting vector run radially outward in the far field, but they are displaced with respect to an optical ray which would emanate from the exact site of the dipole, as illustrated in Fig. 2.7. For a given observation direction  $(\theta_0, \phi_0)$ , there is one

field line which runs exactly into that direction, and this field line intersects the observation plane under a right angle (bold field line in Fig. 3.1). The displacement vector of this field line is a vector in the corresponding observation plane, and this vector is along the  $\bar{\mu}$ -axis. If we write  $\mathbf{q}_d = \bar{\mu}_d \mathbf{e}_{\phi_0}$ , then the displacement of this field line is given by Eq. (2.67), and this yields:

$$\bar{\mu}_d = -\beta \frac{2 \sin \theta_0}{2 - \sin^2 \theta_0} . \quad (3.21)$$

Both  $\bar{\mu}_p$  and  $\bar{\mu}_d$  are shown in Fig. 3.6, and we see that the displacement of the field line is larger than the shift of the peak in the corresponding intensity distribution. The intensity profile is determined by a bundle of field lines, as depicted in Fig. 3.1, and the direction of the central field line does not necessarily coincide exactly with the location of an extremum in the intensity pattern.

### 3.3 Far Field Intensity Pattern for an Elliptical Dipole

In the most general state of oscillation of a dipole, the dipole moment vector traces out an ellipse, and the plane of this ellipse is taken as the  $xy$ -plane. The ellipticity is represented by parameter  $\beta$  in Eq. (2.31). For  $\beta = 0$  the dipole moment oscillates linearly along the  $y$ -axis. For  $\beta = \pm 1$  it rotates along a circle, and for  $\beta \rightarrow \pm \infty$  the oscillation becomes linear along the  $x$ -axis. We shall consider an observation plane perpendicular to the  $y$ -axis, so that  $\theta_0 = \phi_0 = \pi/2$ . For this example, the intensity

becomes

$$I(\mathbf{r}_0; \lambda, \mu) = I_0 \left( \frac{q_0}{q} \right)^3 \left\{ 1 - \frac{1}{q^2 (\beta^2 + 1)} \left[ \beta^2 \bar{\mu}^2 + q_0^2 + 2\beta \bar{\mu} \frac{q}{q_0} \left( 1 + \frac{1}{q^2} \right) \right] \right\} . \quad (3.22)$$

For  $\beta = 0$  the profile has a minimum at  $\bar{\lambda} = \bar{\mu} = 0$  and a ring-shaped maximum, as shown in Fig. 3.3. For  $\beta = 0$  we have a linear dipole, and the field lines of the Poynting vector run in the radial direction, without any curving. Therefore, there is no shift  $\bar{\mu}_p$  of the extremum (the hole in this case) in the far field. For  $\beta = \pm 1$ , the extremum is a peak at  $\bar{\lambda} = 0$  and near  $\bar{\mu} = 0$ , as shown in Fig. 3.5 for  $\beta = 1$ . The shift of the peak in the  $\bar{\mu}$ -direction is  $\bar{\mu}_p = -2\beta/3$ .

Possible extrema along the  $\bar{\lambda}$ -axis follow from setting  $\partial I / \partial \bar{\lambda} = 0$ ,  $\bar{\mu} = 0$ , and we also let  $q_0 \gg 1$  for the far field. This yields  $\bar{\lambda} = 0$  and

$$\frac{\bar{\lambda}}{q_0} = \pm \sqrt{\frac{2 - 3\beta^2}{3(\beta^2 + 1)}} , \quad |\beta| < \sqrt{2/3} . \quad (3.23)$$

When  $|\beta| < \sqrt{2/3}$ , we obtain two solutions  $\bar{\lambda} / q_0$ , in addition to the solution  $\bar{\lambda} = 0$ . This corresponds to two maxima and a minimum at  $\bar{\lambda} = 0$ . When  $|\beta| > \sqrt{2/3}$ , we only have  $\bar{\lambda} = 0$ , and therefore this must be a maximum. Similarly, extrema along the  $\bar{\mu}$ -axis follow from setting  $\partial I / \partial \bar{\mu} = 0$  and  $\bar{\lambda} = 0$ . This gives

$$\frac{2\beta}{q_0 q} (q_0^2 - 3\bar{\mu}^2) = -\bar{\mu} \left[ 5\beta^2 + 3 - \frac{5}{q^2} (q_0^2 + \beta^2 \bar{\mu}^2) \right] . \quad (3.24)$$

When dividing by  $q_0$ , the right-hand side vanishes in the far field. We then obtain the solutions  $\bar{\mu}/q_0 = 0$  and

$$\frac{\bar{\mu}}{q_0} = \pm \sqrt{\frac{2-5\beta^2}{3}} \quad , \quad |\beta| < \sqrt{2/5} \quad (3.25)$$

We also find either two maxima and a minimum or one maximum, depending on the value of  $|\beta|$ .

For  $\beta = 0$  we have a minimum in both the  $\bar{\lambda}$ - and  $\bar{\mu}$ -directions at the origin of the image plane, as shown in Fig. 3.3, and the maximum has the shape of a ring. When  $|\beta|$  increases, the locations of the maxima along the coordinate axes change according to Eqs. (3.23) and (3.25). These functions of  $|\beta|$  are shown in Fig. 3.7, and we see that the dimension of the hole decreases both along the  $\bar{\lambda}$ -axis and the  $\bar{\mu}$ -axis. Since the decrease along the  $\bar{\mu}$ -axis is faster than along the  $\bar{\lambda}$ -axis, the ring distorts. The dimension of the hole shrinks in both directions, and the hole becomes shallower. When  $|\beta|$  approaches the value of  $\sqrt{2/5}$ , the maxima along the  $\bar{\mu}$ -axis approach the origin of coordinates, and for  $|\beta| > \sqrt{2/5}$  we only have a maximum at  $\bar{\mu}/q_0 = 0$ . When  $|\beta|$  increases further towards  $|\beta| = \sqrt{2/3}$ , also the maxima along the  $\bar{\lambda}$ -axis approach the origin, and for  $|\beta| > \sqrt{2/3}$  we have a maximum at  $\bar{\lambda} = 0$ . Therefore, for  $0 \leq |\beta| < \sqrt{2/5}$  the intensity profile has a hole near the origin. For  $\sqrt{2/5} < |\beta| < \sqrt{2/3}$  the region around the origin has the appearance of a saddle point, and for  $|\beta| > \sqrt{2/3}$  we have a single peak, as for  $\beta = 1$  in Fig. 3.5.

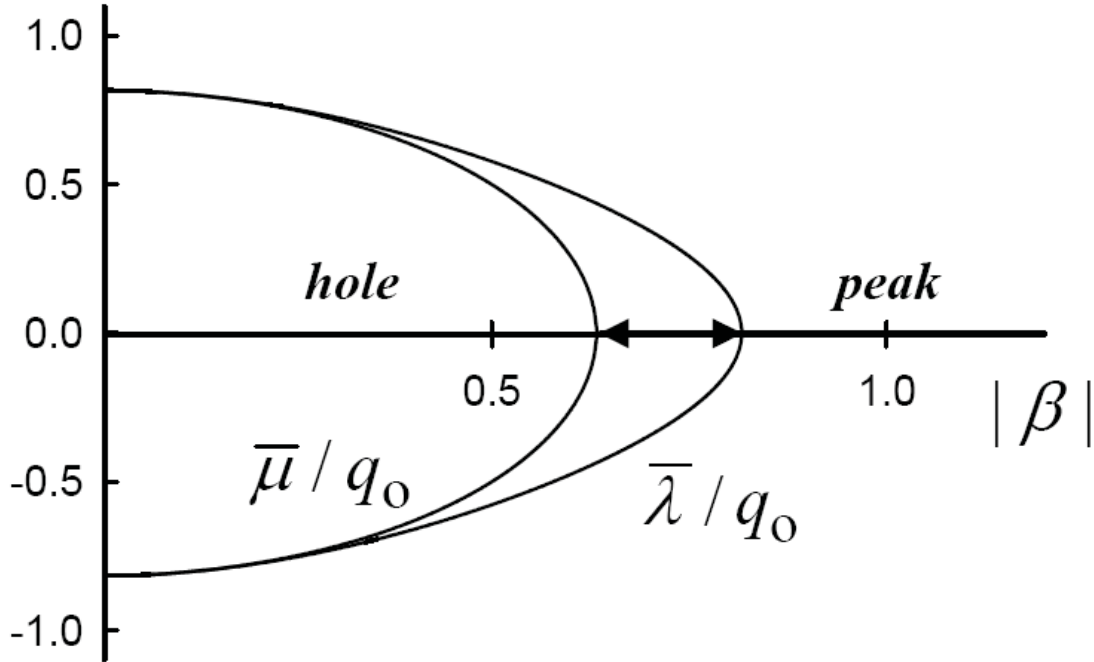


Figure 3.7 The location of the maxima as a function of  $|\beta|$ .

The graph shows the location of the maxima along the coordinate axes in the  $\bar{\lambda}\bar{\mu}$ -plane as a function of  $|\beta|$ . For  $|\beta| < \sqrt{2/5}$  there are two maxima along both axes, and there is a hole in the middle. For  $|\beta| > \sqrt{2/3}$  there is a single peak near the origin of coordinates. In the region indicated by  $\leftrightarrow$ , there is a minimum along the  $\bar{\lambda}$  direction and a maximum along the  $\bar{\mu}$  direction near the origin.

At the center of the profile we have a minimum, a maximum, or a transition between the two, and at the location of this extremum we have  $\bar{\lambda} = 0$  and  $\bar{\mu}/q_0 = 0$ . Just as for the circular dipole, the condition  $\bar{\mu}/q_0 = 0$  leaves open the possibility that  $\bar{\mu}$  is finite. In Eq. (3.24) we let  $\bar{\mu}/q_0 \rightarrow 0$ . We then obtain for the coordinates of the extremum around the origin of the image plane

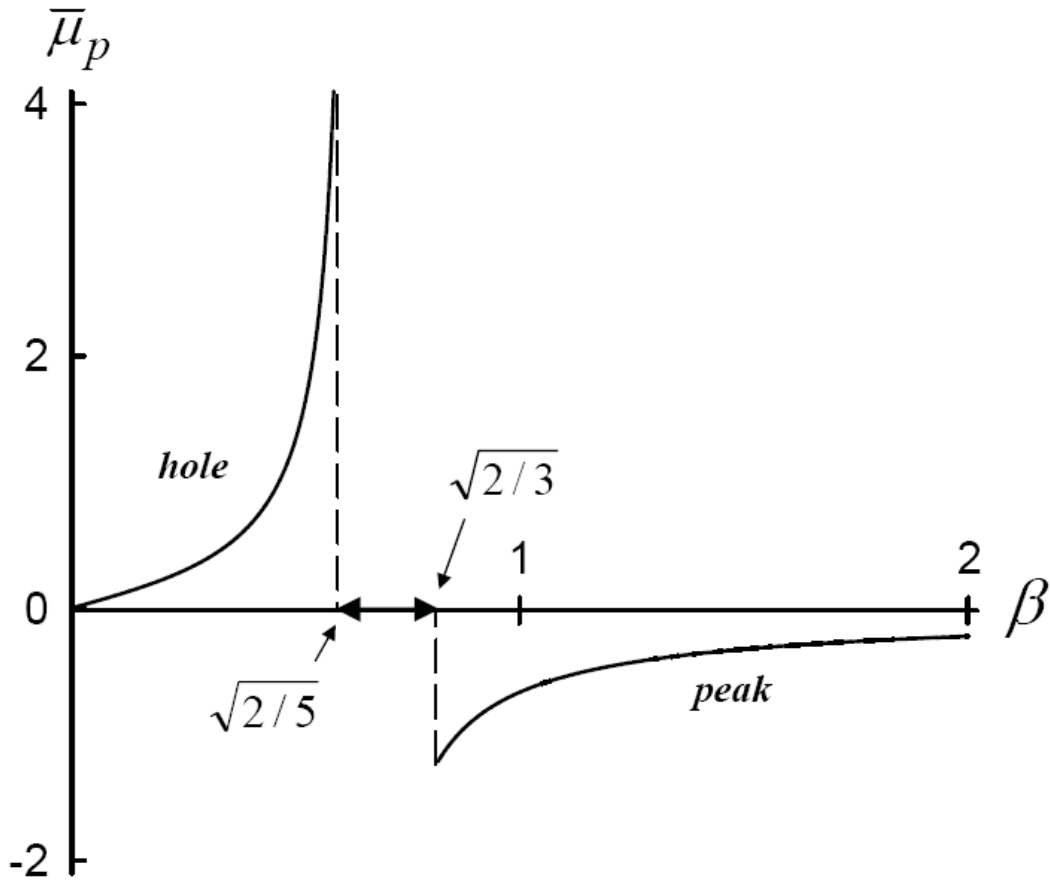


Figure 3.8 The shift  $\bar{\mu}_p$  for  $\beta \geq 0$ .

The graph shows the shift  $\bar{\mu}_p$  for  $\beta \geq 0$  of either the hole or the peak with respect to the origin of coordinates. In the transition region  $\sqrt{2/5} < \beta < \sqrt{2/3}$ , there is neither a hole nor a peak in the intensity distribution.

$$\bar{\lambda}_p = 0 \quad , \quad \bar{\mu}_p = \frac{2\beta}{2-5\beta^2} \quad . \quad (3.26)$$

The finite shift  $\bar{\mu}_p$  is again a result of the rotation in the field lines near the source. Figure 3.8 shows  $\bar{\mu}_p$  as a function of  $\beta$  for  $\beta$  positive. For  $0 \leq \beta < \sqrt{2/5}$  the extremum is a hole, as shown in Fig 3.9.

Eq. (3.26) represents the shift of the hole with respect to the origin. We see from the figure that the shift of the hole is in the positive  $\bar{\mu}$ -direction. In the region  $\beta > \sqrt{2/3}$ , the extremum is a peak, and the shift is in the negative direction. For  $\beta$  negative, the hole shifts in the negative direction and the peak shifts in the positive direction. For a circular dipole we have  $|\beta|=1$  and the magnitude of the shift of the peak is equal to  $|\bar{\mu}_p|=2/3$ , as in Fig. 3.5. This shift increases with decreasing  $|\beta|$ , and at  $|\beta|=\sqrt{2/3}$  the magnitude of the shift is  $|\bar{\mu}_p|=\sqrt{3/2}$ . This is a factor of 1.84 larger than the shift for a circular dipole. The shift of the hole for  $|\beta|<\sqrt{2/5}$  can be extremely large, but the depth and sharpness of the hole decrease with increasing shift.

### 3.4 Intensity in the Near Field

Thus far we have considered the intensity distribution in the far field. With contemporary experimental techniques, it has become feasible to detect electromagnetic radiation with nanoscale resolution very close to a source. In these experiments the electric field vector is measured, including its direction, within a fraction of a wavelength from the source. From these measurements, a field line pattern for the electric field can be obtained, and it should be possible to construct the field lines of the Poynting vector from these data. Figure 3.10 shows a typical intensity distribution on an image plane in the near field for a rotating dipole moment. The positive peak at the left-hand side comes from the field lines passing through the plane in the outward direction, and the negative peak on the right represents field lines passing the plane in the opposite direction. This

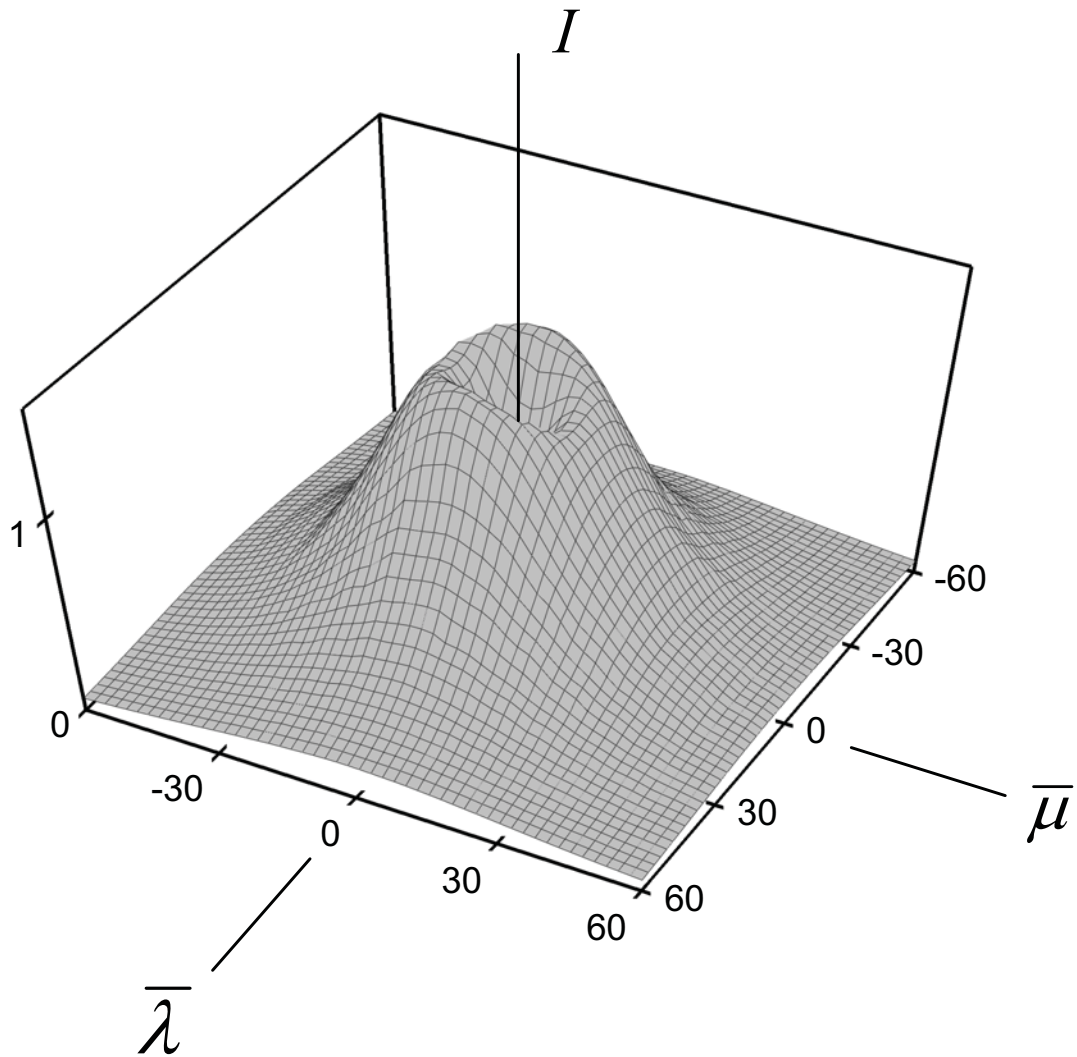


Figure 3.9 The intensity distribution for an elliptical dipole moment with  $\beta = 0.4$ .

The minimum of the hole is located at  $\bar{\lambda} = 0$ ,  $\bar{\mu} = 2/3$ , but that can not be seen in the figure.

image is a direct consequence of the spiraling of the field lines near the source. A field line can pass through the plane on the left, and then this same field line can cross the image plane again in the opposite direction on the right.



### 3.5 Macroscopic Far-Field Observation of the Near-Field Dipole Vortex

The shifts of the peak in Fig. 3.5 and the hole in Fig. 3.9 are of the same order of magnitude as the spatial extent of the dipole vortex in Fig. 3.1. On one hand, this shift leads to a possible observation of the dipole vortex through a measurement in the far field, but on the other hand, this shift is extremely small. It also requires a precise calibration of the experimental setup, since the shift is measured with respect to the origin of the image plane. Furthermore, the profile has a large background, as can be seen from the figures, and the shape of this background (peak, hole or a more complicated distribution) depends on the observation angles  $\theta_0$ ,  $\phi_0$ , and on the parameter  $\beta$  of the ellipse.

The shift of the peak or hole depends on the sign of  $\beta$ . The peak in Fig. 3.5 moves to  $\bar{\mu} = +2/3$  when we reverse the direction of rotation of the dipole, so when we change the sign of  $\beta$ . This is obvious from Fig. 3.1, since changing the direction of rotation results in the field lines swirling around the  $z$ -axis in the opposite direction. The asymmetry in the intensity distribution comes from the rotation of the field lines near the source. In an experiment, changing the direction of rotation can be accomplished by changing the helicity of the driving laser, and this would result in the moving of the peak or hole to the opposite direction.

#### 3.5.1 The Difference Profile

We now introduce the difference profile

$$\Delta I(\lambda, \mu; \beta) = I(\lambda, \mu; \beta) - I(\lambda, \mu; -\beta) . \quad (3.27)$$

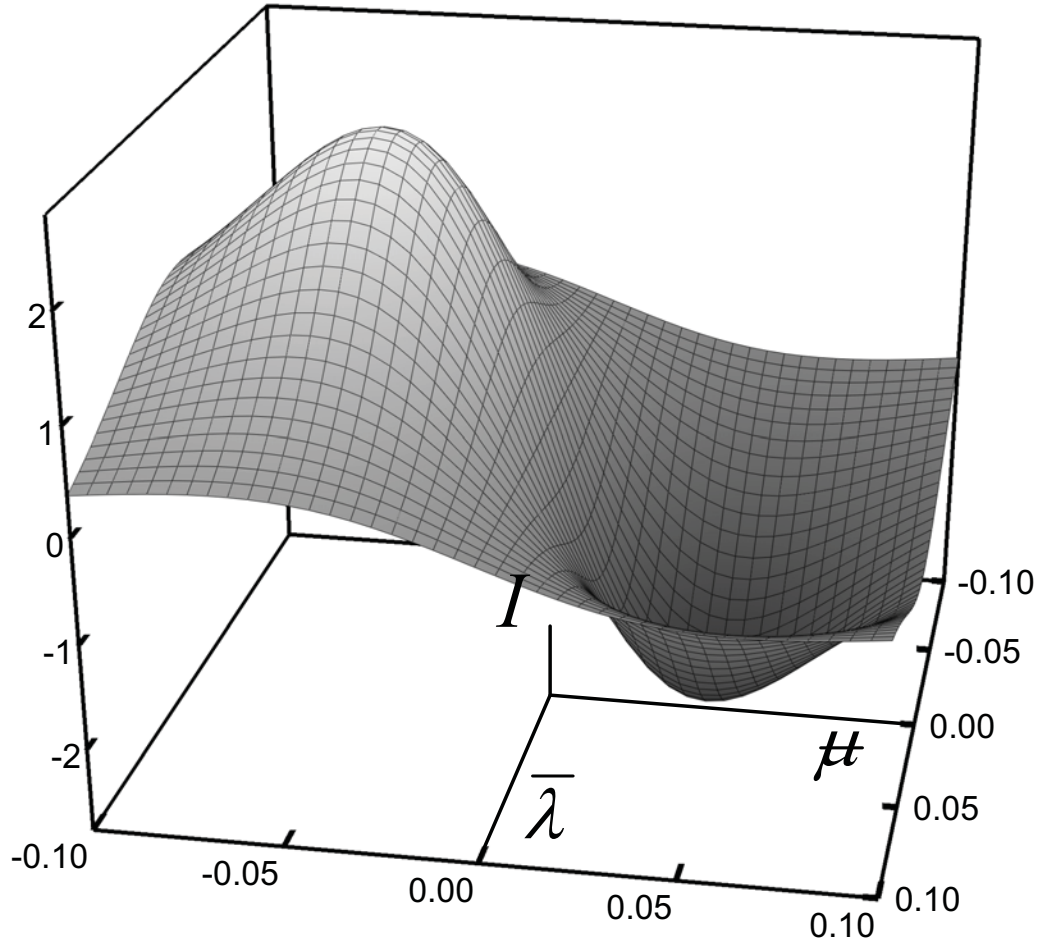


Figure 3.10 The near-field intensity distribution for a dipole with  $\beta = 1$ .

When observed in an image plane perpendicular to the  $y$ -axis ( $\theta_0 = \phi_0 = \pi/2$ ), shows a positive and a negative extremum. This is due to the fact that the field lines of the Poynting vector cross the plane in the outward direction at the negative  $\bar{\mu}$  side, and re-enter the image plane at the positive  $\bar{\mu}$  side. This profile is a result of the numerous rotations of the field lines around the  $z$ -axis close to the source, as shown in Fig. 3.1.

The idea is that in this difference the large background will cancel, and only the asymmetry due to the rotation of the field lines will contribute to this profile. Therefore, any observation of  $\Delta I \neq 0$  in the far field would confirm the rotation of the field lines in the near field.

From Eq. (3.7) we find

$$\Delta I(\lambda, \mu; \beta) = -\frac{\zeta}{q^4} \left( 1 + \frac{1}{q^2} \right) \bar{\mu} \quad , \quad (3.28)$$

with

$$\zeta = \frac{3P_0 k_0^2}{2\pi} \frac{\beta}{\beta^2 + 1} \sin \theta_0 \quad , \quad (3.29)$$

and

$$q = \sqrt{q_0^2 + \bar{\lambda}^2 + \bar{\mu}^2} \quad , \quad (3.30)$$

as the dimensionless distance between the dipole and the observation point in the image plane. The difference profile is independent of the observation angle  $\phi_0$ , and the dependence on  $\theta_0$  only enters through  $\sin \theta_0$  in the overall factor  $\zeta$ . Therefore,  $\Delta I = 0$  for observation on the  $z$ -axis. The parameter  $\beta$  of the ellipse only appears in the overall constant  $\zeta$ . Consequently, apart from an overall constant, the difference profile is independent of the observation angles and is the same for any ellipse.

The profile in the image plane is a function of the dimensionless coordinates  $\bar{\lambda}$  and  $\bar{\mu}$ , with  $q_0$  as the only parameter. The function  $\Delta I$  is symmetric in  $\bar{\lambda}$  and antisymmetric in  $\bar{\mu}$ . It is easily verified from Eqs. (3.28) and (3.30) that  $\Delta I$  has two

extrema on the  $\bar{\mu}$ -axis, symmetrically located with respect to the origin. Figure 3.11 shows  $\Delta I$  for  $q_0 = 20$ , and  $\beta$  positive. For  $\beta$  negative, the overall constant  $\zeta$  changes sign and the maximum and minimum switch positions. If we indicate the positions of the extrema by  $\pm \bar{\mu}_e$ , then for the far field, where  $q_0 \gg 1$ , we obtain

$$\bar{\mu}_e = \frac{q_0}{\sqrt{3}} . \quad (3.31)$$

The location of the peak in Fig. 3.5 is at  $\bar{\mu} = -2/3$ , and this is a displacement of about one-tenth of a wavelength with respect to the origin. The extrema of the difference profile are proportional to  $q_0$ , so their location is proportional to the distance between the dipole and the image plane. Therefore, these extrema are at macroscopic distances from the origin, even though they are a result of the microscopic vortex near the dipole. Figure 3.12 shows the location of the extrema with respect to the dipole. As viewed from the dipole, they appear under an angle  $\gamma$ , with  $\tan \gamma = \bar{\mu}_e / q_0$ , and this gives  $\gamma = 30^\circ$ .

The expression for the difference profile holds for all distances  $q_0$ . If  $\Delta I$  would be measured in the near field, for which  $q_0 \ll 1$ , we would have  $\bar{\mu}_e / q_0 = 1/\sqrt{5}$ , and this would give  $\gamma = 24^\circ$ . Therefore, the angular positions of the extrema are in the range  $24^\circ < \gamma < 30^\circ$ .

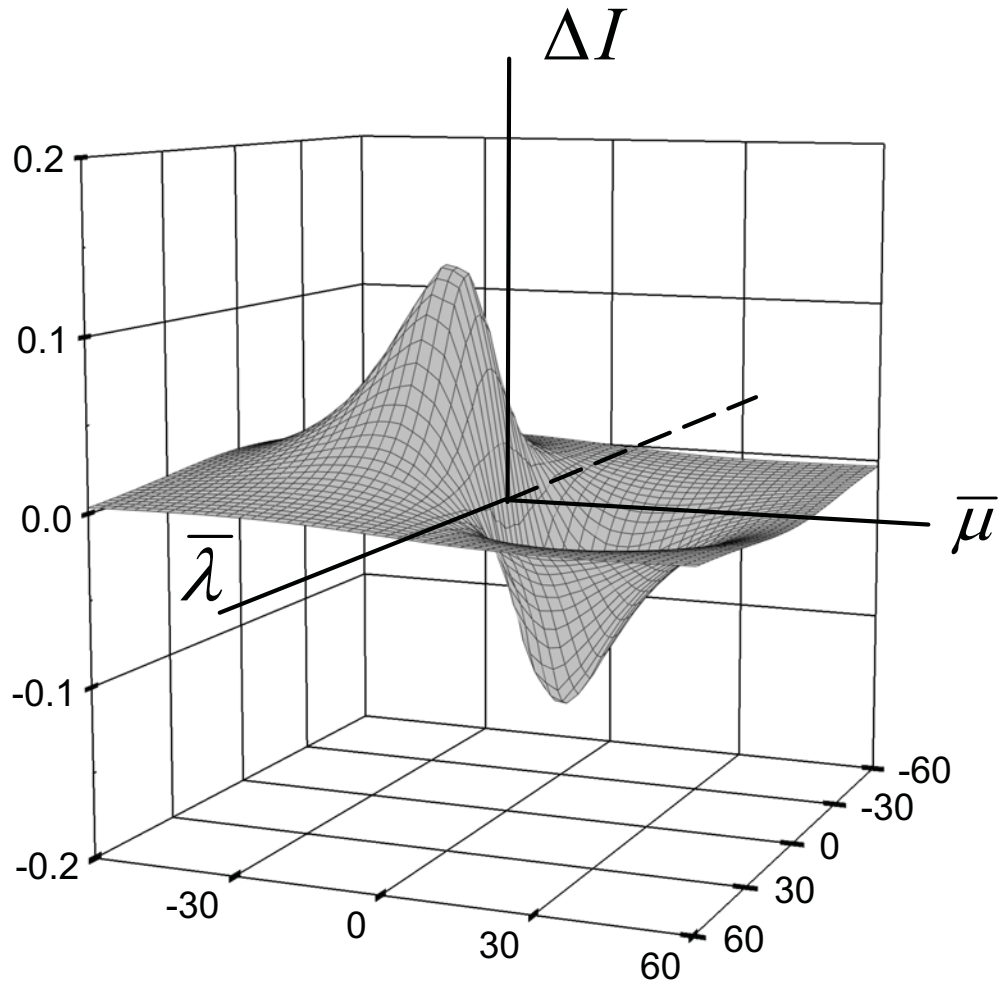


Figure 3.11 The difference profile  $\Delta I$ .

The figure shows the difference profile  $\Delta I$  in the  $(\bar{\lambda}, \bar{\mu})$  plane is shown for  $q_0 = 20$  and  $\beta$  positive. The maxima and minima are located on the  $\bar{\mu}$ -axis at  $\bar{\mu} = -11.5$  and  $\bar{\mu} = 11.5$ , respectively.

### 3.5.2 Experimental Setup and Results

In a recent experiment [41], the difference profile was measured for a small polystyrene sphere with a diameter of  $4.6 \mu\text{m}$  in a circularly polarized laser beam with a wavelength of  $532 \text{ nm}$ . The setup of the experiment is shown in Fig. 3.13. The

observation angle was  $\theta_0 = \pi/2$ . The experimental results are in good qualitative agreement with Fig. 3.12. In the experimental data, as shown in Fig. 3.14, there are some small oscillations in the wings which are probably due to the finite size of the object.

The field lines of the Poynting vector for dipole radiation swirl around an axis in the near field, and approach a straight line in the far field, except for a linear dipole for which the field lines are straight at all distances to the source. This vortex structure, shown in Fig. 2.7, has the dimension of an optical wavelength or less, so it manifests itself in the near field. However, as also shown in Fig. 2.7, it leads to an asymptotic displacement of the field lines in the far field. In order to observe indirectly the existence of the vortex in the near field, we consider the intensity distribution in the far field, and as suggested in Fig. 3.1, we anticipate that the displacement of the field lines due to the vortex in the near field will yield a shift of the intensity profile in the far field.

We have considered the intensity distribution on a plane in the far field for a dipole with an elliptical dipole moment, rotating in the  $xy$ -plane. In the image plane we define a rectangular coordinate system  $(\lambda, \mu)$ , associated with the spherical-coordinate angles  $(\theta_0, \phi_0)$  of the location of the image plane, as illustrated in Fig. 3.2. For a circular dipole, the intensity distribution is a single peak in the image plane. The maximum along the  $\lambda$ -axis is located at  $\bar{\lambda}_p = \alpha q_0$  (in dimensionless coordinates), where  $\alpha$  is a function of the angle  $\theta_0$  of the image plane, as shown in Fig. 3.4. The location of this maximum scales with  $q_0$ , which is the dimensionless distance between the dipole and the image plane. Therefore, the position of this maximum along the  $\lambda$ -axis is simply a result of the non-

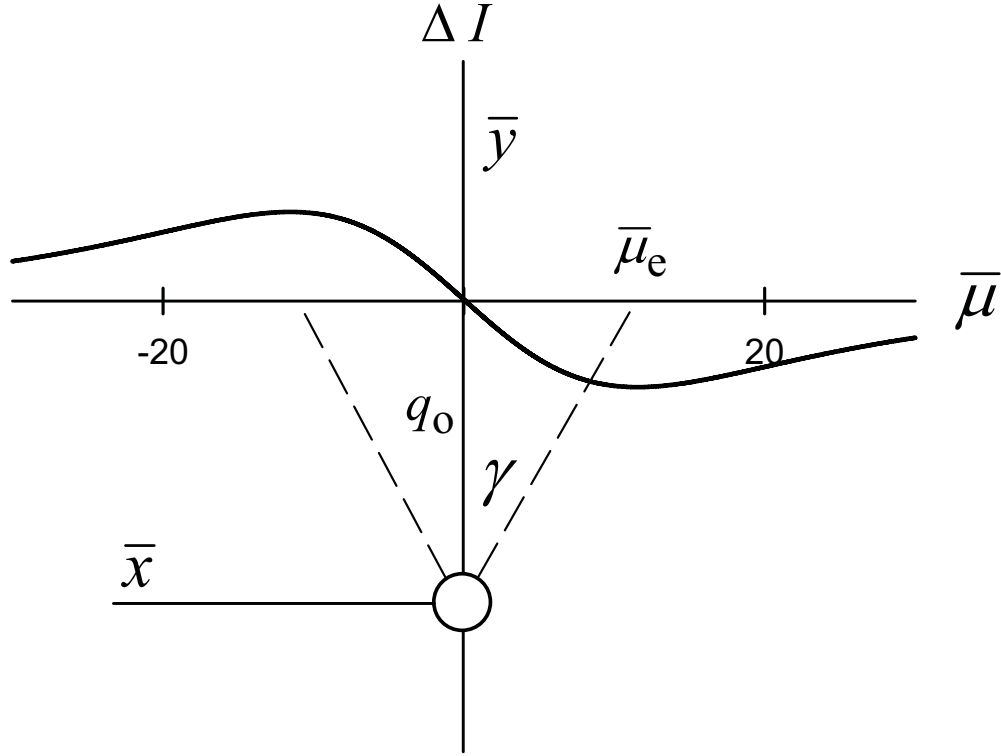


Figure 3.12 The extrema on the  $\bar{\mu}$ -axis are located at  $\bar{\mu}_e$  and  $-\bar{\mu}_e$ .

For  $\beta > 0$ , as in the figure, the maximum is at the negative side of the  $\bar{\mu}$ -axis. Both extrema appear under angle  $\gamma$  as seen from the location of the dipole. For the figure we took  $q_0 = 20$ , which is just over three optical wavelengths. Here,  $\gamma = 30^\circ$ , and when we increase  $q_0$  this angle remains  $30^\circ$ .

uniformity of the emitted power per unit solid angle. The position of the maximum along the  $\mu$ -axis is given by Eq. (3.20), and this position does not scale with  $q_0$ . It is a finite shift of the peak, resulting from the displacement of the field lines of the Poynting vector, and it is due to the presence of the vortex in the near field. In this fashion, a near field

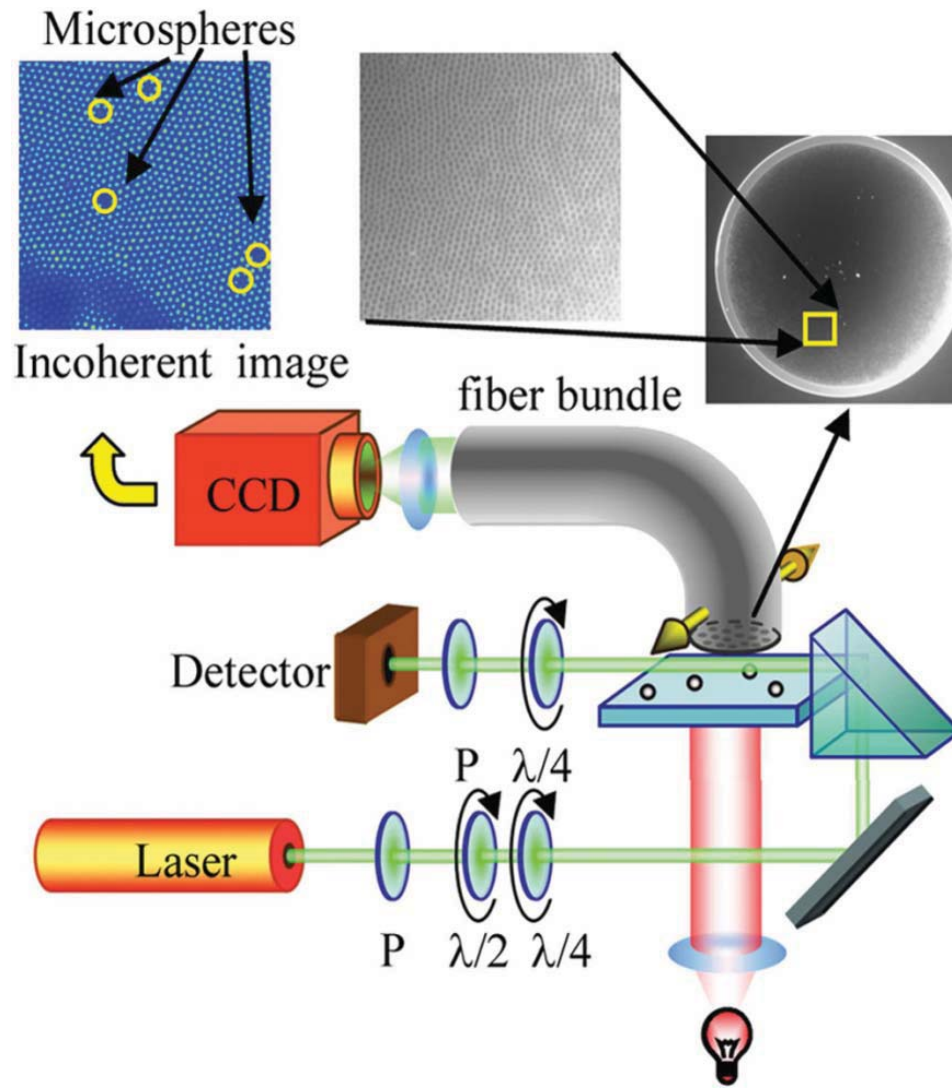


Figure 3.13 Experimental setup.

Polystyrene spheres with a diameter of 4.62 micrometer were sparsely distributed upon a microscope slide. The circularly polarized coherent laser light was used as an excitation and a prism was employed to adjust the plane of illumination. The scattered light was collected through a coherent imaging fiber bundle. The position of individual particles was detected and monitored using an additional, incoherent illumination from underneath the sample. A cooled CCD array was used to both image the sphere and to detect the scattered intensity at desired locations.

[Reproduced from Ref. 41, with permission from the American Physical Society]



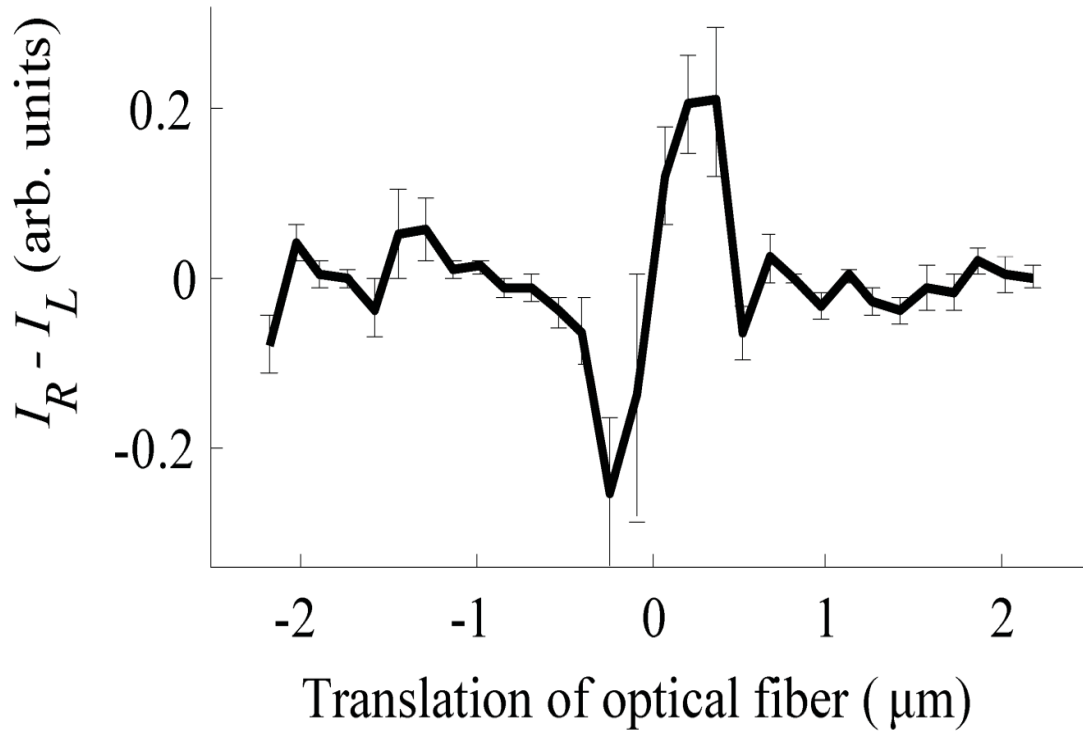


Figure 3.14 Experimental data.

Shown are the experimental results for  $\Delta I$ . Here,  $I_R$  is the case of right circular polarized light, which means  $\beta = 1$ , and  $I_L$  represents  $\beta = -1$ . The data was obtained through a single mode fiber scanned across a polystyrene sphere of 4.6 micrometer diameter.

[Reproduced from Ref. 41, with permission from the American Physical Society]

phenomenon is reflected in a far field intensity profile, and therefore it should be possible to verify the existence of the vortex through a far field measurement.

However, the intensity shift is of sub-wavelength order, which may be difficult to detect. We propose to detect the vortex in the near field through a measurement of the difference profile in the far field. The intensity for a rotating dipole is measured at a

given point in the observation plane. Then the helicity of the driving laser is reversed, and the new intensity is subtracted from the first. We have shown that this difference profile is a universal function, with only the distance between the dipole and the observation plane as a free parameter. Apart from an overall factor for a given observation plane and state of rotation of the dipole (the  $\beta$  of the ellipse), any profile has a peak and a hole as shown in Fig. 3.11. The location of the extrema is independent of the angular position  $(\theta_0, \phi_0)$  of the observation plane, and independent of the magnitude of  $\beta$ . When  $\beta$  changes sign, the peak and the hole reverse positions. The most important property of the difference profile is that the locations of the extrema are not of sub-wavelength order. The angular location  $\gamma$  of the extrema, as shown in Fig. 3.12, is  $30^\circ$  when the profile is observed in the far field (a few wavelengths or more from the dipole). The distance between the peak and the hole is proportional to the distance between the dipole and the observation plane, since  $\gamma$  remains constant. Therefore, the separation between the extrema is of macroscopic order, even though they are a result of the nanoscopic vortex near the source. Without the vortex, the difference profile would be identically zero, and consequently any macroscopic far-field observation of a  $\Delta I$  as in Fig. 3.11 would confirm the existence of this vortex.

## CHAPTER IV

### ELECTRIC DIPOLE RADIATION NEAR A MIRROR

In the previous chapters we have been discussing dipole radiation and its intensity distribution in free space. From Eq. (2.11) we were able to calculate the energy flow lines of dipole radiation. Figure 4.1 shows the field lines of the Poynting vector for a free linear dipole. No radiation is emitted along the dipole axis ( $\alpha = 0$  in Eq. (2.11)), and the field lines are drawn more dense into the directions of maximum power per unit solid angle ( $\alpha = \pi/2$ ). In a 3D view, the picture is rotationally symmetric around the dipole axis.

We now consider the dipole located on the  $z$ -axis, a distance  $H$  above a mirror, and the surface of the mirror is taken as the  $xy$ -plane. The position vector of the dipole is given by  $H\mathbf{e}_z$ , and when we let  $\mathbf{r}_1$  be the location of a field point with respect to the position of the dipole, then the position vector of that field point with respect to the origin is given by  $\mathbf{r} = H\mathbf{e}_z + \mathbf{r}_1$ . The setup is illustrated in Fig. 4.2. The complex amplitudes  $\mathbf{E}(\mathbf{r})_s$  and  $\mathbf{B}(\mathbf{r})_s$  of this source are given by Eqs. (2.6) and (2.7) with the replacements  $\hat{\mathbf{r}} \rightarrow \hat{\mathbf{r}}_1$ , the unit vector in the  $\mathbf{r}_1$  direction, and  $q \rightarrow q_1 = k_0 r_1$ , the dimensionless distance between the dipole and the field point. The  $y$ -axis is taken such that the dipole vector  $\mathbf{e}$  is in the  $yz$ -plane. The dipole axis makes an angle  $\gamma$  with the  $z$ -axis, and therefore

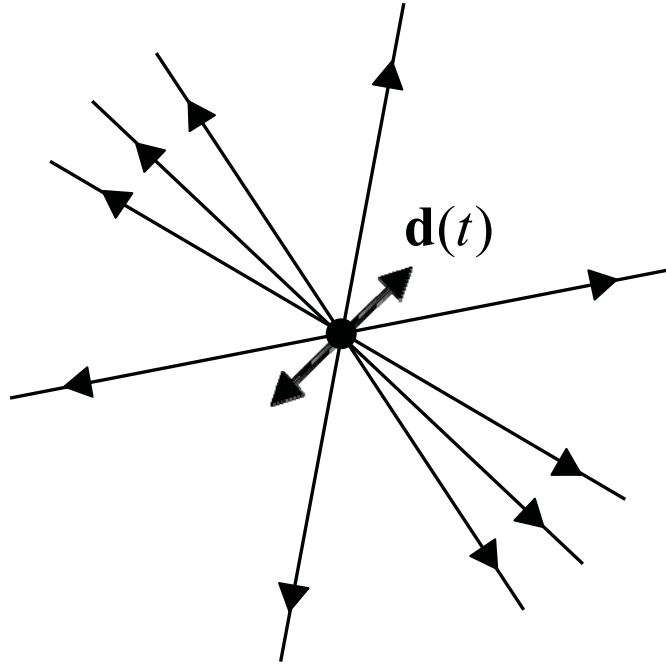


Figure 4.1 Field lines of the Poynting vector for a linear dipole.

vector  $\boldsymbol{\varepsilon}$  is

$$\boldsymbol{\varepsilon} = \mathbf{e}_y \sin \gamma + \mathbf{e}_z \cos \gamma \quad . \quad (4.1)$$

The reflected field by the mirror is identical to the field of an image dipole, located at  $-H\mathbf{e}_z$  and with dipole moment  $d_0 \boldsymbol{\varepsilon}^{\text{im}} \cos(\omega t)$ , where [42]

$$\boldsymbol{\varepsilon}^{\text{im}} = -\mathbf{e}_y \sin \gamma + \mathbf{e}_z \cos \gamma \quad . \quad (4.2)$$

The complex amplitudes  $\mathbf{E}(\mathbf{r})_r$  and  $\mathbf{B}(\mathbf{r})_r$  of the reflected field are as in Eqs. (2.6) and (2.7) with  $\boldsymbol{\varepsilon} \rightarrow \boldsymbol{\varepsilon}^{\text{im}}$ ,  $\hat{\mathbf{r}} \rightarrow \hat{\mathbf{r}}_2$ ,  $q \rightarrow q_2 = k_0 r_2$ , and vector  $\mathbf{r}_2$  is the position vector of the field point with respect to the location of the image dipole, as shown in Fig. 4.2. The

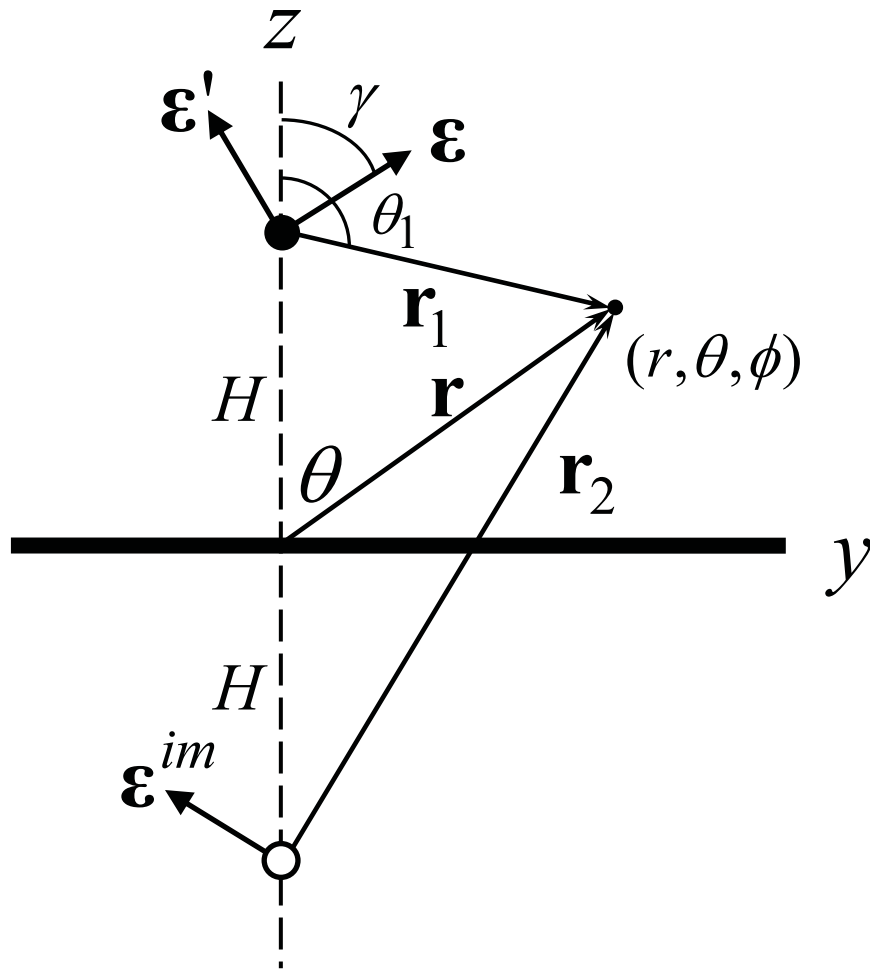


Figure 4.2 A dipole is located on the  $z$ -axis, a distance  $H$  above a mirror.

The dipole oscillates along the direction indicated by vector  $\boldsymbol{\varepsilon}$ , which makes an angle  $\gamma$  with the  $z$ -axis. The reflected field is identical to the field by an image dipole, located at a distance  $H$  below the mirror, and on the  $z$ -axis. The image dipole oscillates along the direction  $\boldsymbol{\varepsilon}^{im}$ , which is also under angle  $\gamma$  with the  $z$ -axis, but it has its horizontal component reversed as compared to  $\boldsymbol{\varepsilon}$ . Vector  $\boldsymbol{\varepsilon}'$  is perpendicular to  $\boldsymbol{\varepsilon}$ . A field point can be represented by vector  $\mathbf{r}$  with respect to the origin, or by vector  $\mathbf{r}_1$  or  $\mathbf{r}_2$  with respect to the dipole or the image dipole, respectively. A field point can also be represented by the spherical coordinates  $(r, \theta, \phi)$  with respect to the origin or the spherical coordinates  $(r_1, \theta_1, \phi)$  with respect to the position of the dipole.

total field in the region  $z > 0$  is then the sum  $\mathbf{E}(\mathbf{r}) = \mathbf{E}(\mathbf{r})_s + \mathbf{E}(\mathbf{r})_r$ ,  $\mathbf{B}(\mathbf{r}) = \mathbf{B}(\mathbf{r})_s + \mathbf{B}(\mathbf{r})_r$ . It can be verified explicitly that this field satisfies the boundary conditions for a perfect conductor at  $z = 0$ , e.g., the parallel part of  $\mathbf{E}(\mathbf{r})$  and the perpendicular part of  $\mathbf{B}(\mathbf{r})$  vanish.

With  $\mathbf{E}(\mathbf{r})$  and  $\mathbf{B}(\mathbf{r})$  constructed, the Poynting vector  $\mathbf{S}(\mathbf{r})$  from Eq. (2.10) can be computed. The expression is rather lengthy, and is given in Appendix A. The result for  $\mathbf{S}(\mathbf{r})$  defines a vector field in space, and a field line of  $\mathbf{S}(\mathbf{r})$  is a curve for which at any point along the curve the vector  $\mathbf{S}(\mathbf{r})$  is on its tangent line. First we set

$$\mathbf{S}(\mathbf{r}) = \frac{3P_0}{8\pi r_1^2} \boldsymbol{\sigma}(\mathbf{r}) \quad , \quad (4.3)$$

so that  $\boldsymbol{\sigma}(\mathbf{r})$  is dimensionless. Since a field line is only determined by the direction of  $\mathbf{S}(\mathbf{r})$ , and not its magnitude, the field lines of  $\boldsymbol{\sigma}(\mathbf{r})$  are the same as the field lines of  $\mathbf{S}(\mathbf{r})$ . For a field point  $\mathbf{r}$  we set  $\mathbf{q} = k_0 \mathbf{r}$  for its dimensionless representation. Let  $\mathbf{q}(u)$  be a parametrization of a field line, with  $u$  a dummy variable. The field lines  $\mathbf{q}(u)$  are solutions of the autonomous differential equation

$$\frac{d\mathbf{q}}{du} = \boldsymbol{\sigma}(\mathbf{q}) \quad . \quad (4.4)$$

The field lines in the figures below are made by numerical integration of Eq. (4.4). Some aspects of the numerical integration can be found in Appendix B, which also includes a sample program.

At the surface of the mirror,  $\mathbf{E}(\mathbf{r})$  is perpendicular to the surface and  $\mathbf{B}(\mathbf{r})$  is in the  $xy$ -plane. It then follows from Eq. (2.10) that  $\mathbf{S}(\mathbf{r})$  is in the  $xy$ -plane, and therefore any field line that approaches the mirror is expected to bend smoothly away from it, as suggested in Fig. 1.3b.

#### 4.1 Emission of Radiation

For a free dipole the radiation is emitted in all directions, as shown in Fig. 4.1, and the Poynting vector is radially outward at any field point. We now consider the radiation field in close vicinity of the dipole for a dipole located near a mirror. We shall use spherical coordinates  $(r_1, \theta_1, \phi)$  with respect to the location of the dipole, and set  $q_1 = k_0 r_1$  for the dimensionless distance between the dipole and the field point. Both the electric and magnetic field of the source diverge when approaching the dipole. The electric field diverges as  $\mathcal{O}(1/q_1^3)$  and the magnetic field goes as  $\mathcal{O}(1/q_1^2)$ , as follows from Eqs. (2.6) and (2.7), respectively. The reflected field emanates from the image dipole, and close to the dipole both the electric and magnetic field (amplitudes) are constant. Therefore, the electric and magnetic fields close to the dipole are dominated by the emitted field by the source. One may therefore expect that close to the dipole the field lines of the Poynting vector come out of the dipole, as in Fig. 4.1, and at some distance from the dipole the reflected field becomes comparable to the source field, and interference sets in. This would then lead to a flow line pattern as sketched in Fig. 1.3b.

We shall now show that this is not the case.

The Poynting vector  $\boldsymbol{\sigma}(\mathbf{q})$  (with a factor split off as in Eq. (4.3)) is given by Eq (A11), and it has only  $\gamma$  and  $h$ , with  $h = k_0 H$ , as free parameters. We consider the region close to the dipole, such that  $q_1 \ll 1$  and  $q_1 \ll h$ . In physical terms this means that we consider field points that are close to the dipole as compared to a wavelength, and we assume that the distance between the mirror and the dipole is much larger than the distance between the dipole and the field point. The Poynting vector  $\boldsymbol{\sigma}(\mathbf{q})$  can be expanded in a series in  $q_1$ , and it is shown in Appendix C that the result is

$$\boldsymbol{\sigma}(\mathbf{q}) = \frac{\sin \gamma}{q_1} v(h) [(3 \cos^2 \alpha - 1) \boldsymbol{\varepsilon}' - 3 \cos \alpha (\hat{\mathbf{q}}_1 \cdot \boldsymbol{\varepsilon}') \boldsymbol{\varepsilon}] + \hat{\mathbf{q}}_1 \sin^2 \alpha + O(1) . \quad (4.5)$$

Here we have introduced the function

$$v(h) = \frac{1}{2h} \left[ \frac{\sin(2h)}{2h} - \cos(2h) \right] , \quad (4.6)$$

and  $\alpha$  is the angle between  $\boldsymbol{\varepsilon}$  and the observation direction  $\hat{\mathbf{q}}_1$ , e.g.,  $\cos \alpha = \boldsymbol{\varepsilon} \cdot \hat{\mathbf{q}}_1$ , as in Eq. (2.21). Vector  $\boldsymbol{\varepsilon}'$  is defined as

$$\boldsymbol{\varepsilon}' = -\mathbf{e}_y \cos \gamma + \mathbf{e}_z \sin \gamma . \quad (4.7)$$

This vector is perpendicular to  $\boldsymbol{\varepsilon}$ , and is directed as shown in Fig. 4.2.

Without the mirror, the Poynting vector would be  $\boldsymbol{\sigma}(\mathbf{q}) = \hat{\mathbf{q}}_1 \sin^2 \alpha$ , as in Eq. (2.21), and in Eq. (4.5) this is the second term on the right-hand side. The corresponding field



lines would run straight out from the dipole if this were the leading term at a close distance. In Eq. (4.5), however, the first term is  $O(1/q_1)$ , and for  $q_1$  small enough this term will dominate over the free-dipole term  $\hat{\mathbf{q}}_1 \sin^2 \alpha$ . Since this term is due to interference between the source and the image field, we conclude that very close to the dipole the power flow is determined by interference rather than free emission. The term  $\hat{\mathbf{q}}_1 \sin^2 \alpha$  is  $O(1)$ , as are the remaining terms of the expansion, but it is split off explicitly in Eq. (4.5) for reasons described below.

In the neighborhood of the dipole, the electric field is  $O(1/q_1^3)$  and the magnetic field is  $O(1/q_1^2)$ . When computing the Poynting vector, this may seem to lead to  $\mathbf{S}(\mathbf{r}) = O(1/q_1^5)$ , with Eq. (2.10), and for  $\boldsymbol{\sigma}(\mathbf{q})$  this would be  $O(1/q_1^3)$ . However, the high-order terms cancel exactly and we get  $\boldsymbol{\sigma}(\mathbf{q}) = O(1)$  for a free dipole, and this is the second term on the right-hand side of Eq. (4.5). The cross term between the electric field of the source, which is  $O(1/q_1^3)$ , and the magnetic field of the image, which is  $O(1)$  at the location of the dipole, gives a contribution of  $O(1/q_1)$  to  $\boldsymbol{\sigma}(\mathbf{q})$ , and this is the first term on the right-hand side of Eq. (4.5). Consequently, sufficiently close to the dipole this interference term is larger than the source term  $\hat{\mathbf{q}}_1 \sin^2 \alpha$ .

The emission pattern of the radiation is determined by the energy flow lines in the immediate neighborhood of the source. In order to determine the structure of this pattern we first consider a field point  $\mathbf{q}_1$  in a plane through the dipole, which is perpendicular to vector  $\boldsymbol{\varepsilon}'$ . For such a field point we have  $\hat{\mathbf{q}}_1 \cdot \boldsymbol{\varepsilon}' = 0$ , and therefore the  $O(1/q_1)$  term in Eq. (4.5) is proportional to  $\boldsymbol{\varepsilon}'$ . Consequently, in this plane the Poynting vector  $\boldsymbol{\sigma}(\mathbf{q})$  is

perpendicular to the plane, and the corresponding field lines cross the plane under a  $90^\circ$  angle. The factor of  $3\cos^2\alpha - 1$ , multiplying  $\boldsymbol{\varepsilon}'$ , becomes zero when  $\cos\alpha = \pm 1/\sqrt{3}$ . Since  $\alpha$  is the angle between  $\boldsymbol{\varepsilon}$  and  $\hat{\mathbf{q}}_1$ , the condition  $\cos\alpha = \pm 1/\sqrt{3}$  defines two lines in the plane on which the  $O(1/q_1)$  contribution to the Poynting vector vanishes. These lines are under  $54.7^\circ$  with the  $\boldsymbol{\varepsilon}$  axis, and are indicated by  $\ell_+$  and  $\ell_-$  in Fig. 4.3. Across these semi-singular lines the Poynting vector changes direction and this leads to a rotation of the field lines around these lines in the plane. The orientation of the Poynting vector in this plane is shown in Fig 4.3, and Fig. 4.4 shows several field lines resulting from this rotation. Apparently, when an oscillating electric dipole is located near a mirror, the radiation is emitted in a pattern of four vortices. Each field line swirls around one of the lines  $\ell_+$  and  $\ell_-$  in the plane. Two vortices are in front of the  $yz$ -plane, as shown in Fig. 4.4, and two are in the back. The Poynting vector is proportional to  $v(h)$ , which depends on the distance between the dipole and the surface of the mirror. When  $h$  changes, this function may change sign, and in that case the orientation of the rotation of the field lines around the semi-singular lines reverses.

In Eq. (C4) of Appendix C, the  $O(1)$  term of Eq. (4.5) is given explicitly, and we see that this term vanishes as  $\sim 1/h$  for  $h$  large, except for the free-dipole part  $\hat{\mathbf{q}}_1 \sin^2\alpha$ , which is independent of  $h$ . Therefore, for a field point on a semi-singular line the Poynting vector is approximately equal to  $(2/3)\hat{\mathbf{q}}_1$ , for  $h$  not too small. On these lines the  $O(1/q_1)$  term vanishes, but the Poynting vector is finite, and radially outward. From the diagram in Fig. 4.3 we can easily derive parameter equations for the lines  $\ell_+$  and  $\ell_-$ .

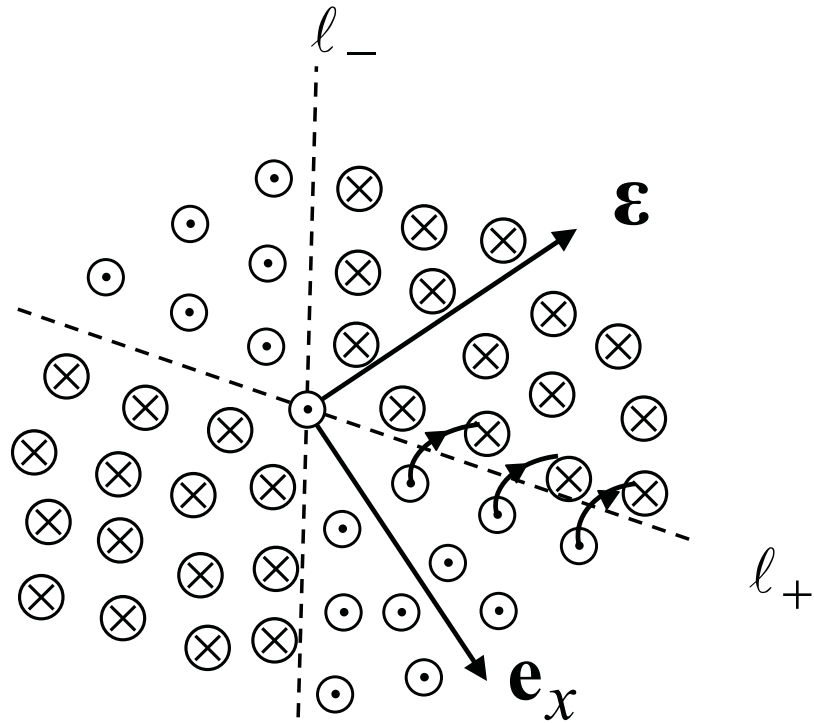


Figure 4.3 The plane through the dipole which is perpendicular to  $\boldsymbol{\varepsilon}'$ .

It follows from Fig. 4.2 that the plane is spanned by vectors  $\boldsymbol{\varepsilon}$  and  $\mathbf{e}_x$ , and the view is such that  $\boldsymbol{\varepsilon}'$  is out of the page. The Poynting vector in this plane is perpendicular to the plane, indicated by  $\otimes$  and  $\odot$ . The Poynting vector  $\boldsymbol{\sigma}(\mathbf{q})$  has an overall factor of  $v(h)\sin\gamma$ , and the orientation is shown for the case where this factor is negative (as in Fig. 4.4). The Poynting vector changes direction across the lines  $l_+$  and  $l_-$ , and this gives rise to a rotation of the field lines around these semi-singular lines. This is shown schematically for the  $l_+$  line. For a field point on the  $\boldsymbol{\varepsilon}'$  axis we have  $\cos\alpha = 0$ , and it then follows from Eq. (4.5) that  $\boldsymbol{\sigma}(\mathbf{q})$  is in the  $\boldsymbol{\varepsilon}'$  direction for  $v(h)\sin\gamma < 0$ . Therefore, at the origin of the plane, the Poynting vector is out of the page.

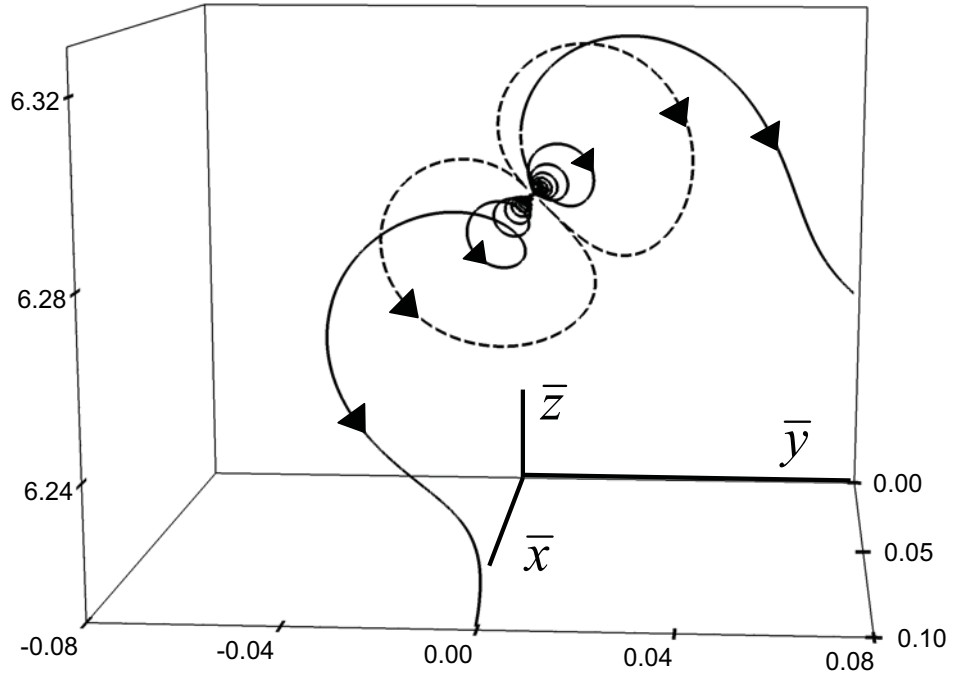


Figure 4.4 Four-vortex structure.

The field lines of the Poynting vector for electric dipole radiation emitted near a mirror exhibit a vortex structure. Shown are field lines for  $\gamma = \pi/4$  and  $h = 2\pi$ . In the region  $x > 0$  the field lines (solid curves) swirl around the semi-singular lines of Fig. 4.3. The dashed field lines are in the  $yz$ -plane, and they are closed loops. The other two vortices are behind the  $yz$ -plane, and are not shown in the figure.

The result is, in matrix form

$$\ell_{\pm} : \begin{pmatrix} \bar{x} \\ \bar{y} \\ \bar{z} \end{pmatrix} = \begin{pmatrix} 0 \\ 0 \\ h \end{pmatrix} + t \begin{pmatrix} \pm\sqrt{2} \\ \sin \gamma \\ \cos \gamma \end{pmatrix}, \quad -\infty < t < \infty, \quad (4.8)$$

where  $\bar{x} = k_0 x$ ,  $\bar{y} = k_0 y$  and  $\bar{z} = k_0 z$  are the dimensionless Cartesian coordinates of points on the lines.

## 4.2 Field Lines in the $yz$ -Plane

The field lines of the Poynting vector are in general curves in 3D. For a field point in the  $yz$ -plane, however, the Poynting vector is in the  $yz$ -plane, and therefore the field lines are 2D curves in the  $yz$ -plane. The vortices from Fig. 4.4 become closed loops when in the  $yz$ -plane, as shown by the dashed curves in Fig. 4.4. Figure 4.5 shows field lines in the  $yz$ -plane (obtained with the exact solution of Appendix A) on a larger scale. The inner two loops are the same as the dashed loops of Fig. 4.4. Vector  $\boldsymbol{\varepsilon}$  (not shown) is under  $45^\circ$  with the  $z$ -axis, and we see that in the neighborhood of the dipole all field lines cross the  $\boldsymbol{\varepsilon}$  axis under  $90^\circ$ , and all run in the same direction, as expected from Fig. 4.3. All field lines along the  $\boldsymbol{\varepsilon}$  axis in Fig. 4.3 go into the page, except for the field line through the origin, which comes out of the page. The result is that in Fig. 4.5 all field lines come out of the dipole along the  $\boldsymbol{\varepsilon}'$ -axis. In the  $yz$ -plane, all radiation is emitted in the same direction, which is the direction perpendicular to the direction of oscillation of the dipole. This in sharp contrast to emission in free space for which radiation is emitted in all directions (except along the dipole axis).

The field lines near the dipole form closed loops. This means that the energy propagating along these field lines returns to the dipole at the other side. The closed loops do not contribute to the overall emitted power, but they give a circulation of power

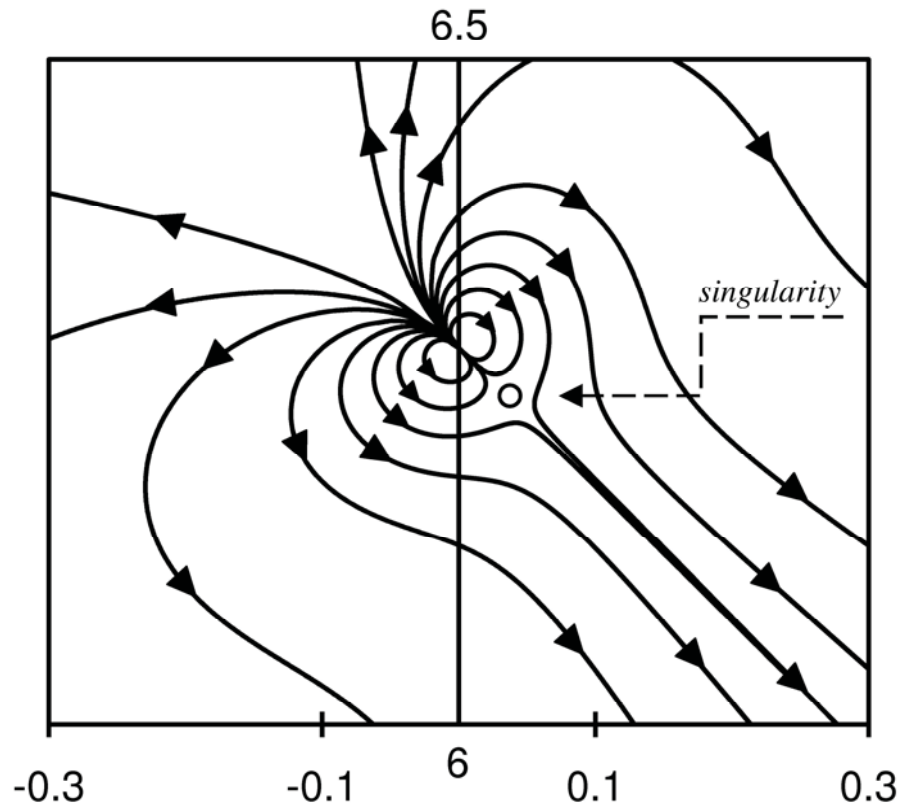


Figure 4.5 The field lines of the Poynting vector for a dipole oscillating above mirror.

The figure shows field lines of the Poynting vector for a dipole oscillating under  $45^\circ$  with the  $z$ -axis, and located at a distance  $h = 2\pi$  above the mirror. The  $z$ -axis is up and the  $y$ -axis is to the right. Very close to the dipole the field lines are closed loops, and just below the dipole a singularity appears.

in the near field. This situation is reminiscent of the case of two oscillating dipoles close together, where energy is emitted by one dipole and is subsequently absorbed by the other dipole. For such a case, field lines run from one dipole to the other, and this mechanism does not contribute to the overall emitted power either [43].

At a larger distance from the dipole, the free-dipole term  $\hat{\mathbf{q}}_1 \sin^2 \alpha$  will eventually become larger than the  $O(1/q_1)$  term, and the field lines will run outward. Since just below the dipole in Fig 4.5 the field lines run into the dipole, we expect a singularity along the  $\boldsymbol{\varepsilon}'$ -axis in this area. For a field point on the  $\boldsymbol{\varepsilon}'$ -axis we have  $\alpha = \pi/2$ . The Poynting vector of Eq. (4.5) becomes

$$\boldsymbol{\sigma}(\mathbf{q}) = \hat{\mathbf{q}}_1 - \frac{\sin \gamma}{q_1} v(h) \boldsymbol{\varepsilon}' + O(1) \quad , \quad (4.9)$$

where the first term,  $\hat{\mathbf{q}}_1$ , is the free-dipole term. At a singularity, the Poynting vector vanishes, and when neglecting the  $O(1)$  term, this occurs at the field point

$$\mathbf{q}_1 = \boldsymbol{\varepsilon}' v(h) \sin \gamma \quad . \quad (4.10)$$

This point is on the  $\boldsymbol{\varepsilon}'$ -axis, and indicated by a little circle in Fig. 4.5. Equation (4.10) gives the distance between the singularity and the dipole as  $|v(h) \sin \gamma|$ . We can view this distance as a measure for the spatial extent of the loops in the very near field of the dipole. For  $\gamma = 0$  this distance is zero, because the  $O(1/q_1)$  is absent. So for a dipole oscillating along the  $z$ -axis there are no loops. For  $\gamma \neq 0$ , the size of the loops is determined by the function  $v(h)$  of Eq. (4.6), and the graph of this function is shown in Fig. 4.6. For  $h$  large, this function falls off as  $\sim 1/h$ , and therefore the radial extension of the loops is approximately  $q_1 \lesssim 1/h$ . Consequently, when the distance between the dipole and the mirror increases, the loops diminish in size. At a root of  $v(h)$  the loops vanish, and when  $v(h)$  reverses sign, the field lines of the loops reverse direction. In that

case, the singularity appears at the top side of the dipole as shown in Fig. 4.7, rather than below it as in Fig. 4.5.

For  $h$  small we have

$$v(h) = \frac{2h}{3} + O(h^3) , \quad (4.11)$$

so for  $h \rightarrow 0$  this function goes to zero. The  $O(1/q_1)$  term, which is responsible for the loops, is proportional to  $v(h)$ , and therefore the loops disappear when the distance  $h$  between the dipole and the mirror vanishes. In the limit  $h \rightarrow 0$  the exact solution of Appendix A can be simplified, and the result is

$$\sigma(\mathbf{q}) = 4\hat{\mathbf{q}} \cos^2 \gamma \cos^2 \theta , \quad (4.12)$$

which holds in 3D. The Poynting vector is proportional to the radial unit vector  $\hat{\mathbf{q}}$  at all distances, and therefore the field lines are straight lines. For  $h \rightarrow 0$  the loops and the singularity disappear, and the four vortices from the previous section are not present either.

The pattern of energy emission in the  $yz$ -plane is illustrated in Fig. 4.5, showing that the field lines either form closed loops or bend somewhat and then run away from the dipole. It can be seen from the scale in the figure that this pattern is of a very sub-wavelength nature. Figure 4.8 shows a larger view of the field lines of energy transport near the mirror. The details of the flow lines of Fig. 4.5 cannot be resolved on the scale of Fig. 4.8. Field lines that run downward from the dipole approach the mirror (the  $xy$ -



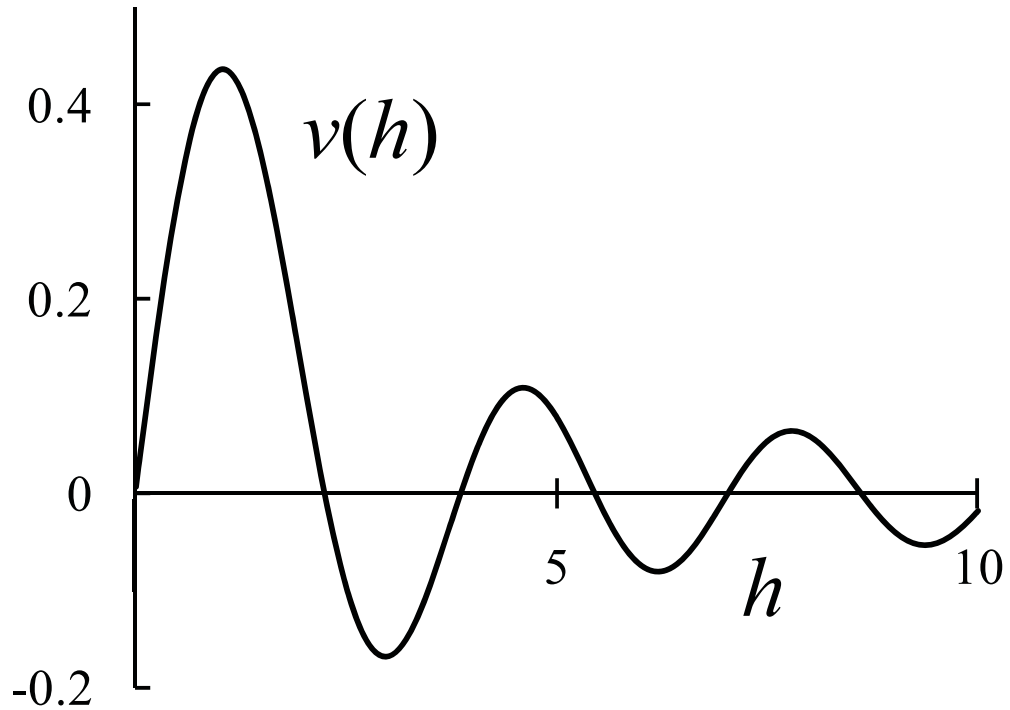


Figure 4.6 The function  $v(h)$ .

The leading term of the Poynting vector in the near field is proportional to the function  $v(h)$  from Eq. (14), which is shown in this graph. This function determines the dependence of this term on the distance between the dipole and the mirror.

plane), and an intricate field line pattern appears due to interference between the source field and the reflected field. We observe numerous singularities and three vortices for the parameters chosen for the figure ( $\gamma = \pi/4$ ,  $h = 2\pi$ ). For other values of the parameters a similar pattern is observed, and typically the number of singularities and vortices increases with  $h$ . On the other hand, for  $\gamma = 0$  there are no singularities (except for point

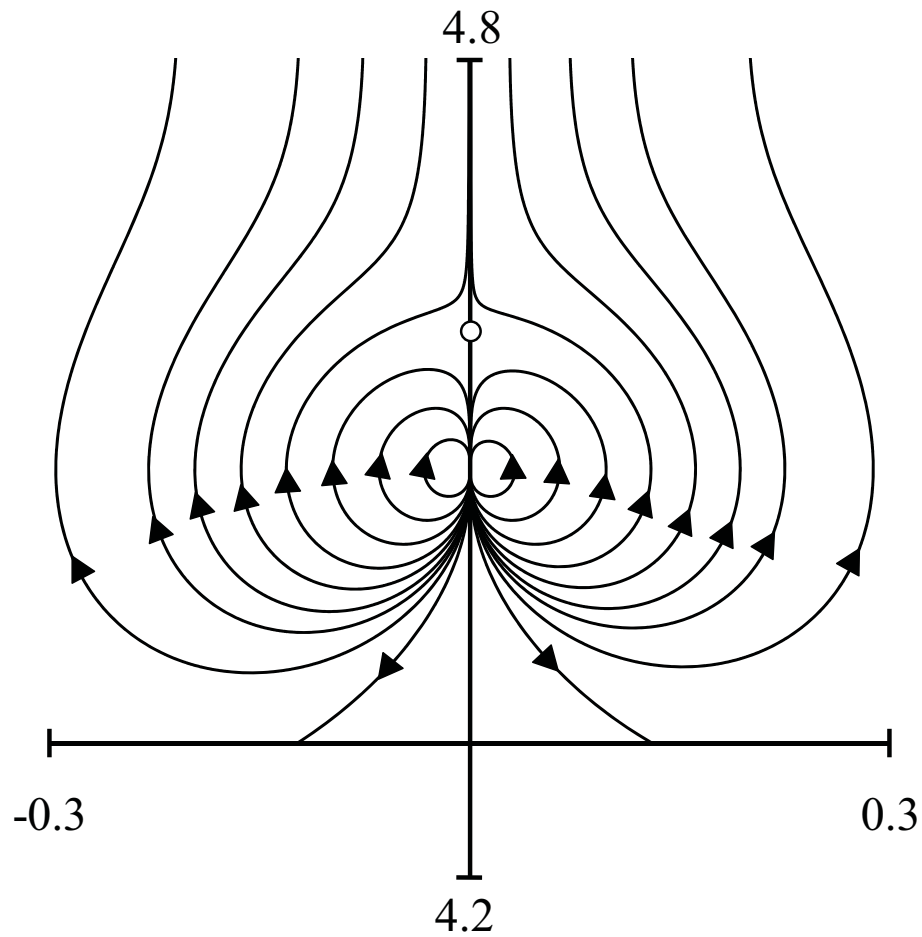


Figure 4.7 Energy flow lines for a dipole oscillating above mirror when  $h = 4.5$ .

The figure shows field lines of the Poynting vector for a dipole oscillating perpendicular to the  $z$ -axis, and located at a distance  $h = 4.5$  above the mirror. The  $z$ -axis is up and the  $y$ -axis is to the right. Very close to the dipole the field lines are closed loops, and just below the dipole a singularity appears.

$g$  directly below the dipole, and at the mirror surface) and all field lines more or less bend at the mirror as in Fig. 1.3b. To the right of the  $z$ -axis and above the dipole (not shown) the field lines are typically smooth curves without any interesting structure, although exceptions are possible. The existence of optical vortices resulting from interference

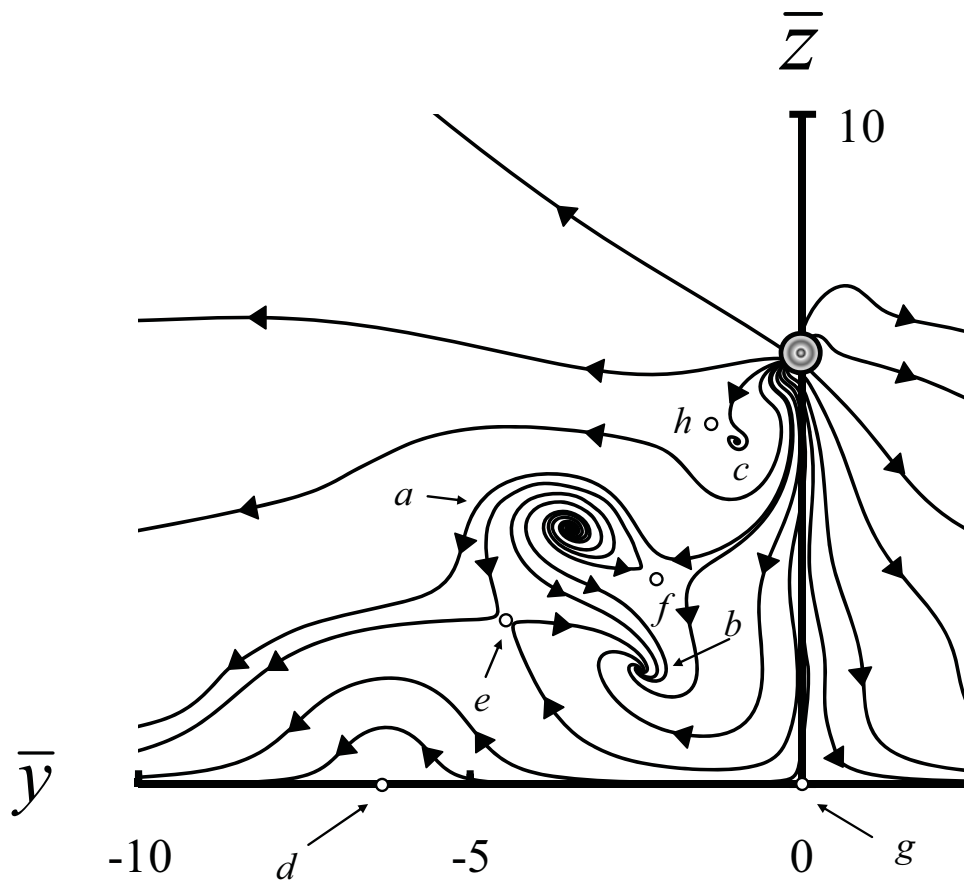


Figure 4.8 Field lines in the  $yz$ -plane.

The figure shows the field lines of the Poynting vector in the  $yz$ -plane for a dipole located at a distance of one wavelength from the mirror ( $h = 2\pi$ ), oscillating under an angle of  $45^\circ$  with the  $z$ -axis ( $\gamma = \pi/4$ ). We observe a complex flow line pattern with singularities and vortices. Points  $a$ ,  $b$  and  $c$  are optical vortices, and points  $e$ ,  $f$ ,  $g$  and  $h$  are singularities where the field lines split. Singularity  $d$  is a point on the singular circle in the  $xy$ -plane (Sec. 4.3).

between radiation and its reflection at a surface was predicted for the first time by Braunbek and Laukien for the reflection of a plane wave by the Sommerfeld half-plane [1]. The most common optical vortices are vortices in Laguerre-Gaussian laser beams

[10-13], and their structure is related to the angular momentum carried by the beam. Another type of optical vortex is the rotation in the field lines of the Poynting vector of a multipole field [44]. These vortices are due to the emission mechanism of the source rather than interference.

Points  $a$ ,  $b$  and  $c$  in the figure are singularities at the centers of vortices, and the other named points, except for point  $d$ , are regular singularities where field lines abruptly change direction. Interestingly, there are field lines that start at vortex  $a$  and end at vortex  $b$ . These field lines represent a local energy flow where the energy does not directly originate from the location of the dipole. Field lines emanating from vortex  $a$  either end in vortex  $b$  or they run to the far field, and field lines ending at vortex  $b$  either come from vortex  $a$  or from the dipole. Other field lines coming from the dipole swing around either vortex  $a$  or  $b$  and then run to the far field. At point  $e$ , some of these field lines seem to collide, and this leads to the singularity at point  $e$ . At the singularities  $f$  and  $g$ , field lines split in two directions. An enlargement of the very small vortex at point  $c$  is shown in Fig. 4.9. Since the field lines split just above the vortex, there has to be a singularity in that region, which is point  $h$ .

For other values of the parameters a similar pattern is observed, and typically the number of singularities and vortices increases with  $h$ . An exception is  $\gamma = 0$ , for which there are no singularities, except for the point directly below the dipole, at the mirror surface. For this case of a perpendicular dipole all field lines more or less bend at the mirror as in Fig. 1.3b, and this is illustrated in Fig. 4.10. The field line pattern for a

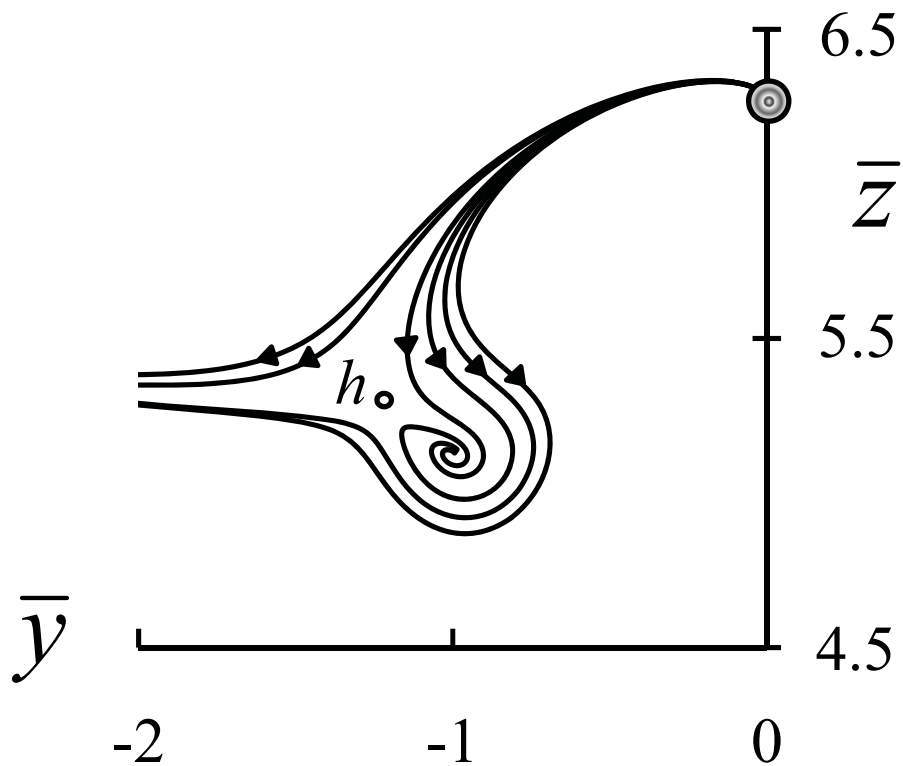


Figure 4.9 Enlargement of the vortex  $c$  of Fig. 4.8.

At the center of the vortex is a singularity, and very nearby is the singularity labeled  $h$ .

parallel dipole ( $\gamma = \pi/2$ ) is shown in Fig. 4.11, and we see that there are fewer singularities than in Fig. 4.8 where the dipole oscillates under  $45^\circ$  with the  $z$ -axis.

At a singularity the Poynting vector is zero. This can be a result of  $\mathbf{E}(\mathbf{r}) = 0$ ,  $\mathbf{B}(\mathbf{r}) = 0$  or  $\mathbf{E}(\mathbf{r}) \times \mathbf{B}(\mathbf{r})$  imaginary. Since  $\boldsymbol{\varepsilon}$  and  $\boldsymbol{\varepsilon}^{\text{im}}$  are in the  $yz$ -plane, it follows from Eq. (2.7) that  $\mathbf{B}(\mathbf{r})$  only has an  $x$ -component for a field point  $\mathbf{r}$  in the  $yz$ -plane.

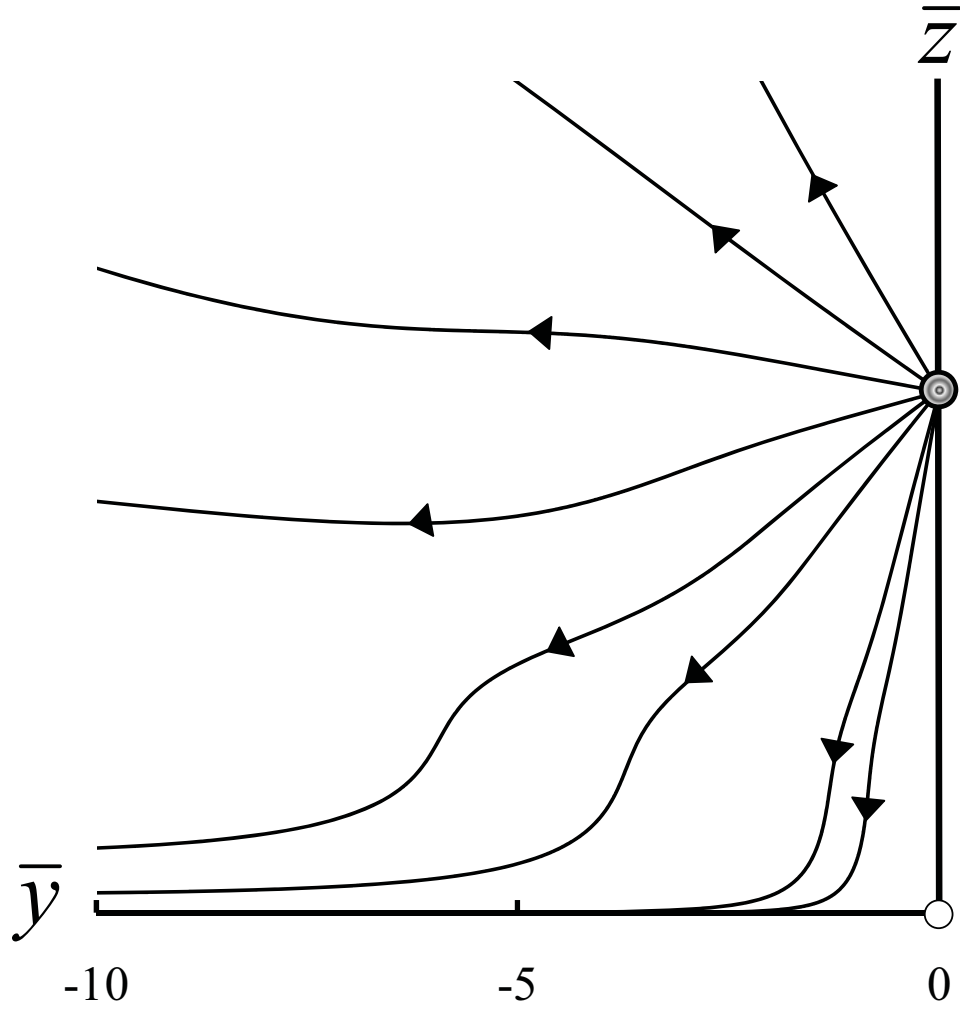


Figure 4.10 The field line pattern for a dipole oscillating perpendicular to the plane of the mirror at a distance  $h = 2\pi$ .

For this case there are no vortices and singularities, except for the point directly below the dipole at the mirror surface. The field line pattern is reflection symmetric with respect to the  $z$ -axis.

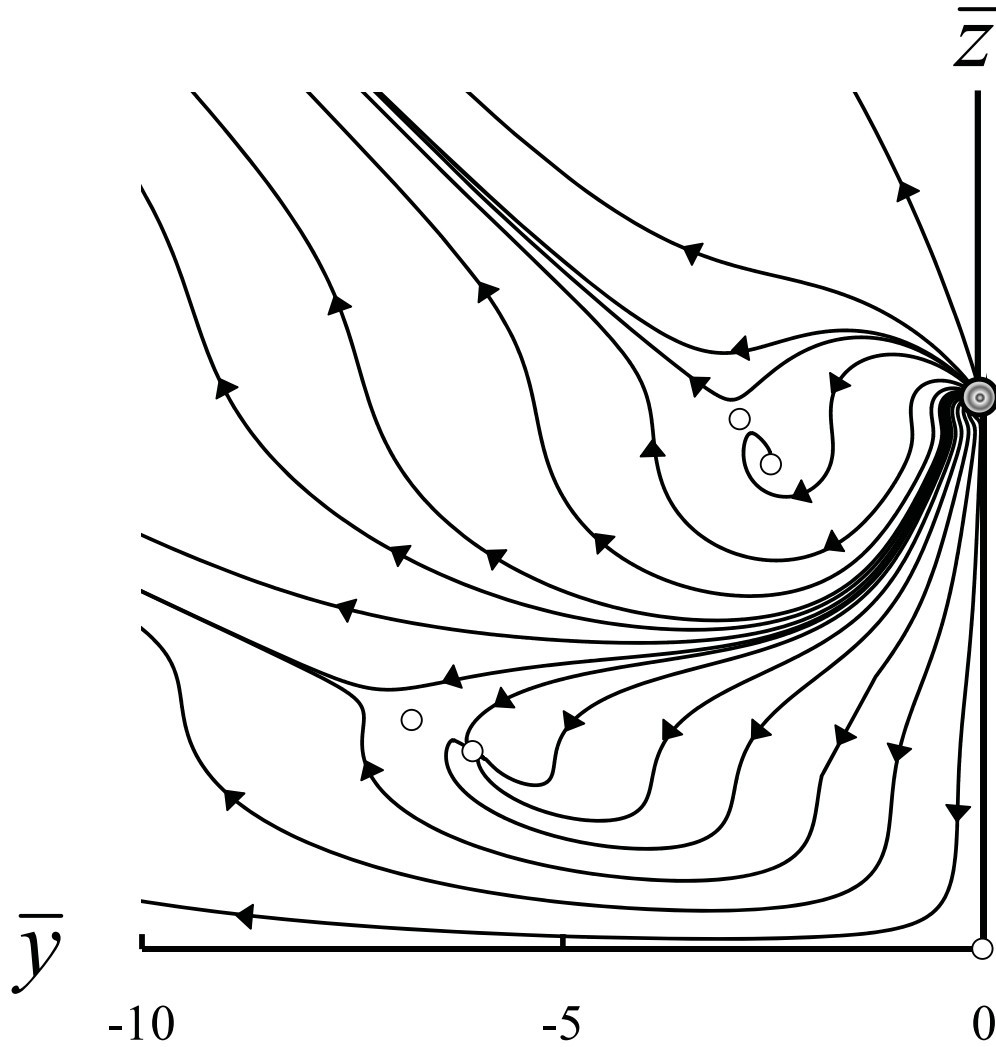


Figure 4.11 Field lines for a dipole oscillating parallel to the surface at a distance  $h = 2\pi$ .

In this graph, several singularities appear and they are indicated by little white circles. The energy flow pattern is reflection symmetric with respect to the  $z$ -axis.

The amplitude  $\mathbf{B}(\mathbf{r})$  is complex, so for  $\mathbf{B}(\mathbf{r})$  to vanish it has to hold that both the real and the imaginary parts of the  $x$ -component have to vanish simultaneously. Working out the expression for  $B_x(\mathbf{r})$  gives

$$\frac{\sin q_1 - q_1 \cos q_1}{q_1^3} [\bar{y} + (h - \bar{z}) \tan \gamma] + \frac{\sin q_2 - q_2 \cos q_2}{q_2^3} [\bar{y} + (h + \bar{z}) \tan \gamma] = 0 \quad , \quad (4.13)$$

for  $\text{Re} B_x(\mathbf{r}) = 0$  and

$$\frac{\cos q_1 + q_1 \sin q_1}{q_1^3} [\bar{y} + (h - \bar{z}) \tan \gamma] + \frac{\cos q_2 + q_2 \sin q_2}{q_2^3} [\bar{y} + (h + \bar{z}) \tan \gamma] = 0 \quad , \quad (4.14)$$

for  $\text{Im} B_x(\mathbf{r}) = 0$  , and here  $q_1 = \sqrt{\bar{y}^2 + (\bar{z} - h)^2}$  and  $q_2 = \sqrt{\bar{y}^2 + (\bar{z} + h)^2}$  . Equations (4.13) and (4.14) define two sets of curves in the  $yz$ -plane, and at any intersection the magnetic field is zero. These curves are shown in Fig. 4.12, and we see that the curves intersect at the location of the three vortices in Fig. 4.8. Therefore, the vortices are due to the disappearing of the magnetic field at these points. We have verified numerically that at the other singularities  $\mathbf{E}(\mathbf{r}) \times \mathbf{B}(\mathbf{r})^*$  is imaginary, except for point  $d$  where we have again  $\mathbf{B}(\mathbf{r}) = 0$  .

### 4.3 Field Lines in the Plane of the Mirror

Singularity  $d$  in Fig. 4.8 appears to be of a different nature than the other singularities. There is no vortex at this point, there is no splitting of the field lines, and there is no collision between field lines running in different directions, like for instance at singularity



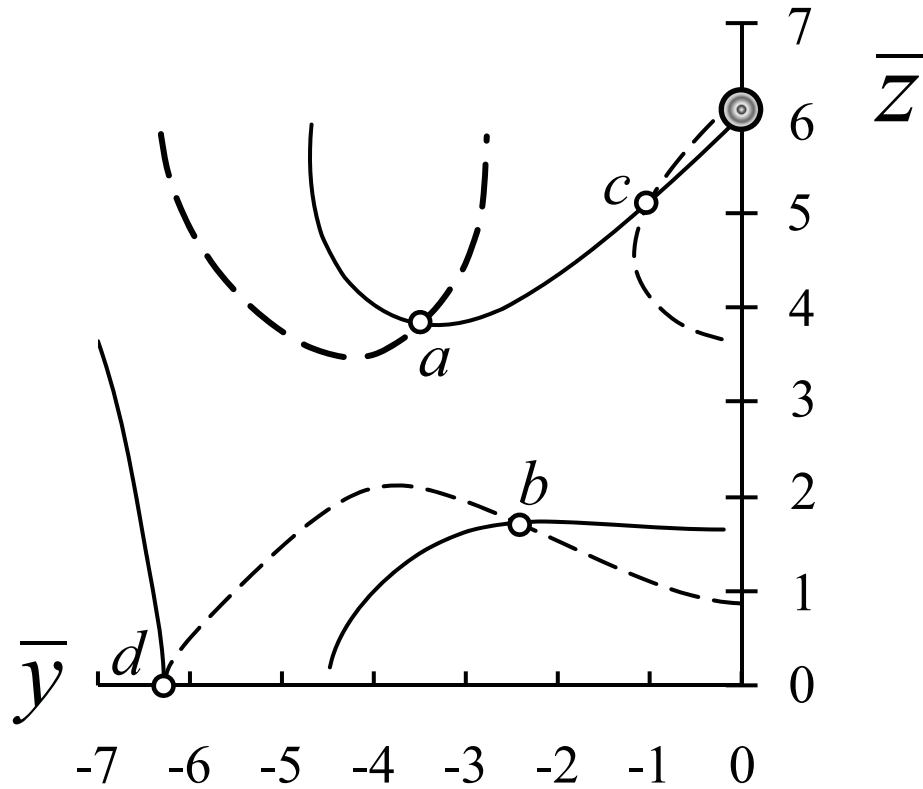


Figure 4.12 The solutions of  $\text{Re} B_x = 0$  and  $\text{Im} B_x = 0$ .

The solutions of  $\text{Re} B_x = 0$  and  $\text{Im} B_x = 0$  are the solid and dashed curves, respectively, and the parameters for this graph are the same as for Fig. 4.8. At an intersection the Poynting vector is zero, and the intersections  $a$ ,  $b$  and  $c$  correspond to the three vortices in Fig. 4.8.

*e.* Point  $d$  is in the surface of the mirror, and field lines in the neighborhood have the appearance of jumping over a bump. Singularity  $g$  in Fig 4.8 is also in the plane of the mirror, and it can be verified easily from the explicit expressions in Appendix A that  $\sigma(\mathbf{q}) = 0$  at the origin of coordinates. For a point in the plane of the mirror, the Poynting vector is in the  $xy$ -plane, and therefore field lines through any point in the mirror surface

are 2D curves in the mirror plane. In the plane of the mirror we have  $q_1 = q_2$ , and expression (A11) for  $\sigma(\mathbf{q})$  simplifies considerably. When we introduce the vector

$$\mathbf{v} = -\mathbf{e}_y h \tan \gamma \quad , \quad (4.15)$$

the Poynting vector at the point in the  $xy$ -plane with position vector  $\mathbf{q}$  can be expressed as

$$\sigma(\mathbf{q}) = \frac{4 \cos \gamma}{q_1} \left( \cos \gamma + \frac{h}{q_1} \cos \alpha \right) (\mathbf{q} - \mathbf{v}) \quad . \quad (4.16)$$

Vector  $\mathbf{v}$  represents a point on the negative  $y$ -axis (for  $\tan \gamma > 0$ ), and for  $\mathbf{q} = \mathbf{v}$  this gives  $\sigma(\mathbf{q}) = 0$ . Therefore, the singularity  $d$  in Fig. 4.8 has  $\mathbf{v}$  as position vector, and so the  $\bar{y}$ -coordinate of this point equals  $-h \tan \gamma$ . The Poynting vector is proportional to  $\mathbf{q} - \mathbf{v}$ , which is the position vector  $\mathbf{q}$  with respect to the singular point  $\mathbf{v}$ . So the Poynting vector everywhere in the  $xy$ -plane is straight out from point  $\mathbf{v}$ , and therefore the field lines are straight lines coming out of or running towards point  $\mathbf{v}$ .

With some manipulations of the expressions in Appendix A we find

$$\cos \alpha = \frac{\cos \gamma}{q_1} (\mathbf{e}_y \cdot \mathbf{q} \tan \gamma - h) \quad , \quad (4.17)$$

and combination with Eq. (4.16) yields the expression

$$\sigma(\mathbf{q}) = \frac{4 \cos^2 \gamma}{q_1^3} [\mathbf{q} \cdot (\mathbf{q} - \mathbf{v})] (\mathbf{q} - \mathbf{v}) \quad , \quad (4.18)$$

for the Poynting vector. In this form we see immediately that  $\sigma(\mathbf{q})$  vanishes at the origin of coordinates, and this is singularity  $g$  from Fig. 4.8. Furthermore, the factor  $\mathbf{q} \cdot (\mathbf{q} - \mathbf{v})$  is zero when vector  $\mathbf{q}$  is perpendicular to vector  $\mathbf{q} - \mathbf{v}$ . As can be seen most easily from Fig. 4.13, this defines a circle in the  $xy$ -plane. For any  $\mathbf{q}$  on this circle we have  $\sigma(\mathbf{q}) = 0$ , and therefore this is a singular circle. Across this circle, the Poynting vector changes sign and the field lines change direction. All field lines are straight and go through point  $\mathbf{v}$  on the  $y$ -axis. Outside the singular circle the angle between  $\mathbf{q}$  and  $\mathbf{q} - \mathbf{v}$  is less than  $90^\circ$ , so  $\mathbf{q} \cdot (\mathbf{q} - \mathbf{v}) > 0$ , and therefore  $\sigma(\mathbf{q})$  is in the outward direction. Consequently, inside the circle the field lines run from the circle towards the singularity at point  $\mathbf{v}$ , and this gives the field line picture shown in Fig. 4.14.

For a dipole oscillating along the  $z$ -axis we have  $\gamma = 0$ , and the circle shrinks to a point at the origin of coordinates. Then all field lines run radially outward from the origin. For a dipole oscillating along the  $y$ -axis we have  $\gamma \rightarrow \pi/2$ , and the radius of the circle goes to infinity. Vector  $\mathbf{v}$  becomes undefined, and this limit has to be considered more carefully. We find

$$\sigma(\mathbf{q}) = \frac{4h^2}{q_1^3} \bar{y} \mathbf{e}_y . \quad (4.19)$$

The field lines are parallel to the  $y$ -axis and the  $x$ -axis is a singular line. All field lines start at a point on the  $x$ -axis and run parallel to the  $y$ -axis to the left and the right. This is the limit of Fig. 4.14, where the circle stretches out so that it becomes the  $x$ -axis. The inside of the circle becomes the region  $y < 0$ , and all field lines run to the point  $\mathbf{v}$ , which

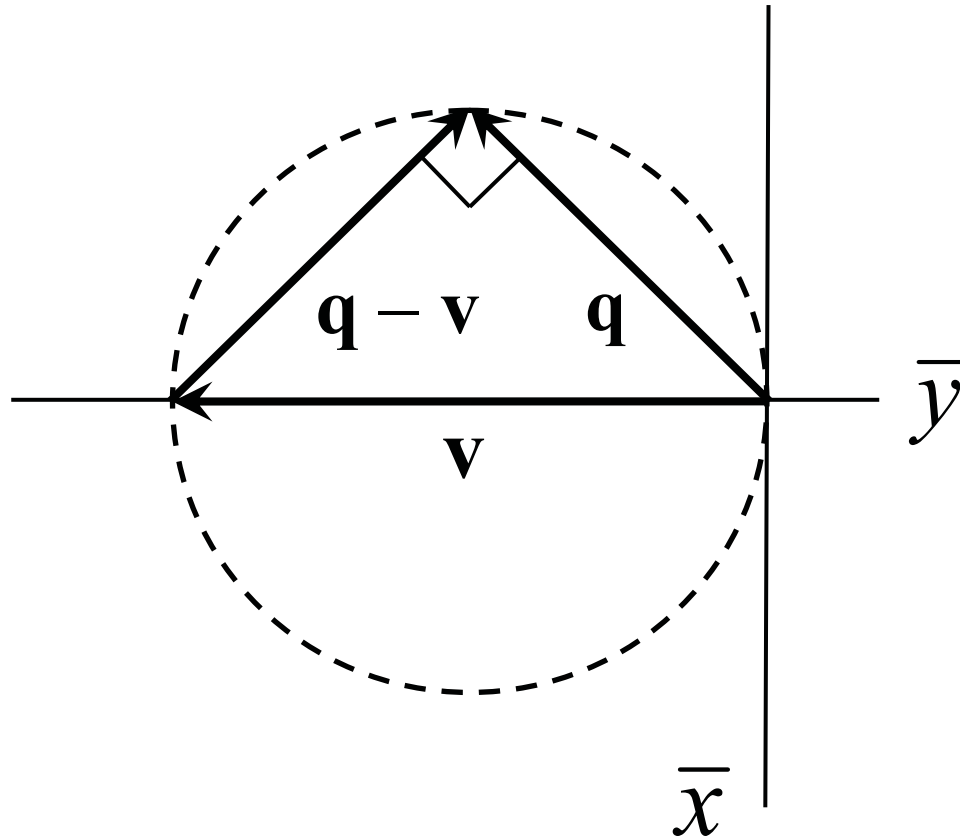


Figure 4.13 A field point in the  $xy$ -plane is represented by the position vector  $\mathbf{q}$ .

Vector  $\mathbf{v}$  is a fixed vector, directed along the  $y$ -axis, and the same field point can be represented by the position vector  $\mathbf{q} - \mathbf{v}$  with respect to the endpoint of vector  $\mathbf{v}$ . The set of all field points that satisfy the equation  $\mathbf{q} \cdot (\mathbf{q} - \mathbf{v}) = 0$  then form the shown circle, since this equation implies that the angle between  $\mathbf{q}$  and  $\mathbf{q} - \mathbf{v}$  is  $90^\circ$ .

is now at  $y = -\infty$  on the  $y$ -axis.

In summary, when an oscillating electric dipole emits radiation in the vicinity of a mirror, the pattern of energy emission is determined by interference between the electric field of the dipole and the magnetic field of the reflected radiation. The field lines of

energy flow form a set of four optical vortices, two of which are shown in Fig. 4.4. The field lines spiral around two semi-singular lines through the dipole, and these lines are oriented as shown in Fig. 4.3. Their directions are determined by angle  $\gamma$ , which is the angle between the oscillation direction of the dipole and the  $z$ -axis. The pattern is symmetric under reflection in the  $yz$ -plane. In the  $yz$ -plane, these vortices reduce to closed loops, as shown in Fig. 4.5. It is also found that for emission in the  $yz$ -plane all energy is emitted in a single direction, which is perpendicular to the dipole. This in contrast to the emission in free space, where energy is emitted in all directions. Some of the emitted energy propagates along a closed loop, and so it returns to the dipole. Since at a larger distance all energy radiates away from the source, there has to be a singular point near the dipole, as shown in Fig. 4.5. The location of this point is approximately given by Eq. (4.10). The function  $v(h)$  in this equation goes to zero with increasing  $h$ , so when the distance between the dipole and the surface of the mirror becomes larger, the singularity moves closer to the dipole, and hence the dimension of the loops becomes smaller.

Figure 4.8 shows the field line pattern in the  $yz$ -plane on a much smaller scale. We find that numerous singularities are present in the flow line pattern and there are three vortices (for the parameters in the figure). The vortices are due to the vanishing of the magnetic field at the centers of the vortices. Of particular interest is singularity  $d$  in the figure. It was shown that this singularity is a point on a singular circle in the plane of the

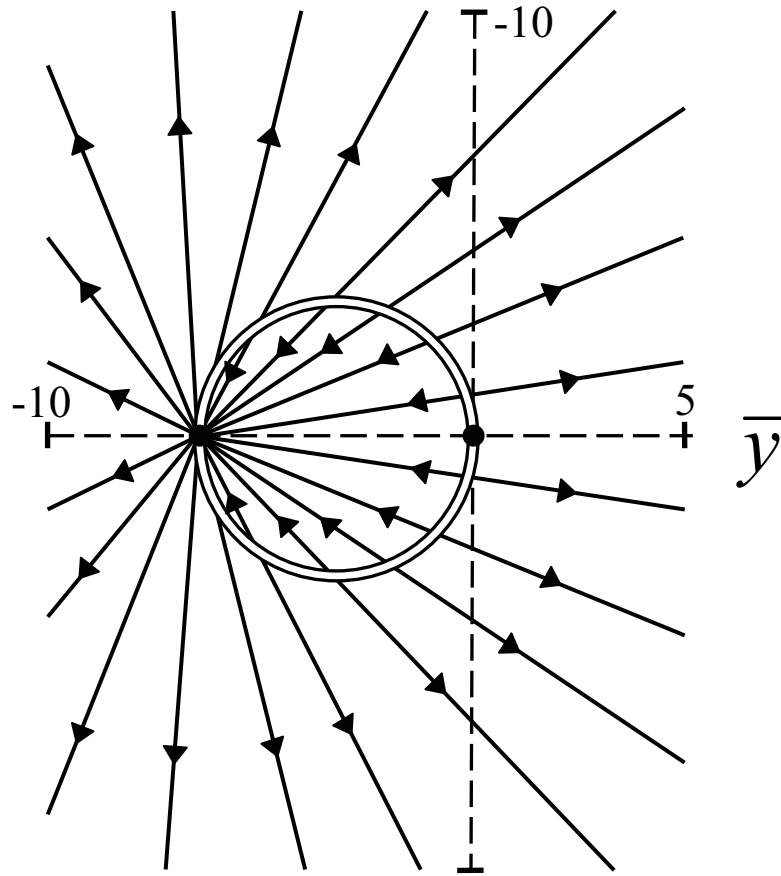


Figure 4.14 The field lines in the plane of the mirror (for  $\tan \gamma > 0$ ).

The two black dots on the  $y$ -axis are the singularities  $d$  and  $g$  from Fig. 4.8, which are located at point  $\mathbf{v}$  and the origin, respectively. In the  $xy$ -plane, these singularities appear to be the intersections of a singular circle with the  $y$ -axis. The diameter of the circle is the magnitude of vector  $\mathbf{v}$ , which is  $h|\tan \gamma|$ . When viewed from outside the circle, all field lines appear to come from the singularity at point  $\mathbf{v}$ , but inside the circle all field lines run towards the singularity. For  $\tan \gamma < 0$ , the circle is located in the region  $\bar{y} > 0$ .

mirror. Inside this circle, the field lines run from a point on the circle to singularity  $d$ , and outside the circle they run from a point on the circle to the far field, and such that the field lines appear to come from singularity  $d$ . Also, in the plane of the mirror all field lines are straight, as follows from Eq. (4.18).

When sub-wavelength resolution of the energy flow is taken into consideration, then the interference pattern between dipole radiation and its own reflection from a mirror is far from trivial. A ray diagram as in Fig. 1.3a or an educated guess as in Fig. 1.3b are not even close to the intricate pattern of energy flow that appears in this simple system. Particularly fascinating is the fact that for a linear dipole the radiation is emitted as a set of four vortices, except when the dipole oscillates exactly perpendicular to the mirror.

CHAPTER V  
DIPOLE RADIATION IN A DIELECTRIC AND A NEGATIVE INDEX OF  
REFRACTION MATERIAL

In the previous chapters we have been discussing dipole radiation in free space and near a mirror surface. Now we shall consider the energy transport of dipole radiation in a dielectric and a metamaterial with a negative index of refraction. The wave number  $k_m$  in a material with (relative) permittivity  $\epsilon_r$  and (relative) permeability  $\mu_r$  is related to the angular frequency  $\omega$  of the light by the dispersion relation  $k_m^2 = \epsilon_r \mu_r \omega^2 / c^2$ . In an ordinary dielectric we have  $\epsilon_r > 0$  and  $\mu_r > 0$ , when neglecting possible imaginary parts of  $\epsilon_r$  and  $\mu_r$ , which account for absorption, and so the wave number is  $k_m = \sqrt{\epsilon_r \mu_r} \omega / c$ . For a metal, the dielectric constant is negative in the visible region, which makes  $k_m^2$  negative and  $k_m$  imaginary. Therefore, a metal does not support propagating modes, but only evanescent modes which decay exponentially away from the surface of the material. A metamaterial is an artificially structured medium in which both  $\epsilon_r$  and  $\mu_r$  can have any value in principle. When both  $\epsilon_r$  and  $\mu_r$  are negative, the material has a negative index of refraction (see below). The wave number is again  $k_m = \sqrt{\epsilon_r \mu_r} \omega / c$ , which is real and positive. Thus such a metamaterial supports propagating modes, like a dielectric.



## 5.1 Introduction to Metamaterials

The electromagnetic response of a medium is accounted for by the (relative) permittivity  $\epsilon_r$  and the (relative) permeability  $\mu_r$ . Both  $\epsilon_r$  and  $\mu_r$  are in general complex, with a non-negative imaginary part, and they depend on the angular frequency  $\omega$  of the spectral component under consideration. The index of refraction  $n$  of the medium is a solution of

$$n^2 = \epsilon_r \mu_r \quad , \quad (5.1)$$

and for causality reasons (below) we should take the solution with

$$\text{Im}(n) \geq 0 \quad . \quad (5.2)$$

For a dielectric,  $\epsilon_r$  is approximately real and positive,  $\mu_r \approx 1$ , and the index of refraction is  $n = \sqrt{\epsilon_r \mu_r}$ , which is positive, apart from a very small positive imaginary part. For a metal with  $\omega$  below the plasmon frequency, the real part of  $\epsilon_r$  is negative, the imaginary part of  $\epsilon_r$  is small, and  $\mu_r \approx 1$ . Therefore,  $n$  is approximately positive imaginary. Paramagnetic materials have a permeability larger than unity, and for diamagnetic materials we have  $0 < \mu_r < 1$ . Media with a negative permeability do not occur naturally, or in man-made chemical compounds.

Metamaterials are artificially structured composites, consisting of arrays of sub-wavelength structures, and their electromagnetic response may not be determined only by the material from which they are constructed, but also by the geometry of the design. The typical size of a unit cell of such a composite is well below the wavelength of the radiation under consideration, and this justifies the description of the material as a

continuum with permittivity  $\epsilon_r$  and permeability  $\mu_r$ . Of particular interest are metamaterials for which the real parts of both  $\epsilon_r$  and  $\mu_r$  are negative and the imaginary parts of both are small, at a given frequency  $\omega$ . It then follows from Eqs. (5.1) and (5.2) that the real part of the index of refraction  $n$  is negative, and such materials are called negative index of refraction materials, or NIM's for short.

In the first experimental demonstration of a negative index of refraction structure [45,46], the composite consisted of split-ring resonators, to obtain a negative  $\mu_r$ , and a grid of thin metal wires, needed to lower the plasma frequency to the desired range. It was shown that this composite has a negative index of refraction in the microwave range of the electromagnetic spectrum. Many variations in the design structure of the composites have been studied, with attempts to manipulate either the plasma frequency of the permittivity of the metal or the permeability of the split-ring resonators [47-57]. After the successful proof-of-concept demonstrations of the experimental feasibility of constructing a NIM in the microwave region, the quest was on to design composites that operate in the visible region of the spectrum. The design with the split-ring resonators does not scale down to smaller wavelengths, due to increase of loss. New nanostructured materials have been developed, and negative index of refraction has been reported in the THz and near-infrared regions [58-66]. In 2005, the first NIM operating at optical wavelengths was reported [67,68]. The latest designs involve metal-dielectric nanostructures with unit cell widths as small as 10 nm, lattices with coated dielectric

spheres, or composites with nanoclusters or nanowires [69-73]. At the present state-of-the-art, loss in the material seems to be the main issue to be addressed in future designs.

## 5.2 Negative Index of Refraction Materials

We shall consider time-harmonic fields, oscillating at angular frequency  $\omega$ . The electric field can then be written as

$$\mathbf{E}(\mathbf{r}, t) = \text{Re}[\mathbf{E}(\mathbf{r})e^{-i\omega t}] , \quad (5.3)$$

with  $\mathbf{E}(\mathbf{r})$  the complex amplitude, and the magnetic field  $\mathbf{B}(\mathbf{r})$  can be represented similarly. The time-averaged Poynting vector is defined as

$$\mathbf{S}(\mathbf{r}) = \text{Re}\left[\frac{1}{2\mu}\mathbf{E}(\mathbf{r})^* \times \mathbf{B}(\mathbf{r})\right] , \quad (5.4)$$

with  $\mu = \mu_0\mu_r$ , and electromagnetic energy flows along the field lines of this vector field. When both  $\epsilon_r$  and  $\mu_r$  are negative, the material is transparent, just like an ordinary dielectric, and Maxwell's equations admit traveling plane-wave solutions. When  $\mathbf{k}_m$  is the wave vector of the plane wave, it can be shown easily that in such a material (NIM) the Poynting vector is directed opposite to the wave vector. With the time dependence as in Eq. (5.3), the phase velocity of the wave is into the direction of the wave vector  $\mathbf{k}_m$ . Therefore, the phase velocity is opposite to the direction of energy propagation, and such materials are said to have a negative phase velocity. This possibility was shown for the first time by Sivukhin [74]. Mandel'shtam [75] showed that this property has interesting consequences when an incident plane wave refracts at an interface with a NIM. Figure

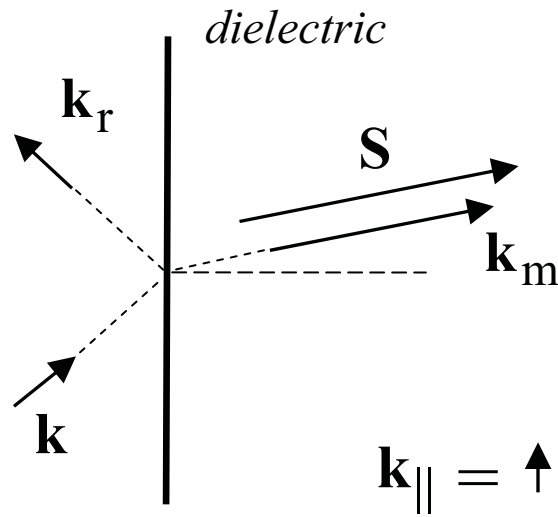


Figure 5.1 A plane wave with wave vector  $\mathbf{k}$  is incident upon an interface.

The wave partially reflects and partially transmits into the material. Due to the boundary conditions at the interface, the wave vectors of all waves must have the same parallel component  $\mathbf{k}_{||}$  with respect to the interface. For transmission into a dielectric, this gives the familiar picture shown here.

5.1 shows the refraction for an ordinary dielectric, and Fig. 5.2 illustrates refraction into a material with negative  $\epsilon_r$  and  $\mu_r$ , e.g., a NIM. The parallel components of all wave vectors have to be the same, due to the boundary conditions. In the NIM, the energy propagates against the wave vector, and since the energy transport has to be away from the interface, the wave vector  $\mathbf{k}_m$  of the refracted wave must be as shown in Fig. 5.2. Consequently, the direction of energy propagation in the negative index of refraction material is into the direction indicated by the Poynting vector  $\mathbf{S}$  in the figure. As compared to Fig. 5.1, the light bends to the other side of the normal to the interface.

Many other unusual properties have been predicted for NIM's, such as an inverse Doppler shift and Cerenkov effect [76]. A historical account of negative index of

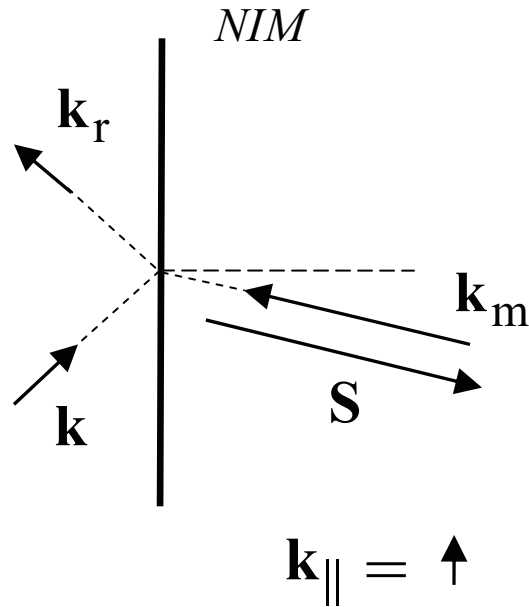


Figure 5.2 The same plane wave incident upon a NIM.

In a NIM, the energy propagates against the wave vector, and therefore the wave vector  $\mathbf{k}_m$  in the medium must be as shown here. As a result, the propagation direction of the energy, indicated by the Poynting vector  $\mathbf{S}$ , of the transmitted wave is at the opposite side of the surface normal, as compared to refraction into a dielectric.

refraction (and negative group velocity) can be found in [77]. A particularly interesting feature of a NIM is that it has the ability to focus radiation from a point source, as shown by Veselago [78] When radiation is incident upon a slab of negative index of refraction material, as shown in Fig. 5.3, then at the first interface the rays refract as in Fig. 5.2, and upon exiting the layer at the second interface, the rays are transmitted at the opposite side of the normal, as compared to the similar situation for a dielectric. As a result, a ray

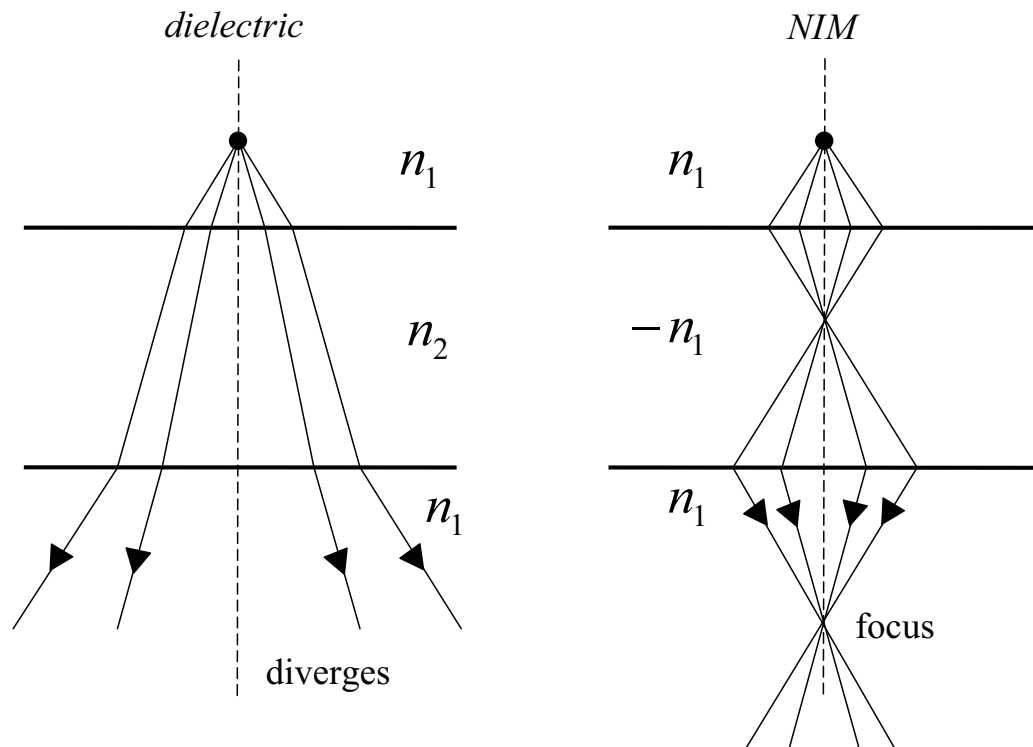


Figure 5.3 Light from a point source is incident upon a layer of dielectric material (left) and a ray diagram for a slab of NIM (right).

The rays emerge as diverging below the material for a dielectric, as shown in the diagram on the left. When the index of refraction of the NIM is the opposite of the index of refraction of the surrounding dielectric, the rays focus to a point, as show in the diagram on the right.

coming from the source crosses the optical axis as shown, whereas for a dielectric layer of material, the rays diverge away from the axis. When the index of refraction of the NIM is the opposite of the index of refraction of the medium outside the layer (usually vacuum or air, so  $n_1 = 1$ ), then all rays go through the same point below the medium, and hence there is a focal point which represents the image of the source. In this sense, a

layer of metamaterial behaves like a lens, provided there is a perfect index matching with the dielectric above and below.

It was shown by Pendry in 2000 [79] that a layer of negative index of refraction material has the ability to amplify the evanescent waves upon transiting the layer. Therefore, the evanescent waves will contribute to the image at the focal point, provided this point is at a sub-wavelength distance from the second interface. In principle, it may therefore be possible to obtain an image with sub-wavelength resolution. A perfect index matching is required, so the index of refraction of the NIM should be -1 (if surrounded by vacuum). After the publication of this landmark paper, such a layer of negative index of refraction material has become known as a superlens.

In this chapter we shall demonstrate another peculiar property of energy transport in a NIM. When a small (compared to a wavelength) particle is embedded in a dielectric and irradiated by a circularly-polarized laser beam, the induced electric dipole moment is a vector which rotates in a plane perpendicular to the propagation direction of the beam (taken to be the  $z$ -axis). The field lines of the Poynting vector of the emitted electric dipole radiation are curves which swirl around the  $z$ -axis and each field line lies on a cone. The field lines form a vortex pattern, and two typical field lines are shown in Fig. 5.4. We shall show that when the particle is embedded in a material with negative  $\epsilon_r$  and  $\mu_r$ , the field lines of energy flow of the same rotating dipole moment wind again around the  $z$ -axis and each field line lies on a cone, but the direction of rotation around the  $z$ -axis is

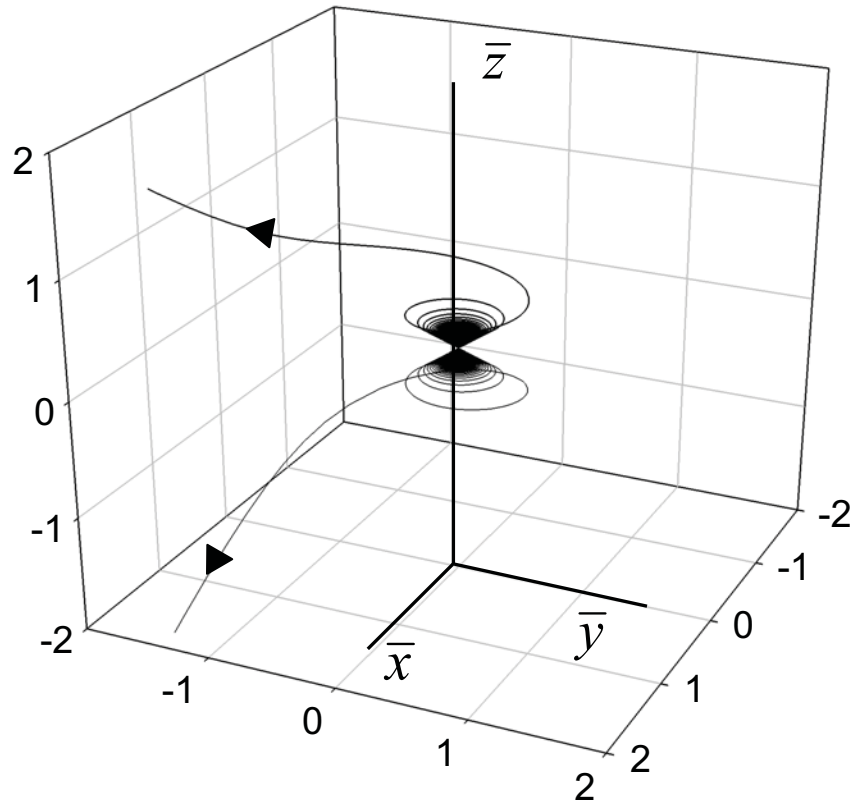


Figure 5.4 Two field lines of the Poynting vector for the radiation emitted by a rotating dipole moment embedded in a dielectric.

We use dimensionless variables  $x = k_0 x$ ,  $y = k_0 y$  and  $z = k_0 z$ , so that 2 corresponds to one wavelength. The  $x$  and  $y$  axes have been lowered to improve the view. The direction of rotation of the dipole moment is counterclockwise when viewed down the positive  $z$ -axis. The field lines swirl around the  $z$ -axis while remaining on a cone. The direction of rotation of the field lines is the same as the direction of rotation of the dipole moment.



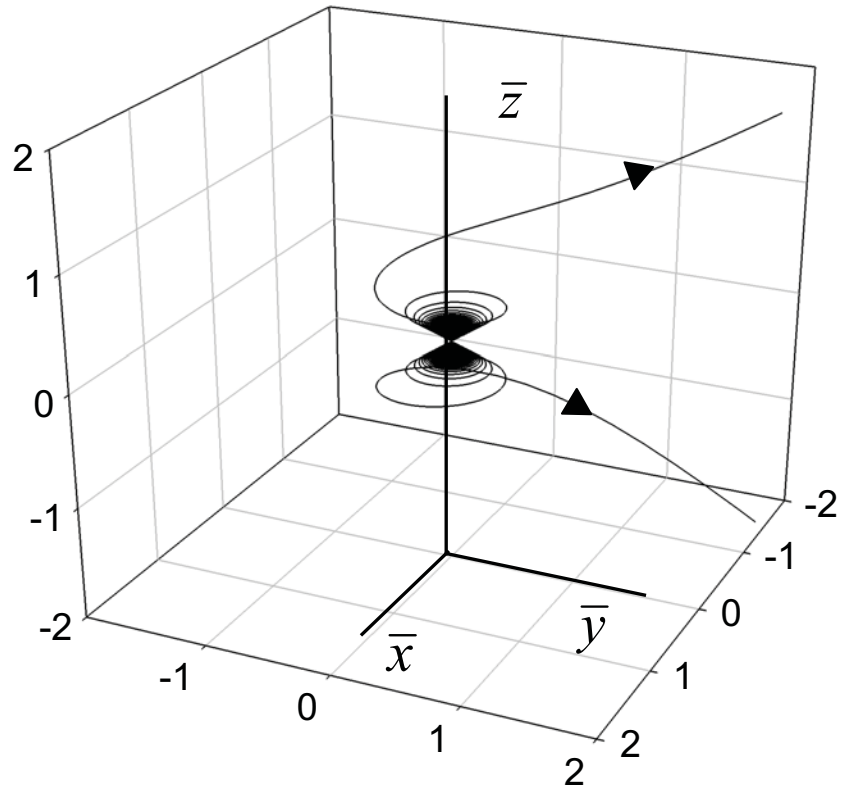


Figure 5.5 Energy flow field lines for emission of radiation by a particle embedded in a NIM.

The direction of rotation of the field lines around the  $z$ -axis is reversed, as compared to the rotation of the field lines in Fig. 5.4.

reversed as compared to the field lines for emission in a dielectric. This feature is shown in Fig. 5.5.

### 5.3 Green's Function and the Index of Refraction

The electric and magnetic fields of the radiation emitted by a particle embedded in an infinite medium with permittivity  $\epsilon_T$  and permeability  $\mu_T$  are solutions of Maxwell's equations. These solutions can be expressed in terms of the Green's function  $g(\mathbf{r})$  for the scalar Helmholtz equation. This function is the solution of

$$(\nabla^2 + n^2 k_0^2)g(\mathbf{r}) = -4\pi\delta(\mathbf{r}) \quad , \quad (5.5)$$

with  $k_0 = \omega/c$  and  $n^2$  is given by Eq. (5.1). A solution of Eq. (5.5) is

$$g(\mathbf{r}) = \frac{e^{ink_0 r}}{r} \quad . \quad (5.6)$$

This solution involves the index of refraction  $n$ . However, Eq. (5.1) only determines  $n^2$ , given  $\epsilon_T$  and  $\mu_T$ , and this leaves an ambiguity for the choice of  $n$ . In general,  $\epsilon_T$  and  $\mu_T$  are complex, and therefore also  $n$  and  $n^2$  are complex. The two solutions of Eq. (5.1) differ by a minus sign, and are each others reflection in the origin of the complex plane. The Green's function represents a spherical wave, centered at the origin of coordinates, and causality requires that such a wave cannot grow exponentially in amplitude with increasing  $r$ . It then follows from (5.6) that we need to take the solution  $n$  for which  $\text{Im}(n) \geq 0$ . A moment of thought then shows that this still leaves an ambiguity for the choice of  $n$  when the product  $\epsilon_T \mu_T$  is positive. Causality requires that the imaginary

parts of  $\varepsilon_r$  and  $\mu_r$  are non-negative, and we then see that we can only have  $\varepsilon_r\mu_r > 0$  if  $\varepsilon_r$  and  $\mu_r$  are both positive or both negative. In order to resolve this ambiguity, we note that both  $\varepsilon_r$  and  $\mu_r$  will still have a very small positive imaginary part, representing damping in the material. By taking the limit where these imaginary parts vanish, we find that for  $\varepsilon_r\mu_r > 0$  the solution of Eq. (5.1) should be taken as

$$n = \sqrt{\varepsilon_r\mu_r} \quad , \quad \varepsilon_r \text{ and } \mu_r \text{ positive (dielectric)} \quad , \quad (5.7)$$

$$n = -\sqrt{\varepsilon_r\mu_r} \quad , \quad \varepsilon_r \text{ and } \mu_r \text{ negative (NIM)} \quad . \quad (5.8)$$

When a time dependence as in Eq. (5.3) is considered, the Green's function leads to spherical waves of the form  $\exp[i(nk_0r - \omega t)]/r$ . For a dielectric we have  $n > 0$ , and such a wave is an outgoing wave with phase velocity  $c/n$ . For  $\text{Re}(n) < 0$  this is an incoming wave rather than an outgoing wave and therefore the phase velocity is inward, or negative. This situation is reminiscent of the case for a plane wave, as shown in Fig. 5.2, where the energy propagates against the wave vector.

#### 5.4 Electric Dipole Radiation

The induced electric dipole moment of a particle can be written as

$$\mathbf{d}(t) = \text{Re}(\mathbf{d}e^{-i\omega t}) \quad , \quad (5.9)$$

with  $\mathbf{d}$  the complex amplitude. When this dipole is located at the origin of coordinates, the complex amplitude of the current density is  $\mathbf{j}(\mathbf{r}) = -i\omega \mathbf{d}\delta(\mathbf{r})$ , and the solution of

Maxwell's equations for the radiation field emitted by this dipole, embedded in a medium, can be represented as

$$\mathbf{E}(\mathbf{r}) = \mu_r \frac{k_0^2}{4\pi\epsilon_0} \left[ \mathbf{d}g(\mathbf{r}) + \frac{1}{n^2 k_0^2} (\mathbf{d} \cdot \nabla) \nabla g(\mathbf{r}) \right], \quad (5.10)$$

$$\mathbf{B}(\mathbf{r}) = \frac{i\omega\mu}{4\pi} \mathbf{d} \times \nabla g(\mathbf{r}), \quad (5.11)$$

in terms of the Green's function  $g(\mathbf{r})$ . With expression (5.6) for  $g(\mathbf{r})$  the derivatives of the Green's function can be worked out, and this yields

$$\mathbf{E}(\mathbf{r}) = \mu_r \frac{k_0^2}{4\pi\epsilon_0} \left\{ \mathbf{d} - (\hat{\mathbf{r}} \cdot \mathbf{d}) \hat{\mathbf{r}} + [\mathbf{d} - 3(\hat{\mathbf{r}} \cdot \mathbf{d}) \hat{\mathbf{r}}] \frac{i}{nk_0 r} \left( 1 + \frac{i}{nk_0 r} \right) \right\} g(\mathbf{r}), \quad (5.12)$$

$$\mathbf{B}(\mathbf{r}) = \frac{n\mu_r}{c} \frac{k_0^2}{4\pi\epsilon_0} (\hat{\mathbf{r}} \times \mathbf{d}) \left( 1 + \frac{i}{nk_0 r} \right) g(\mathbf{r}). \quad (5.13)$$

With expressions (5.12) and (5.13) for the electric and magnetic field amplitudes, the Poynting vector  $\mathbf{S}(\mathbf{r})$  can be constructed. Let us first consider the far field, for which  $k_0 r \gg 1$ . Then only the  $O(1/r)$  terms in  $\mathbf{E}(\mathbf{r})$  and  $\mathbf{B}(\mathbf{r})$  survive, and we obtain

$$\mathbf{S}(\mathbf{r}) \approx \hat{\mathbf{r}} |\mu_r|^2 \frac{ck_0^4}{32\pi^2 \epsilon_0 r^2} e^{-2k_0 r \text{Im} n} [\mathbf{d}^* \cdot \mathbf{d} - (\hat{\mathbf{r}} \cdot \mathbf{d}^*)(\hat{\mathbf{r}} \cdot \mathbf{d})] \text{Re} \left( \frac{n}{\mu_r} \right). \quad (5.14)$$

In the far field, the Poynting vector is proportional to  $\hat{\mathbf{r}}$ . It can be shown from the discussion above that [80]

$$\operatorname{Re}\left(\frac{n}{\mu_r}\right) \geq 0, \quad (5.15)$$

and since every other term on the right-hand side of Eq. (5.14) is positive, it follows that the power flow is in the radially outward direction in the far field. For a material with  $\operatorname{Re}(n) < 0$  the electric and magnetic fields are spherical incoming waves, but the power flow is in the outward direction, as expected.

### 5.5 The Poynting Vector for a Dielectric and a NIM

The expression for the Poynting vector for arbitrary  $\epsilon_r$  and  $\mu_r$  is cumbersome, so here we shall only give the result relevant to the present topic. These are the cases shown in Eqs. (5.7) and (5.8). For  $\epsilon_r$ ,  $\mu_r$  and  $n$  positive we have a dielectric and for  $\epsilon_r$ ,  $\mu_r$  and  $n$  negative we have a NIM. We set  $\mathbf{d} = d_0 \mathbf{u}$ , with  $\mathbf{u} \cdot \mathbf{u}^* = 1$ , for the dipole moment, and we introduce  $q = k_0 r$  as the dimensionless distance between the dipole and the field point  $\mathbf{r}$ . The Poynting vector then becomes

$$\mathbf{S}(\mathbf{r}) = \frac{3P_0}{8\pi r^2} \left\{ \mu_r n [1 - (\hat{\mathbf{r}} \cdot \mathbf{u}^*)(\hat{\mathbf{r}} \cdot \mathbf{u})] \hat{\mathbf{r}} + \frac{2\mu_r}{q} \left( 1 + \frac{1}{n^2 q^2} \right) \operatorname{Im}(\hat{\mathbf{r}} \cdot \mathbf{u}^*) \mathbf{u} \right\}, \quad (5.16)$$

where

$$P_0 = \frac{ck_0^4 d_0^2}{12\pi\epsilon_0}, \quad (5.17)$$

equals the power emitted by the dipole in free space.

When  $\mathbf{u}$  is real we have a linear dipole oscillating back and forth along the vector  $\mathbf{u}$ , as can be seen from Eq. (5.9). Then  $\operatorname{Im}(\hat{\mathbf{r}} \cdot \mathbf{u}^*) \mathbf{u} = 0$ , and  $\mathbf{S}(\mathbf{r})$  is in the radial outward

direction (since  $\mu_r n > 0$  for both cases). The field lines of  $\mathbf{S}(\mathbf{r})$  are straight lines coming out of the dipole. We now consider the more interesting case of a rotating dipole moment.

When we take

$$\mathbf{u} = -\frac{1}{\sqrt{2}}(\mathbf{e}_x + i\mathbf{e}_y) , \quad (5.18)$$

then it can be verified from Eq. (5.9) that  $\mathbf{d}(t)$  is a vector which rotates counterclockwise in the  $xy$ -plane, when viewed down the  $z$ -axis. The Poynting vector becomes

$$\mathbf{S}(\mathbf{r}) = \frac{3P_0}{8\pi r^2} \left[ \mu_r n \left(1 - \frac{1}{2} \sin^2 \theta\right) \hat{\mathbf{r}} + \left(1 + \frac{1}{n^2 q^2}\right) \frac{\mu_r \sin \theta}{q} \mathbf{e}_\phi \right] , \quad (5.19)$$

with  $\theta$  the polar angle with the  $z$ -axis, and  $\mathbf{e}_\phi$  is the unit vector into the direction of increasing  $\phi$  (angle around the  $z$ -axis in the counterclockwise direction). Apart from the radial component, the Poynting vector now has a contribution proportional to  $\mathbf{e}_\phi$ , and this gives a rotation of the field lines around the  $z$ -axis. For a dielectric we have  $\mu_r > 0$ , and this rotation is in the counterclockwise direction, which is the same orientation as the rotation of the dipole moment. For a negative index of refraction material we have  $\mu_r < 0$ , and the field lines swirl around the  $z$ -axis in the opposite direction as the rotation direction of the dipole moment. Figures 3 and 4 show two field lines each for this rotating dipole moment.

## 5.6 Conclusions

The complex amplitudes of the electric and magnetic fields for the radiation emitted by an electric dipole embedded in a medium with arbitrary values of  $\epsilon_r$  and  $\mu_r$  are given by Eqs. (5.12) and (5.13). The Poynting vector can then be obtained by substitution of these expressions into the right-hand side of Eq. (5.4). For the case where both  $\epsilon_r$  and  $\mu_r$  are positive (dielectric) or where both are negative (NIM), the result is given by Eq. (5.16). For a linear dipole the field lines of  $\mathbf{S}(\mathbf{r})$  are straight lines, coming out of the dipole. When the embedding medium is a material with negative  $\epsilon_r$  and  $\mu_r$ , the spherical waves are incoming, whereas the energy flow is outward. This is very similar to the case of a plane wave, as shown in Fig. 5.2, where the direction of energy flow is opposite to the wave vector. For a rotating dipole moment embedded in a material with negative  $\epsilon_r$  and  $\mu_r$ , we found that the direction of rotation of the field lines around the  $z$ -axis is opposite to the direction of rotation of the dipole moment, whereas for a dielectric both the field lines and the dipole moment have the same orientation in their rotation.

## CHAPTER VI

### CONCLUSIONS AND FUTURE WORK

#### 6.1 Conclusions

In its most general state of oscillation, an electric dipole moment of a source of radiation traces out an ellipse in a plane, taken to be the  $xy$ -plane. The field lines of the Poynting vector of the emitted electromagnetic field represent the direction of energy flow, and we have obtained an analytical solution for these field lines. It was found that for a given observation direction in the far field, the corresponding field line lies entirely on the cone specified by the polar angle. Near the location of the dipole the field lines have a vortex structure, in which each field line swirls around the  $z$ -axis numerous times. In the far field, each field line approaches asymptotically a straight line, resembling an optical ray. This line does not go through the origin of coordinates, where the dipole is located, and therefore it appears that the position of the dipole in the  $xy$ -plane is shifted. We have calculated this displacement in  $xy$ -plane. To observe indirectly the existence of the vortex in the near field, we consider the intensity distribution in the far field, and we anticipate that the displacement of the field lines due to the vortex in the near field will yield a shift of the intensity profile in the far field. This intensity shift has a macroscopic effect, when considering the difference profile, and this can be observed in the far field.



Both numerical simulations and experimental results of the macroscopic effect observed in the far field are presented.

When a linearly oscillating dipole is located in the vicinity of a mirror, the pattern of energy emission (energy flow in the near field) is determined by interference between the electric field of the dipole and the magnetic field of the reflected radiation and the emission of radiation is drastically altered as compared to the emission by a dipole in free space. Close to the dipole, the energy is emitted as a set of four optical vortices. At a larger distance from the dipole, singularities and isolated vortices appear. Also, in the plane of the mirror a singular circle appears.

For a rotating dipole moment embedded in a material with negative index of refraction, we found that the direction of rotation of the field lines around the z-axis is opposite to the direction of rotation of the dipole moment, whereas for a dielectric both the field lines and the dipole moment have the same orientation in their rotation.

## 6.2 Future Work

In the future we intend to extend our research to biomedical applications. We plan to disperse gold nano-particles inside a liposome, which contains a drug for therapy. Then we can track the drug and manipulate its temperature through selective heating of the nano-particles by microwave irradiation. As a first step we shall embed the nano-particles in a tissue mimicking material as show in Fig. 6.1. The system will be exposed to an external microwave field, and we shall consider various microwave generator

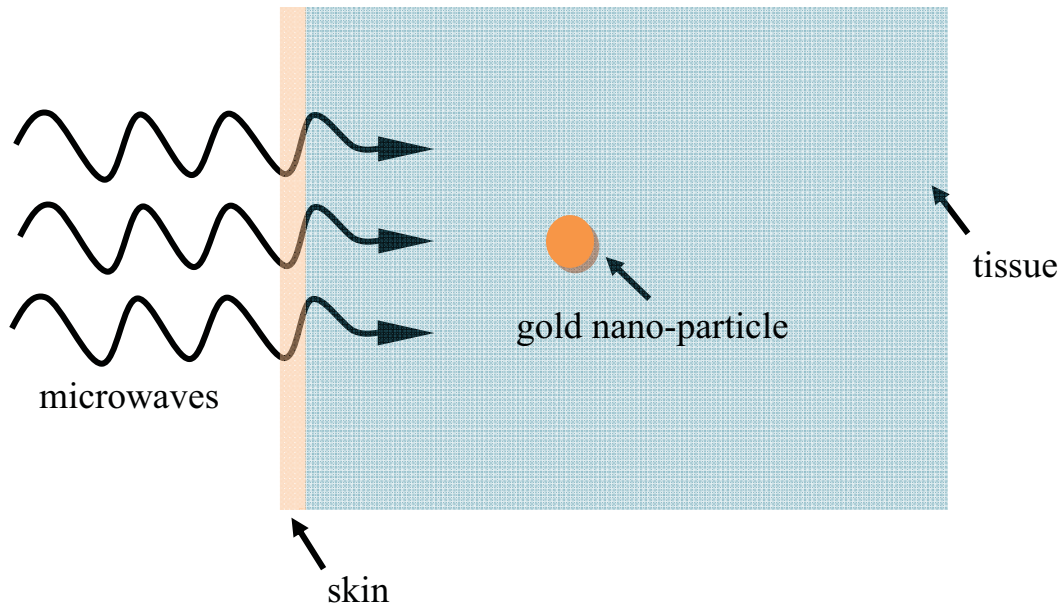


Figure 6.1 Gold nano-particle embedded in tissue and exposed to external microwaves.

power outputs. The incident microwaves will induce a current density in the nano-particle, and this current density will heat up the particle through Ohmic loss. Through phonon-phonon interactions at the interface between the particle and the tissue, the nano-particle will transfer heat to the tissue. The heat generated by the nano-particles can then be used to affect the surrounding material, for instance to destroy tumor cells. Theoretical calculations will be conducted to better understand the heating process of the nano-particles and the effects on the surrounding tissue.

## REFERENCES

- [1] W. Braunbek and G. Laukien, Einzelheiten zur Halbebenen Beugung, *Optik* 9 (1952) 174-179.
- [2] J. F. Nye and M. V. Berry, Dislocations in wave trains, *Proc. Roy. Soc. Lond. A* 336 (1974) 165-190.
- [3] H. F. Schouten, T. D. Visser, G. Gbur, D. Lenstra and H. Blok, Creation and annihilation of phase singularities near a sub-wavelength slit, *Opt. Exp.* 11 (2003) 371-380.
- [4] H. F. Schouten, T. D. Visser, D. Lenstra and H. Blok, Light transmission through a sub-wavelength slit: Waveguiding and optical vortices, *Phys. Rev. E* 67 (2003) 036608 1-4.
- [5] J. Masajada and B. Dubik, Optical vortex generation by three plane wave interference, *Opt. Commun.* 198 (2001) 21-27.
- [6] B. Richards and E. Wolf, Electromagnetic diffraction in optical systems II. Structure of the image field in an aplanatic system, *Proc. Roy. Soc. Lond. A* 253 (1959) 358-379.
- [7] A. Boivin, J. Dow and E. Wolf, Energy flow in the neighborhood of the focus of a coherent beam, *J. Opt. Soc. Am.* 57 (1967) 1171-1175.
- [8] G. P. Karman, M. W. Beijersbergen, A. van Duijl and J. P. Woerdman, Creation and annihilation of phase singularities in a focal field, *Opt. Lett.* 22 (1997) 1503-1505.
- [9] J. T. Foley and E. Wolf, Wave-front spacing in the focal region of high-numerical aperture systems, *Opt. Lett.* 30 (2005) 1312-1314.
- [10] M. Vasnetsov and K. Staliunas (Eds.), *Optical Vortices, Horizons in World Physics*, Vol. 228, Nova Science, Commack, New York (1999).
- [11] A. V. Volyar, V. G. Shvedov and T. A. Fadeeva, The structure of a nonparaxial gaussian beam near the focus: II. Optical vortices, *Opt. Spectrosc.* 90 (2001) 93-100.

- [12] V. A. Pas'co, M. S. Soskin and M. V. Vasnetsov, Transversal optical vortex, *Opt. Commun.* 198 (2001) 49-56.
- [13] A. V. Volyar, T. A. Fadeeva and V. G. Shvedov, Optical vortex generation and Jones vector formalism, *Opt. Spectrosc.* 93 (2002) 267-272.
- [14] J. Leach, M. R. Dennis, J. Courtial and M. J. Padgett, Vortex knots in light, *New Journal of Physics* 7 (2005) 55-65.
- [15] G. Molina-Terriza, L. Torner and D. V. Petrov, Vortex streets in walking parametric wave mixing, *Opt. Lett.* 24 (1999) 899-901.
- [16] I. Freund, Poincaré vortices, *Opt. Lett.* 26 (2001) 1996-1998.
- [17] I. Freund, A. I. Mokhun, M. S. Soskin, O. V. Angelsky and I. I. Mokhun, Stokes singularity relations, *Opt. Lett.* 27 (2002) 545-547.
- [18] V. G. Denisenko, A. Minovich, A. S. Desyatnikov, W. Krolikowski, M. S. Soskin and Y. S. Kivshar, Mapping phases of singular scalar light fields, *Opt. Lett.* 33 (2008) 89-91.
- [19] J. D. Jackson, *Classical Electrodynamics*, 3rd ed., Wiley, New York (1998) p. 411.
- [20] M. Born and E. Wolf, *Principles of Optics*, 6th ed., Pergamon, Oxford (1980) Chapter 3.
- [21] H. F. Arnoldus and J. T. Foley, The dipole vortex, *Opt. Commun.* 231 (2004) 115-128.
- [22] K. G. Lee, H. W. Kihm, J. E. Kihm, W. J. Choi, H. Kim, C. Ropers, D. J. Park, Y. C. Yoon, S. B. Choi, D. H. Woo, J. Kim, B. Lee, Q. H. Park, C. Lienau and D. S. Kim, Vector field microscopic imaging of light, *Nature Photonics* 1 (2007) 53-56.
- [23] Y. Ohdaira, T. Inoue, H. Hori and K. Kitahara, Local circular polarization observed in surface vortices of optical near-fields, *Opt. Exp.* 16 (2008) 2915-2921.
- [24] D. Courjon, *Near-Field Microscopy and Near-Field Optics*, Imperial College Press, London (2003).
- [25] F. Zenhausern, Y. Martin and H. K. Wickramasinghe, Scanning interferometric apertureless microscopy: Optical imaging at 10 Angstrom resolution, *Science* 269 (1995) 1083-1085.

- [26] Z. H. Kim and S. R. Leone, High-resolution apertureless near-field optical imaging using gold nanosphere probes, *J. Phys. Chem. B* 110 (2006) 19804-19809.
- [27] A. J. Devaney and E. Wolf, New representations for multipole moments and angular spectrum amplitudes of electromagnetic fields, *Opt. Commun.* 9 (1973) 327-330.
- [28] J. Gasper, G. C. Sherman and J. J. Stamnes, Reflection and refraction of an arbitrary electromagnetic wave at a plane interface, *J. Opt. Soc. Am.* 66 (1976) 955-960.
- [29] G. W. Ford and W. H. Weber, Electromagnetic effects on a molecule at a metal surface, *Surf. Sci.* 109 (1981) 451-481.
- [30] G. W. Ford and W. H. Weber, Electromagnetic interactions of molecules with metal surfaces, *Phys. Rep.* 113 (1984) 195-287.
- [31] L. Mandel and E. Wolf, *Optical Coherence and Quantum Optics*, Cambridge University Press, Cambridge (1995) p. 120.
- [32] T. Setälä and M. Kaivola, Decomposition of the point-dipole field into homogeneous and evanescent parts, *Phys. Rev. E* 59 (1999) 1200-1206.
- [33] H. F. Arnoldus and J. T. Foley, Uniform asymptotic approximation of the evanescent part of the Green's tensor, *Opt. Commun.* 207 (2002) 7-15.
- [34] H. F. Arnoldus and J. T. Foley, Spatial separation of the traveling and evanescent parts of dipole radiation, *Opt. Lett.* 28 (2003) 1299-1301.
- [35] H. F. Arnoldus and J. T. Foley, Traveling and evanescent parts of the optical near field, *J. Mod. Opt.* 50 (2003) 1883-1901.
- [36] H. F. Arnoldus, Evanescent waves in the near and the far field, *Advances in Imaging and Electron Physics*, Vol. 132, Ed. P. W. Hawkes, Elsevier Academic Press, New York (2004) p 1-67.
- [37] H. F. Arnoldus and J. T. Foley, Transmission of dipole radiation through interfaces and the phenomenon of anti-critical angles, *J. Opt. Soc. Am. A* 21 (2004) 1109-1117.
- [38] H. F. Arnoldus, Angular spectrum representation of the electromagnetic multipole fields, and their reflection at a perfect conductor, *Surf. Sci.* 590 (2005) 101-116.
- [39] I. V. Lindell, *Methods for Electromagnetic Field Analysis*, Oxford University Press, Oxford (1992) Sec. 1.4.

- [40] L. Mandel and E. Wolf, *Optical Coherence and Quantum Optics*, Cambridge University Press, Cambridge (1995) p. 469.
- [41] D. Haefner, S. Sukhov and A. Dogariu, Spin-Hall effect of light in spherical geometry, *Phys. Rev. Lett.* 102 (2009) 123903 1-4.
- [42] H. F. Arnoldus, Reflection off a mirror, *J. Mod. Opt.* 54 (2007) 45-66.
- [43] S. Maeda and P. Diamant, Power flow between adjacent electric dipoles, *IEEE Ant. Prop.* 44 (2002) 68-76.
- [44] H. F. Arnoldus, Vortices in multipole radiation, *Opt. Commun.* 252 (2005) 253-261.
- [45] D. R. Smith, W. J. Padilla, D. C. Vier, S. C. Nemat-Nasser and S. Schultz, Composite medium with simultaneously negative permeability and permittivity, *Phys. Rev. Lett.* 84 (2000) 4184-4187.
- [46] R. A. Shelby, D. R. Smith and S. Schultz, Experimental verification of a negative index of refraction, *Science* 292 (2001) 77-79.
- [47] J. B. Pendry, A. J. Holden, D. J. Robbins and W. J. Steward, Low frequency plasmons in thin-wire structures, *J. Phys.: Condens. Matter* 10 (1998) 4785-4809.
- [48] J. B. Pendry, A. J. Holden, D. J. Robbins and W. J. Steward, Low frequency plasmons in thin-wire structures, *J. Phys.: Condens. Matter* 10 (1998) 4785-4809.
- [49] J. B. Pendry, A. J. Holden, D. J. Robbins and W. J. Steward, Magnetism from conductors and enhanced nonlinear phenomena, *IEEE Trans. Microwave Th. and Tech.* 47 (1999) 2075-2084.
- [50] C. G. Parazolli, R. B. Gregor, K. Li, B. E. C. Koltenbah and M. Tanielian, Experimental verification and simulation of negative index of refraction using Snell's law, *Phys. Rev. Lett.* 90 (2003) 107401 1-4.
- [51] A. A. Houck, J. B. Brock and I. L. Chang, Experimental observations of a left-handed material that obeys Snell's law, *Phys. Rev. Lett.* 90 (2003) 137401 1-4.
- [52] J. D. Baena, R. Marqués and F. Medina, Artificial magnetic metamaterial design by using spiral resonators, *Phys. Rev. B* 69 (2004) 014402 1-5.

- [53] T. J. Yen, W. J. Padilla, N. Fang, D. C. Vier, D. R. Smith, J. B. Pendry, D. N. Basov and X. Zhang, Terahertz magnetic response from artificial materials, *Science* 303 (2004) 1494-1496.
- [54] S. Linden, C. Enkrich, M. Wegener, J. Zhou, T. Koschny and C. M. Soukoulis, Magnetic response of metamaterials at 100 Terahertz, *Science* 306 (2004) 1351-1353.
- [55] I. Bulu, H. Caglayan and E. Ozbay, Experimental demonstration of labyrinth-based left-handed metamaterials, *Opt. Exp.* 13 (2005) 10238-10247.
- [56] E. Ekmekci, K. Topalli, T. Akin and G. Turhan-Sayan, A tunable multi-band metamaterial design using micro-split SRR structures, *Opt. Exp.* 17 (2009) 16046-16058.
- [57] Y. Yuan, B-I. Popa and S. A. Cummer, Zero loss magnetic metamaterials using powered active unit cells, *Opt. Exp.* 17 (2009) 16135-16143.
- [58] S. Zhang, W. Fan, B. K. Minhas, A. Frauenglass, K. J. Malloy and S. R. J. Brueck, Midinfrared resonant magnetic nanostructures exhibiting a negative permeability, *Phys. Rev. Lett.* 94 (2005) 037402 1-4.
- [59] G. Dolling, C. Enkrich, M. Wegener, J. F. Zhou, C. M. Soukoulis and S. Linden, Cut-wire pairs and plate pairs as magnetic atoms for optical metamaterials, *Opt. Lett.* 30 (2005) 3198-3200.
- [60] W. J. Padilla, A. J. Taylor, C. Highstrete, M. Lee and R. D. Averitt, Dynamical electric and magnetic metamaterial response at terahertz frequencies, *Phys. Rev. Lett.* 96 (2006) 107401 1-4.
- [61] G. Dolling, C. Enkrich, M. Wegener, C. M. Soukoulis and S. Linden, Low-loss negative-index metamaterial at telecommunication wavelengths, *Opt. Lett.* 31 (2006) 1800-1802.
- [62] M. S. Wheeler, J. S. Aitchison and M. Mojahedi, Coated nonmagnetic spheres with a negative index of refraction at infrared frequencies, *Phys. Rev. B* 73 (2006) 045105 1-7.
- [63] E. Kim, Y. R. Shen, W. Wu, E. Ponizovskaya, Z. Yu, A. M. Bratkovsky, S-Y. Wang and R. S. Williams, Modulation of negative index metamaterials in the near-IR range, *Appl. Phys. Lett.* 91 (2007) 173105 1-3.

- [64] L. Menon, W. T. Lu, A. L. Friedman, S. P. Bennett, D. Heiman and S. Sridhar, Negative index metamaterials based on metal-dielectric nanocomposites for imaging applications, *Appl. Phys. Lett.* 93 (2008) 123117 1-3.
- [65] J. Valentine, S. Zhang, T. Zentgraf, E. Ulin-Avila, D. A. Genov, G. Bartal and X. Zhang, Three-dimensional optical metamaterial with a negative refractive index, *Nature* 455 (2008) 376-380.
- [66] D. Ö. Güney, T. Koschny, M. Kafesaki and C. M. Soukoulis, Connected bulk negative index photonic metamaterials, *Opt. Lett.* 34 (2009) 506-508.
- [67] V. M. Shalaev, W. Cai, U. K. Chettiar, H-K. Yuan, A. K. Sarychev, V. P. Drachev and A. V. Kildishev, Negative index of refraction in optical metamaterials, *Opt. Lett.* 30 (2005) 3356-3358.
- [68] S. Zhang, W. Fan, N. C. Panoiu, K. J. Malloy, R. M. Osgood and S. R. J. Brueck, Experimental demonstration of near-infrared negative-index metamaterials, *Phys. Rev. Lett.* 95 (2005) 137404 1-4.
- [69] C. Enkrich, M. Wegener, S. Linden, S. Burger, L. Zschiedrich, F. Schmidt, J. F. Zhou, Th. Koschny and C. M. Soukoulis, Magnetic metamaterials at telecommunication and visible frequencies, *Phys. Rev. Lett.* 95 (2005) 203901 1-4.
- [70] G. Dolling, M. Wegener, C. M. Soukoulis and S. Linden, Negative-index metamaterial at 780 nm wavelength, *Opt. Lett.* 32 (2007) 53-55.
- [71] U. K. Chettiar, A. V. Kildishev, H-K. Yuan, W. Cai, S. Xiao, V. P. Drachev and V. M. Shalaev, Dual-band negative index metamaterial: double negative at 813 nm and single negative at 772 nm, *Opt. Lett.* 32 (2007) 1671-1673.
- [72] J. Yao, Z. Liu, Y. Liu, Y. Wang, C. Sun, G. Bartal, A. M. Stacy and X. Zhang, Optical negative refraction in bulk metamaterials of nanowires, *Science* 321 (2008) 930.
- [73] Q. Wu and W. Park, Negative index materials based on nanoclusters, *Appl. Phys. Lett.* 92 (2008) 153114 1-3.
- [74] D. V. Sivukhin, The energy of electromagnetic fields in dispersive media, *Opt. Spectrosc.* 3 (1957) 308-312.
- [75] L. I. Mandel'shtam, Group velocity in a crystal lattice, *Zh. Exp. Teor. Fiz.* 15 (1945) 475-478.



- [76] V. E. Pafomov, Transition radiation and Cerenkov radiation, Sov. Phys. JETP 36 (1959) 1321-1324.
- [77] V. M. Agranovich and Y. N. Gartstein, Spatial dispersion and negative refraction of light, Phys. Uspekhi 49 (2006) 1029-1044.
- [78] V. G. Veselago, The electrodynamics of substances with simultaneously negative values of  $\epsilon$  and  $\mu$ , Sov. Phys. Uspekhi 10 (1968) 509-514.
- [79] J. B. Pendry, Negative refraction makes a perfect lens, Phys. Rev. Lett. 85 (2000) 3966-3969.
- [80] M. W. McCall, A. Lakhtakia and W. S. Weiglhofer, The negative index of refraction demystified, Eur. J. Phys. 23 (2002) 353-359.

## APPENDIX A

### CALCULATION OF THE POYNTING VECTOR FOR A DIPOLE LOCATED AT A DISTANCE H ABOVE A MIRROR

The Poynting vector for electric dipole radiation near a mirror can be evaluated explicitly, as outlined in Chapter 4. In terms of the parameters

$$a = \boldsymbol{\varepsilon} \cdot \hat{\mathbf{q}}_1 , \quad (\text{A1})$$

$$a' = \boldsymbol{\varepsilon}^{\text{im}} \cdot \hat{\mathbf{q}}_1 , \quad (\text{A2})$$

$$b = \boldsymbol{\varepsilon}^{\text{im}} \cdot \hat{\mathbf{q}}_2 , \quad (\text{A3})$$

$$b' = \boldsymbol{\varepsilon} \cdot \hat{\mathbf{q}}_2 , \quad (\text{A4})$$

$$c = \hat{\mathbf{q}}_1 \cdot \hat{\mathbf{q}}_2 , \quad (\text{A5})$$

$$c' = \boldsymbol{\varepsilon} \cdot \boldsymbol{\varepsilon}^{\text{im}} , \quad (\text{A6})$$

and the functions

$$f_1 = \left[ 1 - \frac{i}{q_1} \left( 1 - \frac{i}{q_1} \right) \right] \left( 1 + \frac{i}{q_2} \right) , \quad (\text{A7})$$

$$g_1 = \left[ 1 - \frac{3i}{q_1} \left( 1 - \frac{i}{q_1} \right) \right] \left( 1 + \frac{i}{q_2} \right) , \quad (\text{A8})$$

$$f_2 = \left[ 1 + \frac{i}{q_2} \left( 1 + \frac{i}{q_2} \right) \right] \left( 1 - \frac{i}{q_1} \right) , \quad (\text{A9})$$

$$g_2 = \left[ 1 + \frac{3i}{q_2} \left( 1 + \frac{i}{q_2} \right) \right] \left( 1 - \frac{i}{q_1} \right) , \quad (\text{A10})$$

the Poynting vector takes the form

$$\boldsymbol{\sigma}(\mathbf{q}) = (1 - a^2) \hat{\mathbf{q}}_1 + \left( \frac{q_1}{q_2} \right)^2 (1 - b^2) \hat{\mathbf{q}}_2 + \frac{q_1}{q_2} \text{Re} [ e^{i(q_2 - q_1)} \mathbf{Z} ] , \quad (\text{A11})$$

with

$$\mathbf{Z} = (c'\hat{\mathbf{q}}_2 - b'\boldsymbol{\varepsilon}^{\text{im}})f_1 + a(c\boldsymbol{\varepsilon}^{\text{im}} - a'\hat{\mathbf{q}}_2)g_1 + (c'\hat{\mathbf{q}}_1 - a'\boldsymbol{\varepsilon})f_2 + b(c\boldsymbol{\varepsilon} - b'\hat{\mathbf{q}}_1)g_2 . \quad (\text{A12})$$

The first term on the right-hand side of Eq. (A11), proportional to  $\hat{\mathbf{q}}_1$ , is the Poynting vector for a free dipole (no mirror) and the second term, proportional to  $\hat{\mathbf{q}}_2$ , would be the Poynting vector of the mirror dipole, if it were a free dipole. The third term in Eq. (A11) is the interference term, involving cross terms between the source field and the reflected field.

The parameters given by Eqs. (A1)-(A6) can be worked out further by using the expressions Eqs. (4.1) and (4.2) for  $\boldsymbol{\varepsilon}$  and  $\boldsymbol{\varepsilon}^{\text{im}}$ , respectively. In terms of the polar angles  $(\theta_1, \phi)$  with respect to the position of the dipole (Fig. 4.2), we have

$$\hat{\mathbf{q}}_1 = \mathbf{e}_\rho \sin \theta_1 + \mathbf{e}_z \cos \theta_1 , \quad (\text{A13})$$

where

$$\mathbf{e}_\rho = \mathbf{e}_x \cos \phi + \mathbf{e}_y \sin \phi \quad (\text{A14})$$

is the radial unit vector in the  $xy$ -plane, and it can be seen from Fig. 4.2 that

$$\hat{\mathbf{q}}_2 = \frac{q_1}{q_2} \left( \hat{\mathbf{q}}_1 + \mathbf{e}_z \frac{2h}{q_1} \right) , \quad (\text{A15})$$

with  $h = k_0 H$ . We then obtain

$$a = \sin \theta_1 \sin \phi \sin \gamma + \cos \theta_1 \cos \gamma , \quad (\text{A16})$$

$$a' = -\sin \theta_1 \sin \phi \sin \gamma + \cos \theta_1 \cos \gamma , \quad (\text{A17})$$

$$b = \frac{1}{q_2} (a' q_1 + 2h \cos \gamma) , \quad (\text{A18})$$

$$b' = \frac{1}{q_2}(aq_1 + 2h \cos \gamma) \quad , \quad (\text{A19})$$

$$c = \frac{1}{q_2}(q_1 + 2h \cos \theta_1) \quad , \quad (\text{A20})$$

$$c' = \cos(2\gamma) \quad . \quad (\text{A21})$$

From Eq. (A1) it follows that we also have  $a = \cos \alpha$  , with  $\alpha$  the angle between  $\boldsymbol{\varepsilon}$  and  $\hat{\mathbf{q}}_1$  .

## APPENDIX B

### NUMERICAL ASPECTS OF THE COMPUTATION OF FIELD LINES

The Poynting vector  $\mathbf{S}(\mathbf{r})$  is a vector field in space. A field line of this vector field is a curve, represented as  $\mathbf{r}(u)$ , with  $u$  a dummy parameter. For each value of  $u$ ,  $\mathbf{r}(u)$  is a point on the curve, and at this point the vector  $\mathbf{S}(\mathbf{r})$  is on the tangent line of the curve. Therefore, the field lines  $\mathbf{r}(u)$  are a solution of

$$\frac{d\mathbf{r}(u)}{du} = \mathbf{S}(\mathbf{r}(u)) \quad . \quad (\text{B1})$$

The field lines are only determined by the direction of  $\mathbf{S}(\mathbf{r})$ , and not its magnitude, and therefore the vector fields  $\mathbf{S}(\mathbf{r})$  and  $f(\mathbf{r})\mathbf{S}(\mathbf{r})$ , with  $f(\mathbf{r})$  any positive function, have the same field lines. We then adopt dimensionless coordinates, such that  $2\pi$  corresponds to one optical wavelength. So we set  $\mathbf{q} = k_0\mathbf{r}$  for the dimensionless position vector of a point, and a field line is now represented as  $\mathbf{q}(u)$ . Overall positive constants can be absorbed in the function  $f(\mathbf{r})$ , like the factor  $(2\mu_0)^{-1}$  in the definition of the Poynting vector (Eq. (2.10)). The complex amplitudes of the electric and magnetic fields also have overall constants, as can be seen from Eqs. (2.6) and (2.7) for the fields of an electric dipole in free space. We set

$$\mathbf{E}(\mathbf{r}) = \frac{k_0^3 d_0}{4\pi\epsilon_0} \mathbf{e}(\mathbf{r}) \quad , \quad (\text{B2})$$

$$\mathbf{B}(\mathbf{r}) = \frac{k_0^3 d_0}{4\pi\epsilon_0 c} \mathbf{b}(\mathbf{r}) \quad , \quad (\text{B3})$$

so that  $\mathbf{e}(\mathbf{r})$  and  $\mathbf{b}(\mathbf{r})$  are dimensionless. The parameter  $d_0$  is defined in Eq. (2.16).

The equation for the field lines in dimensionless coordinates then becomes

$$\frac{d\mathbf{q}}{du} = a(\mathbf{q}) \text{Re}[\mathbf{e}(\mathbf{q}) \times \mathbf{b}(\mathbf{q})^*] \quad , \quad (\text{B4})$$

with  $a(\mathbf{q})$  an arbitrary positive function. On the right-hand side of Eq. (B4) we consider  $\mathbf{e}$  and  $\mathbf{b}$  functions of  $\mathbf{q}$  rather than  $\mathbf{r}$ , in obvious notation.

The solutions of Eq. (B4) are curves  $\mathbf{q}(u)$ . Only one field line goes through any point in space, since field lines can not cross, and therefore when we choose a point  $\mathbf{q}_0$ , a unique solutions  $\mathbf{q}(u)$  goes through this point. We call this the initial point, and we set  $u = 0$  at this point. So, given  $\mathbf{q}(0) = \mathbf{q}_0$ , Eq. (B4) determines the field line through this point. Field lines have an orientation; they run into the same direction as the Poynting vector on the tangent line. It follows from Eq. (B1) that the direction of a field line is in the direction of increasing  $u$ . Equation (B4) can be integrated from  $u = 0$  to both positive and negative values of  $u$ , and then the direction of the field line is into the direction of the solution with positive  $u$ .

In Sec. (2.4), the field lines of the Poynting vector for a free dipole were obtained analytically by solving Eq. (B4) in spherical coordinates. The field lines of the Poynting vector for dipole radiation near a mirror (Ch. 4) have to be computed numerically by solving Eq. (B4). It appears to be advantageous to use Cartesian coordinates, rather than spherical coordinates. We use dimensionless coordinates  $(\bar{x}, \bar{y}, \bar{z}, )$ , in terms of which a field point is represented as

$$\mathbf{q} = \bar{x}\mathbf{e}_x + \bar{y}\mathbf{e}_y + \bar{z}\mathbf{e}_z . \quad (\text{B5})$$

The Cartesian components of Eq. (B4) are

$$\frac{d\bar{x}}{du} = a(\mathbf{q})\mathbf{e}_x \cdot \text{Re}[\mathbf{e}(\mathbf{q}) \times \mathbf{b}(\mathbf{q})^*] , \quad (\text{B6})$$



$$\frac{d\bar{y}}{du} = a(\mathbf{q})\mathbf{e}_y \cdot \text{Re}[\mathbf{e}(\mathbf{q}) \times \mathbf{b}(\mathbf{q})^*] , \quad (\text{B7})$$

$$\frac{d\bar{z}}{du} = a(\mathbf{q})\mathbf{e}_z \cdot \text{Re}[\mathbf{e}(\mathbf{q}) \times \mathbf{b}(\mathbf{q})^*] , \quad (\text{B8})$$

and this set has to be solved for the functions  $\bar{x}(u)$ ,  $\bar{y}(u)$  and  $\bar{z}(u)$ , given the initial point  $(\bar{x}_0, \bar{y}_0, \bar{z}_0)$ . In the *Mathematica* program below, the right-hand sides of these equations are computed from  $\mathbf{e}(\mathbf{q})$  and  $\mathbf{b}(\mathbf{q})$ , and not by computing  $\text{Re}[\mathbf{e}(\mathbf{q}) \times \mathbf{b}(\mathbf{q})^*]$  first by hand, as in Appendix A.

The function  $a(\mathbf{q})$  is an arbitrary positive function of  $\mathbf{q}$ , or  $\bar{x}$ ,  $\bar{y}$  and  $\bar{z}$ . We may simply set  $a(\mathbf{q}) = 1$ , but better choices are possible. The field of the dipole diverges when approaching the dipole, with  $\mathbf{e}(\mathbf{q})$  diverging as  $1/q_1^3$  and  $\mathbf{b}(\mathbf{q})$  as  $1/q_1^2$  (here,  $q_1$  is the dimensionless distance to the dipole). The corresponding Poynting vector diverges as  $1/q_1^5$  in general for an elliptical dipole. For a linear dipole this becomes  $1/q_1^2$  due to a cancellation of terms. This divergence may lead to numerical problems when integrating the set (B6)-(B8). By making an appropriate choice for the function  $a(\mathbf{q})$ , this divergence may be eliminated from the right-hand side of the three equations. We take the function  $a(\mathbf{q})$  as

$$a(\mathbf{q}) = q_1^n = \left( \sqrt{\bar{x}^2 + \bar{y}^2 + (\bar{z} - h)^2} \right)^n , \quad (\text{B9})$$

and in the Sample Program below we have set  $n = 2$ . The choice of the value of  $n$  affects the numerical step size  $\Delta u$ , which is determined by *Mathematica*, and it is a matter of trial and error to find out which value of  $n$  is most optimum.

The Sample Program below computes the upper-right field line in Fig. 4.4, and the Test Run Output shows the graph that *Mathematica* generates. The graph has been rotated in order to give it more or less the same view as in Fig. 4.4. After running the program, the graph data is exported and put in a *SigmaPlot* (or *Excel*) spreadsheet. For graphs with multiple field lines, this procedure has to be repeated for each field line. Then a graph is made in *SigmaPlot* and fixed up (choose orientation, remove grid lines, change axes fonts, etc.), after which it is copied to *Word*. In *Word*, the axes, axes labels, arrow heads and any other embellishments are put in, to arrive at the final publication-quality graph.

## Sample Program:

```

In[91]:=

Clear;
Clear[x];
Clear[y];
Clear[z];

Assumptions -> Element[{x, y, z}, Reals]

h = 2 Pi;
γ = Pi / 4;
d1 = {0, Sin[γ], Cos[γ]};
d2 = {0, -Sin[γ], Cos[γ]};
rhat1 = {
   $\frac{x[u]}{\sqrt{x[u]^2 + y[u]^2 + (z[u] - h)^2}}$ ,  $\frac{y[u]}{\sqrt{x[u]^2 + y[u]^2 + (z[u] - h)^2}}$ ,  $\frac{z[u] - h}{\sqrt{x[u]^2 + y[u]^2 + (z[u] - h)^2}}$ 
};
rhat2 = {
   $\frac{x[u]}{\sqrt{x[u]^2 + y[u]^2 + (z[u] + h)^2}}$ ,  $\frac{y[u]}{\sqrt{x[u]^2 + y[u]^2 + (z[u] + h)^2}}$ ,  $\frac{z[u] + h}{\sqrt{x[u]^2 + y[u]^2 + (z[u] + h)^2}}$ 
};

ef1 =  $\frac{1}{\sqrt{x[u]^2 + y[u]^2 + (z[u] - h)^2}}$  *
  (d1 - (d1.rhat1) rhat1 +  $\frac{1}{\sqrt{x[u]^2 + y[u]^2 + (z[u] - h)^2}}$  (  $\frac{1}{\sqrt{x[u]^2 + y[u]^2 + (z[u] - h)^2}$  - I ) * (3 (d1.rhat1) rhat1 - d1) ) *
  Ei*sqrt(x[u]^2+y[u]^2+(z[u]-h)^2);
ef2 =  $\frac{1}{\sqrt{x[u]^2 + y[u]^2 + (z[u] + h)^2}}$  *
  (d2 - (d2.rhat2) rhat2 +  $\frac{1}{\sqrt{x[u]^2 + y[u]^2 + (z[u] + h)^2}}$  (  $\frac{1}{\sqrt{x[u]^2 + y[u]^2 + (z[u] + h)^2}$  - I ) * (3 (d2.rhat2) rhat2 - d2) ) *
  Ei*sqrt(x[u]^2+y[u]^2+(z[u]+h)^2);

bf1 =  $\frac{1}{\sqrt{x[u]^2 + y[u]^2 + (z[u] - h)^2}}$  * (1 +  $\frac{I}{\sqrt{x[u]^2 + y[u]^2 + (z[u] - h)^2}}$ ) * Cross[rhat1, d1] Ei*sqrt(x[u]^2+y[u]^2+(z[u]-h)^2);
bf2 =  $\frac{1}{\sqrt{x[u]^2 + y[u]^2 + (z[u] + h)^2}}$  * (1 +  $\frac{I}{\sqrt{x[u]^2 + y[u]^2 + (z[u] + h)^2}}$ ) * Cross[rhat2, d2] Ei*sqrt(x[u]^2+y[u]^2+(z[u]+h)^2);

ef = ef1 + ef2;
bf = bf1 + bf2;
Refine[s = N[Re[Cross[ef, Conjugate[bf]]]], Assumptions -> Element[{x[u], y[u], z[u]}, Reals]];

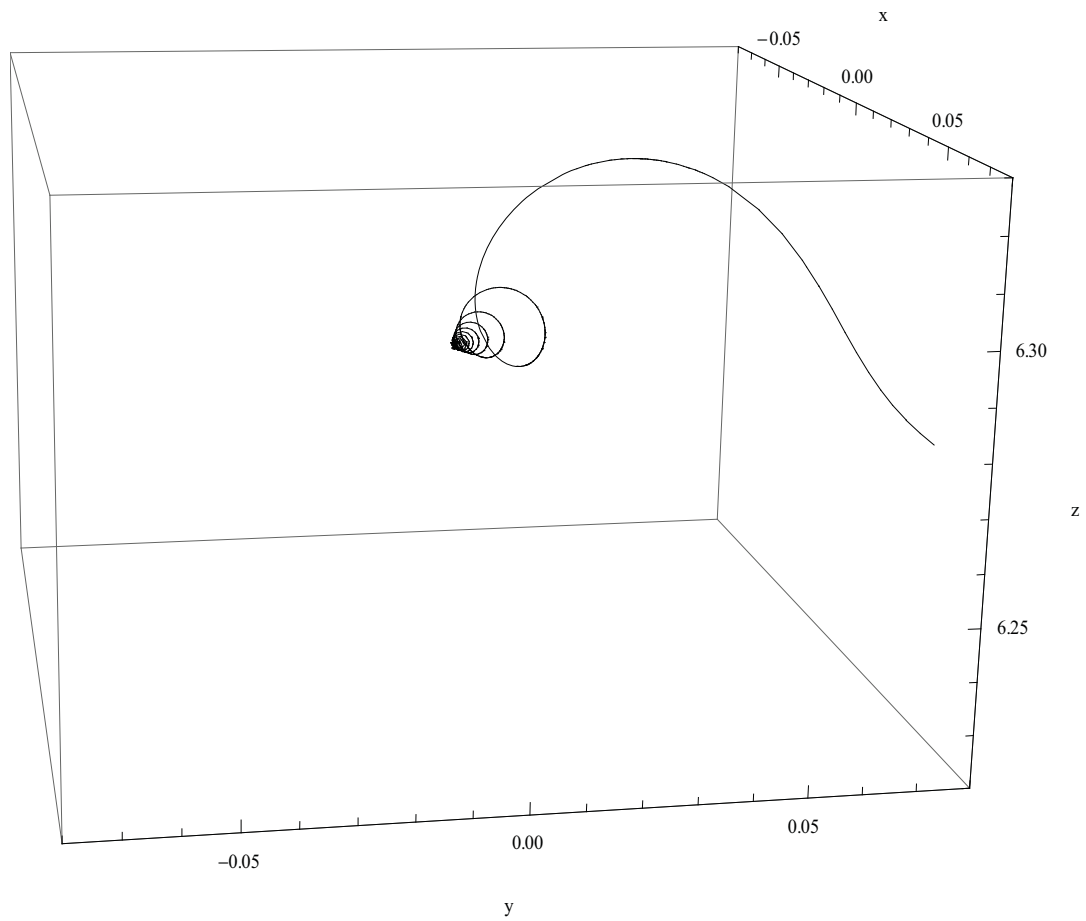
sx = (sqrt(x[u]^2 + y[u]^2 + (z[u] - h)^2))^2 * s.{1, 0, 0};
sy = (sqrt(x[u]^2 + y[u]^2 + (z[u] - h)^2))^2 * s.{0, 1, 0};
sz = (sqrt(x[u]^2 + y[u]^2 + (z[u] - h)^2))^2 * s.{0, 0, 1};

c4 = NDSolve[{D[x[u], u] == sx, D[y[u], u] == sy, D[z[u], u] == sz, x[0] == 0.04, y[0] == 0.04, z[0] == h + 0.04}, {x, y, z},
  {u, -0.092, 0.3}, StartingStepSize -> 0.02, MaxStepSize -> 0.02, MaxSteps -> 500 000,
  Method -> {StiffnessSwitching, Method -> {ExplicitRungeKutta, Automatic}}]

G4 = ParametricPlot3D[Evaluate[{x[u], y[u], z[u]} /. c4], {u, -0.092, 0.3}, PlotRange -> {{-0.08, 0.08}, {-0.08, 0.08}, {6.22, 6.33}},
  AxesLabel -> {"x", "y", "z"}, PlotStyle -> Black]

```

Test Run Output:



## APPENDIX C

### THE POYNTING VECTOR CLOSE TO A DIPOLE ABOVE A MIRROR

Close to the dipole, the parameter  $q_1$  is small, and the expressions from Appendix A can be simplified. We shall assume that  $q_1 \ll 1$  and  $q_1 \ll h$ . It follows from Eqs. (A15) and (A13) that the magnitude of vector  $\mathbf{q}_2$  is

$$q_2 = \sqrt{q_1^2 + 4hq_1 \cos \theta_1 + 4h^2} \quad , \quad (C1)$$

and therefore

$$q_2 = 2h + q_1 \cos \theta_1 + O(q_1^2) \quad . \quad (C2)$$

This function of  $q_1$  appears in  $f_1$ ,  $g_1$ ,  $f_2$  and  $g_2$  of Eqs. (A7)-(A10), in the parameters  $b$ ,  $b'$  and  $c$  of Eqs. (A18)-(A20), and in the interference term in Eq. (A11). The unit vector in the  $\mathbf{q}_2$  direction, appearing on the right-hand side of Eq. (A12), becomes

$$\hat{\mathbf{q}}_2 = \mathbf{e}_z + \frac{q_1}{2h} \mathbf{e}_\rho \sin \theta_1 + O(q_1^2) \quad . \quad (C3)$$

A systematic expansion in orders of  $q_1$  then yields for the Poynting vector in the near field

$$\begin{aligned} \boldsymbol{\sigma}(\mathbf{q}) = & \hat{\mathbf{q}}_1 \sin^2 \alpha + \sin \gamma \left[ \frac{v(h)}{q_1} + w(h) \cos \theta_1 \right] \left[ (3a^2 - 1) \boldsymbol{\varepsilon}' - 3a(\hat{\mathbf{q}}_1 \cdot \boldsymbol{\varepsilon}') \boldsymbol{\varepsilon} \right] \\ & + \sin \gamma \frac{\sin(2h)}{2h} (\boldsymbol{\varepsilon} \sin \theta_1 \sin \phi - \hat{\mathbf{q}}_1 \sin \gamma) \\ & + \frac{v(h)}{2h} [\mathbf{e}_\rho (c' - 3aa') \sin \theta_1 - \hat{\mathbf{q}}_1 (c' - 3 \cos^2 \gamma)] \\ & + \boldsymbol{\varepsilon}^{\text{im}} (3a \sin \theta_1 - \sin \gamma \sin \phi) \sin \theta_1 - \boldsymbol{\varepsilon} (3 \cos \gamma \cos \theta_1 - a') \quad + O(q_1) \quad . \quad (C4) \end{aligned}$$

Here,  $v(h)$  and  $\boldsymbol{\varepsilon}'$  are defined in chapter 4, and in addition we introduce the function

$$w(h) = \frac{1}{2h^2} \cos(2h) + \frac{1}{2h} \left( 1 - \frac{1}{2h^2} \right) \sin(2h) \quad . \quad (C5)$$

APPENDIX D  
BIOGRAPHICAL SKETCH



The author was born on April 6th, 1986, in Ji'an, Jiangxi, China. She received her B.Sc. degree in Applied Physics from Beijing Institute of Technology in July 2006. Then she continued her studies at the Department of Science of Beijing Institute of Technology and she received her M.S. degree in condensed matter physics in July 2008. Starting from Fall 2007, the author enrolled in the Ph.D. program at Mississippi State University and received another M.S. in Physics from the Department of Physics and Astronomy in December 2008. At Mississippi State University, the author had the privilege of working with Dr. Arnoldus, doing research in theoretical optics and she had several publications in some high-profile journals (<http://www2.msstate.edu/~xl121/>). She has also received the outstanding graduate student performance award (2008) from the Sigma Xi Scientific Research Society at MSU.



APPENDIX E  
PUBLICATIONS OF XIN LI

- [1] Henk F. Arnoldus, **Xin Li** and Jie Shu, *Sub-Wavelength Displacement of the Far-Field Image of a Radiating Dipole*, Optics Letters **33**, 1446-1448 (2008).
- [2] Jie Shu, **Xin Li** and Henk F. Arnoldus, *Energy Flow Lines for the Radiation Emitted by a Dipole*, Journal of Modern Optics **55**, 2457-2471 (2008).
- [3] **Xin Li**, Jie Shu and Henk F. Arnoldus, *Far-Field Detection of the Dipole Vortex*, Optics Letters **33**, 2269-2271 (2008).
- [4] **Xin Li**, Jie Shu and Henk F. Arnoldus, *Nanoscale Displacement of the Image of an Atomic Source of Radiation*, Chinese Optics Letters **7**, 149-151 (2009).
- [5] Jie Shu, **Xin Li** and Henk F. Arnoldus, *Nanoscale Shift of the Intensity Distribution of Dipole Radiation*, Journal of the Optical Society of America A **26**, 395-402 (2009).
- [6] **Xin Li**, Jie Shu and Henk F. Arnoldus, *Optical Vortices and Singularities Due to Interference in Atomic Radiation Near a Mirror*, Optics Letters **34**, 3595-3597 (2009).
- [7] **Xin Li** and Henk F. Arnoldus, *Macroscopic Far-Field Observation of the Sub-Wavelength Near-Field Dipole Vortex*, Physics Letters A **374**, 1063-1067 (2010).
- [8] **Xin Li** and Henk F. Arnoldus, *Electric Dipole Radiation near a Mirror*, Physical Review A **81**, 053844-1-053844-10 (2010).
- [9] **Xin Li**, Jie Shu and Henk F. Arnoldus, Computational Studies of New Materials II: From Ultrafast Processes and Nanostructures to Optoelectronics, Energy Storage and Nanomedicine (2010), Chapter 14, invited article, Eds. Thomas F. George, Daniel A. Jelski, Renat R. Letfullin and Guoping Zhang (World Scientific, Singapore), in press, *Nanoscale Resolution in the Near and Far Field Intensity Profile of Optical Dipole Radiation*.
- [10] **Xin Li** and Henk F. Arnoldus, *Reversal of the Dipole Vortex in a Negative Index of Refraction Material*, Physics Letters A, in press, 2010.

Pdf's of publications can be found at <http://hfal.physics.msstate.edu/pub.html>